Multivariate image analysis for quality inspection in fish feed production

Ljungqvist, Martin Georg; Ersbøll, Bjarne Kjær; Frosch, Stina

Publication date:
2012

Document Version
Publisher's PDF, also known as Version of record

Multivariate image analysis for quality inspection in fish feed production

Martin Georg Ljungqvist

Kongens Lyngby 2012
IMM-PHD-2012-273

Technical University of Denmark
Informatics and Mathematical Modelling
Building 321, DK-2800 Kongens Lyngby, Denmark
Phone +45 45253351, Fax +45 45882673
reception@imm.dtu.dk
www.imm.dtu.dk

IMM-PHD: ISSN 0909-3192

Abstract

Aquaculture is today one of the fastest growing food producing sectors in the world. Access to good and effective fish feed is a condition for optimised and sustainable aquaculture activity. In the aquaculture industry it is of utmost importance that the fish get feed of proper size and nutrition. The colour appearance of fish products is important for customers. Salmonid fish get their red colour from a natural pigment called astaxanthin. To ensure a similar red colour of fish in aquaculture astaxanthin is used as an additive coated on the feed pellets. Astaxanthin can either be of natural origin, or synthesised chemically. Common for both types is that they are relatively expensive in comparison to the other feed ingredients.

This thesis investigates multi-variate data collection for visual inspection and optimisation of industrial production in the fish feed industry. Quality parameters focused on here are: pellet size, type and concentration level of astaxanthin in pellet coating, as well as astaxanthin type detected in salmonid fish. Methods used are three different devices for multi- and hyper-spectral imaging, together with shape analysis and multi-variate statistical analysis.

The results of the work demonstrate a high potential of image analysis and spectral imaging for assessing the product quality of fish feed pellets, astaxanthin and fish meat. We show how image analysis can be used to inspect the pellet size, and how spectral imaging can be used to inspect the surface quality of biological materials. This technology and method can be a useful tool for optimising the industrial process, e.g. the utilisation of the expensive astaxanthin. The development of automatic quality inspection methods by machine vision can improve the industry's position in the competition for high quality products and efficient processes.

Resumé

Akvakultur er i dag en af de hurtigst voksende fødevare-producerende sektorer i verden. Adgang til godt og effektivt fiskefoder er en forudsætning for optimal og bæredygtig akvakultur aktivitet. I akvakulturindustrien er det af største vigtighed at fiskene får foder af passende størrelse og næringsindhold. Farven på fiskeprodukter er af stor betydning for kundernes valg. Laksefisk får deres røde farve fra det naturlige pigment astaxanthin. For at sikre en tilsvarende rød farve af fisk fra akvakultur anvendes astaxanthin inden for akvakultur som fodertilsætningsstof belagt på foderpillerne. Astaxanthin kan enten være af naturlig oprindelse eller produceret ved kemisk syntese. Fælles for begge typer er at de er relativt dyre sammenlignet med de øvrige bestanddele i fiskefoder.

Denne afhandling undersøger multivariat dataindsamling for visuel inspektion og optimering af industriel produktion i fiskefoderbranchen. Kvalitetsparametre fokuseret på her er: pellet størrelse, type og koncentration af astaxanthin i pellet coating, såvel som type af astaxanthin detekteret i laksefisk. Metodemæssigt anvendes tre forskellige kameraer til multi- og hyper-spektral billedhåndtering, sammen med form analyse og multivariat statistisk analyse.

Resultaterne af arbejdet viser et stort potentiale for billedanalyse og spektral scanning til at vurdere kvaliteten af fiskefoderpiller, astaxanthin og fiskekød. Vi viser hvorledes billedanalyse kan anvendes til at inspicere pellet størrelse, og hvor spektral billeddannelse kan anvendes til at overvåge overfladekvaliteten af biologiske materialer. Denne teknologi og fremgangsmåde kan være nyttige værktøjer i industrien til optimering af f.eks. brugen af den dyre astaxanthin. Udviklingen af automatiske kvalitetskontrolmetoder kan forbedre industriens position i konkurrencen om produkter af høj kvalitet og forarbejdet med effektive processer.

Preface

This thesis was prepared at the Image Analysis and Computer Graphics group at DTU Informatics and submitted to the Technical University of Denmark (DTU), in partial fulfilment of the requirements for the degree of Doctor of Philosophy, Ph.D., in Informatics and Mathematical Modelling. The project was funded by DTU Informatics, ITMAN Research School programme, BioMar A/S and the EU under the Seventh Framework Programme FP7/2007-2013 under grant agreement number 214505.10 (NEMO).

The work herein represents selected parts of the research work carried out in the Ph.D. time period. The project deals with different aspects of image analysis of multi-variate and spectral images using multi-variate statistics, with applications in the aquaculture industry. The thesis consists of a summary report and a collection of six research papers written during the period 2009–2012, and elsewhere published. The summary part gives background information and an overview of the contributions.

This thesis is an interdisciplinary project between DTU Informatics and DTU Food, done in concert with the NEMO EU project, the Centre for Imaging Food Quality at DTU, and collaboration with BioMar A/S, Brande, Denmark. Part of the research was conducted at the Toyohashi University of Technology, Toyohashi, Japan, under the supervision of Professor Shigeki Nakauchi. The project was supervised by Professor Bjarne Kjær Ersbøll at DTU Informatics, and Associate Professor Stina Frosch at DTU Food.

This thesis was submitted in the end of August 2012, defended 9th of November 2012 and revised for print in April 2013. Since January 2013 DTU Informatics is called DTU Compute.

Kgs. Lyngby, August 2012

Martin Georg Ljungqvist

Publications

Listed here are the scientific publications prepared during the course of the Ph.D. program. The publications included in Part II of the thesis are referred to by their respective appendix notation.

[A] [91] Martin Georg Ljungqvist, Michael Engelbrecht Nielsen, Bjarne Kjær Ersbøll, Stina Frosch. Image Analysis of Pellet Size for a Control System in Industrial Feed Production. PLoS ONE, Public Library of Science, 6, e26492, 2011.

[B] [87] Martin Georg Ljungqvist, Bjarne Kjær Ersbøll, Michael Engelbrecht Nielsen, Stina Frosch. Multi-spectral Image Analysis for Astaxanthin Coating Classification. JIST, Journal of Imaging Science and Technology, 56, 020403-1–020403-6, 2012.

[C] [90] Martin Georg Ljungqvist, Stina Frosch, Michael Engelbrecht Nielsen, Bjarne Kjær Ersbøll. Multi-spectral Image Analysis for Robust Prediction of Astaxanthin Coating. Applied Spectroscopy 67(7) July 2013, accepted for publication.

[D] [89] Martin Georg Ljungqvist, Ken-ichi Kobayashi, Stina Frosch, Michael Engelbrecht Nielsen, Bjarne Kjær Ersbøll, Shigeki Nakauchi. Near-Infrared Hyper-spectral Image Analysis of Astaxanthin Concentration in Fish Feed Coating. Proceedings of the IEEE International Conference on Imaging Systems and Techniques, 2012.

[E] [92] Martin Georg Ljungqvist, Otto Højager Nielsen, Stina Frosch, Michael Engelbrecht Nielsen, Line Harder Clemmensen, Bjarne Kjær Ersbøll. Hyper-

spectral Imaging based on Diffused Laser Light for Prediction of Astaxanthin Coating Concentration. Machine Vision and Applications 2013, accepted for publication.

[F] [85] Martin Georg Ljungqvist, Bjørn Skovlund Dissing, Michael Engelbrecht Nielsen, Bjarne Kjær Ersbøll, Line Harder Clemmensen, Stina Frosch. Classification of Astaxanthin Colouration of Salmonid Fish using Spectral Imaging and Tricolour Measurement. IMM-Technical Report-2012-08, Technical University of Denmark (DTU).

Co-authors of the publications in Part II and their affiliations are listed below in alphabetical order.

- Line Harder Clemmensen
  Department of Informatics and Mathematical Modelling, Technical University of Denmark, Lyngby, Denmark.
- Bjørn Skovlund Dissing
  Department of Informatics and Mathematical Modelling, Technical University of Denmark, Lyngby, Denmark.
- Bjarne Kjær Ersbøll
  Department of Informatics and Mathematical Modelling, Technical University of Denmark, Lyngby, Denmark.
- Stina Frosch
  Division of Industrial Food Research, National Food Institute, Technical University of Denmark, Lyngby, Denmark.
- Ken-ichi Kobayashi
  Department of Information and Computer Sciences, Toyohashi University of Technology, Toyohashi, Japan.
- Shigeki Nakauchi
  Department of Information and Computer Sciences, Toyohashi University of Technology, Toyohashi, Japan.
- Michael Engelbrecht Nielsen
  Division of Industrial Food Research, National Food Institute, Technical University of Denmark, Lyngby, Denmark.
- Otto Højager Attermann Nielsen
  Department of Informatics and Mathematical Modelling, Technical University of Denmark, Lyngby, Denmark.

Published abstracts are listed below.

- High speed imaging of drug distribution in solid dispersion film using multi-wavelength UV imaging technique.
  Jian-Xiong Wu, Jens Michael Carstensen, Frans van den Berg, Martin Georg Ljungqvist, Thomas Rades, Jukka Rantanen
  American Association of Pharmaceutical Sciences Annual Meeting and Exposition 2012, Chicago, USA.

- Visual effects of β-glucans on wound healing in fish.
  Jacob Schmidt, Martin Georg Ljungqvist, Bjarne Kjær Ersbøll, Michael Engelbrecht Nielsen
  Scandinavian Workshop on Imaging Food Quality 2011, Ystad, Sweden.

- Using Image Analysis On Standardised Full-Thickness Wounds In Scattered Mirror Carp (*Cyprinus Carpio*) As A Model For Wound Healing.
  Jacob Schmidt, Bjørn Skovlund Dissing, Martin Georg Ljungqvist, Bjarne Kjær Ersbøll, Michael Engelbrecht Nielsen
  15th European Association of Fish Pathologists conference 2011, Split, Croatia.

- Analysis of Astaxanthin in Fish Feed Pellets.
  Martin Georg Ljungqvist, Stina Frosch, Michael Engelbrecht Nielsen, Bjarne Kjær Ersbøll
  40th West European Fish Technologists Association Conference 2010, Izmir, Turkey.

- Image Analysis of Wound Healing in Fish.
  Martin Georg Ljungqvist, Jacob Schmidt, Bjarne Kjær Ersbøll
  French-Danish Workshop on Spatial Statistics and Image Analysis in Biology 2010, Copenhagen University LIFE.

- Multispectral image analysis in seafood.
  Stina Frosch, Martin Georg Ljungqvist, Michael Engelbrecht Nielsen
  Foods for Health Workshop 2010, Copenhagen, Denmark.

- Effects of beta-glucans on wound healing in carp, *Cyprinus carpio*.
  Jacob Schmidt, Martin Georg Ljungqvist, Natalia Ivonne Vera Jiménez, Dominika Alicja Przybylska, Bjarne Kjær Ersbøll, Michael Engelbrecht Nielsen
  40th West European Fish Technologists Association Conference 2010, Izmir, Turkey.

- Image analysis and multivariate statistics in production of aquaculture feed.

Martin Georg Ljungqvist, Bjørn Skovlund Dissing, Michael Engelbrecht Nielsen, Bjarne Kjær Ersbøll, Stina Frosch
International Workshop on Multivariate Image Analysis 2009, Valencia, Spain.

Acknowledgements

Acknowledgements goes to my main supervisor Bjarne Kjær Ersbøll for being a robust and always encouraging mentor, my co-supervisor Stina Frosch for always being supportive with relevant feedback, and Michael Engelbrecht Nielsen for all practical and good ideas.

Bjørn Skovlund Dissing for rewarding discussions about multi-spectral image analysis and script toolbox development. Line Harder Clemmensen and Karl Sjöstrand for discussions and questions about data analysis. Otto Højager Nielsen for a good collaboration in the laboratory and in the writing process. Christina Horn Nexø for guidance in the administrative part of the Ph.D. programme. Jacob Schmidt for interesting collaboration on posters about fish and technology.

Ken-ichi Kobayashi and Shigeki Nakauchi for a good collaboration and for welcoming me with warm hands on my external stay in Japan; arigatou gozaimasu. BioMar for all important input about the industry. All the people in the NEMO project, and all the people in the CIFQ project. All fellow Ph.D.-students and academic staff at DTU for useful suggestions, fruitful discussions and good company. The Swedish commuting team.

My family and friends. Many thanks to Charlotta Nilsson, Rolf Nilsson, Kristina Månros, Viktor Siira, and Benjamin Morris for proofreading the summary part of the thesis. Warm thanks to Charlotta for being so supportive, understanding, and wonderful.

Gratias omnes! Carpe diem quam minimum credula postero.

Contents

Part I

Summation

Chapter 1

Introduction

1.1 Motivation and Aims

Aquaculture is expanding rapidly throughout the world, today it is one of the fastest growing food producing sectors in the world. Aquaculture is where aquatic organisms such as fish, mussels and crustaceans are farmed, and it accounts for about half of the food fish in the world [115]. Access to good and effective fish feed is a condition for optimised and sustainable aquaculture activity. In the aquaculture industry it is of utmost importance that the fish get feed of proper size. The feed is usually in pellet form, where the pellets contain the nutrients that the fish need to grow and to stay healthy. The size of the pellets is adapted to the size of the fish so that the fish can grow as expected. It has been shown that the growth rate of fish is closely related to the pellet size of the feed [8, 136, 145]. Therefore, when producing feed pellets for aquaculture there is a need to control the size of the output product.

The colour appearance of fish products is important for customers [57, 108, 127]. Consumers associate increased level of red in salmonid fishes with superior quality, and colour is indeed the first quality parameter which they inspect. Today in the industry the colour of a salmonid fish fillet is measured by human inspection and compared to a standardised scale, which is both labour intensive and not necessarily accurate and robust.

Salmonid fish get their red colour from a naturally occurring carotenoid pigment called astaxanthin. Astaxanthin has a high antioxidant activity essential for reproduction, growth and survival, and important for the development of colour in salmonid fish [128]. The primary use of astaxanthin within aquaculture is as a feed additive to ensure that farmed salmon and trout have similar appearance to their wild counterparts [138]. For this purpose, the fish feed pellets are coated with fish oil with added astaxanthin. Astaxanthin is very expensive [9] and therefore optimising quantities used in the fish feed production is important.

Natural astaxanthin for use in aquaculture can be extracted from *Huematococcus pluvialis* algae, *Phaffia* yeast, or extracted from crustaceans such as prawns [4, 20, 70, 71, 103]. The natural solvent is oil.

The so-called synthetic version of astaxanthin is obtained from chemical industry and is usually obtained as cold water dispersible; dissolved in water. Synthetic astaxanthin is more easily available and costs slightly less than natural astaxanthin and is therefore used more often in industry. However, there is a demand for natural astaxanthin for the organic salmonid fish market where natural astaxanthin is mandatory by law.

In the industry many different pellet recipes are used depending on type and size of the fish. Also, the raw material ingredients of any one recipe may well vary depending on availability and price. Automatic and robust visual analysis is important for statistical production control. Furthermore, optimisation of astaxanthin is of great interest in the aquaculture feed pellet production.

In industrial fish feed production, the feed material is commonly extruded through a die plate with holes of a certain diameter which determines the diameter of the pellets. Different die plates with different dimensions of the holes are used for different pellet size. On the other side of the disk is a set of rotating knives that cut the material into shorter cylinder-shaped pellets. The length of the pellets is determined both by the velocity of the knives and the extrusion pressure inside the machine. Pellet extrusion is thus a multi-variate problem.

While the extruder machine is operating the temperature of the machine increase, and this may affect its physical properties and the product quality [10]. Also, with time the holes in the die plate get clogged with raw material. This clogging of holes results in an increase in pressure inside the extruder and thus an increase in the velocity of the feed material that passes through the holes. Since the rotating knives are not adjusted accordingly, the result is a drift in the pellet size. Hence, changes in pressure and temperature result in the problem that the pellet size changes over time during a batch production.

Today, pellet size monitoring is done by manual inspection in order to adjust

the settings or restart the machine to regain balance in the production. This is both labour intensive and relies on experienced assessors. If automatic size measurement could indicate when the pellet size is outside the defined range, this information could be used to adjust machine settings such as the knife speed, screw speed, filling rate or other means of controlling the pellet expansion process, thereby controlling the pellet size and ensuring uniformity.

Quality inspection in food and feed production often consists of visual parameters and having non-invasive and fast measuring methods is of paramount importance. Automatic quality inspection is becoming more common and feasible to implement. Small differences in size or in surface characteristics can be hard to detect using only the naked human eye. Visual inspection using digital cameras has the advantage of being objective, precise and automatic.

An automatic vision system for on-line quality control would be of great benefit to the industry, both for process control and product optimisation.

1.2 Objectives

This thesis aims at investigating multi-variate data collection for visual inspection of industrial production with fish feed industry as case. An overview image can be seen in Figure 1.1. Quality parameters here focused on are pellet size, as well as both type and concentration level of astaxanthin, and also astaxanthin type detected in salmonid fish. An overview of the objectives is shown here:

- Investigate the possibility of on-line quality assurance of pellet size in relation to the extrusion of fish feed products.
- Investigate the possibility of at-line quality assurance of astaxanthin coating in the extrusion of fish feed products.
- Investigate the possibility of determining the astaxanthin type detected in salmonid fish meat.
- Use multi- or hyper-spectral imaging, and shape analysis together with methods for data analysis from recent developments in modern data-intensive statistical analysis.

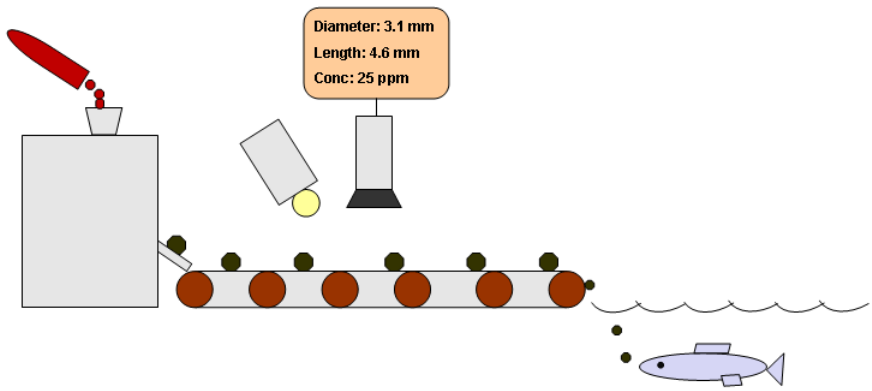

Figure 1.1: Overview of the industrial quality inspection within aquaculture.

1.3 Thesis Outline

This thesis consists of two parts. Part I introduces and summarises the work carried out during the Ph.D. program. Part II is comprised of the scientific publications. The main contributions of this thesis are concentrated around the included research papers. Since the scientific papers are published in a self-contained nature, some overlap occurs between the two parts.

Part I

Chapter 1 provides an introduction to the motivation and intentions of the work presented in the thesis, as well as drawing parallels to related projects.

Chapter 2 introduces the concepts of statistical quality control, machine vision, colour, near infra-red spectrum, and spectral imaging.

Chapter 3 provides an introduction to multi-variate statistical methods for data analysis.

Chapter 4 provides a summary of the experimental work and results of part II and the main contributions of the thesis.

Chapter 5 contains a discussion of the contributions in relation to the objectives as well as future work. Finally, the chapter concludes the thesis with some closing remarks.

Part II

Paper A describes a method for using image analysis of a large amount of piled fish feed pellets in order to predict the average pellet size.

Paper B introduces the investigation of spectral imaging for inspection of astaxanthin coating on feed pellets. Both linear and non-linear discriminant analyses are used in order to classify pellets with or without astaxanthin coating.

Paper C addresses several aspects of spectral imaging for pellet coating inspection. The concentration level of synthetic astaxanthin coating was analysed by spectral imaging, also four different pellet recipes were used in order to see how stable the prediction is with respect to the underlying recipe. Furthermore, both natural and synthetic astaxanthin coating was used in order to see if it is possible to discriminate the types. Two different statistical methods were used for variable selection.

Paper D investigates the synthetic astaxanthin coating characteristics in the near infra-red parts of the spectrum, in order to predict the concentration level by hyper-spectral imaging. A filter design method is used in order to investigate which parts of the spectrum can be used for optical filters for the prediction.

Paper E presents a novel technique for capturing hyper-spectral images using diffused laser light, and is demonstrated for predicting synthetic astaxanthin coating concentration level. This was compared to a parallel study and sparse statistics was used for astaxanthin prediction.

Paper F describes the dependency between feed quality and fish quality; it was investigated if natural and synthetic astaxanthin give different fish meat colour. Spectral imaging and sparse statistics was used in order to differentiate between fish having been fed with natural and synthetic astaxanthin.

1.4 Abbreviations

All abbreviations of the form of acronyms and initialisms in this thesis are spelled out the first time used in Part I, and the first time used in each Paper Appendix in Part II, and will then be used consequently as abbreviations. Even if the phrase is only used once the abbreviation is denoted for the reader's information. As a list of reference, they are all presented here for the reader's convenience.

ADC	Analogue to Digital Converter
AOTF	Acousto-Optical Tunable Filter
ASC	Auto-Scale
BPF	Band Pass Filter
CCD	Charge-Coupled Device
CIE	International Commission on Illumination
CL	Centre Line
CMOS	Complementary Metal-Oxide-Semiconductor
CV	Cross Validation
DTU	Technical University of Denmark
DDS	Direct Digital Synthesizer
EN	Elastic Net
HPLC	High Pressure Liquid Chromatography
IQR	Interquartile Range
IR	Infra-red
Laser	Light amplification by stimulated emission of radiation
LASSO	Least Absolute Shrinkage and Selection Operator
LED	Light Emitting Diode
LCL	Lower Control Limit
LDA	Linear Discriminant Analysis
LOOCV	Leave One Out Cross Validation
LSL	Lower Specification Limit
MCT	Mercury Cadmium Telluride
MSC	Multiplicative Scatter Correction
NIR	Near Infra-Red
NIST	National Institute of Standards and Technology
nm	nanometre
OLS	Ordinary Least Squares
OSH	Optimal Separating Hyperplanes
PC	Principal Component
PCA	Principal Component Analysis
PCF	Photonic Crystal Fibre
PLSR	Partial Least Squares Regression
ppm	parts per million
PRESS	Prediction Residual Sum of Squares
PS	Pattern Spectrum
QDA	Quadratic Discriminant Analysis
RBF	Radial Basis Function
RGB	Red, Green, Blue
RMSE	Root Mean Square Error
ROI	Region of Interest
RPD	Ratio between the standard error of Prediction and the standard Deviation
RR	Ridge Regression
RSS	Residual Sum of Squares
SD	Standard Deviation
SEC	Standard Error of Calibration
SEP	Standard Error of Prediction

sRGB	Standard Red, Green, Blue
SLDA	Sparse Linear Discriminant Analysis
SLS	Subsurface Laser Scattering
SNV	Standard Normal Variate
SPC	Statistical Process Control
SQC	Statistical Quality Control
SVD	Singular Value Decomposition
SVM	Support Vector Machine
SWIR	Short Wave Infra-Red
TEM	Transverse Electromagnetic
TSS	Total Sum of Squares
UCL	Upper Control Limit
USL	Upper Specification Limit
UV	Ultra Violet
UVA	Ultra Violet A

Chapter 2

Machine Vision for Quality Control

This chapter gives an introduction to the area of using cameras for automatic industrial quality inspection, including a section on colour and spectral imaging.

2.1 Industrial Inspection

A manufacturer is interested in producing a controlled product. Irrespective of the care taken in defining the production procedure, the manufacturer realises that he cannot make all units of a given kind of product identical. This can be seen in the afore mentioned problem of drift of the size in pellet production. The application of statistical methods in mass production makes it possible to use raw materials, processes, and economics more efficiently [126].

Objective analysis of the variation in a process is usually called statistical process control (SPC), or statistical quality control (SQC). SPC deals with examination of specific parts of a process. The aim is to investigate which parts of the variation are dependent on controllable factors and which are merely due to chance.

An industrial production process can have more or less variation. Even though the process is calibrated to produce products with specific characteristics there is usually a bit of variation. There could be many reasons that the final products do not ultimately fulfil the specifications. For example if a drift occurs in the process the product characteristics might be too small in the beginning and too large by the end of the process.

It is desirable to monitor and control the process to make sure that it operates at its full potential. This information can be used in order to amend the production; correct for more mistakes and in that way increase the quality of the production.

A commonly used tool in SPC is the control chart, also known as Shewhart charts or process-behaviour charts [125]. The control chart is a very useful process monitoring technique, used to determine whether a manufacturing (or similar) process is in a state of statistical control. A typical control chart plots the averages of the measurements of a quality characteristic in samples taken from the process. The quality characteristic is plotted versus sample number or time. The chart typically has a centre line (CL) consisting of the mean, and along with upper and lower control limits (UCL, LCL) placed typically at three standard errors from the centre line. When unusual sources of variation are present, sample averages will plot outside the control limits. This is a signal that some investigation of the process should be made and actions to correct the process taken [100].

The quality parameter has a target value, along with an upper specification limit (USL) and a lower specification limit (LSL). An example chart of pellet length measurement with these limits indicated can be seen in Figure 2.1.

In the manufacturing process the quality control measurement can take place in different ways:

- Off-line is when a sample from the process is sent to a lab away from the production.
- At-line is when the measurement is made close to the production line and not in real-time.
- On-line is when the quality inspection is made in real-time on the production line, but in a forked inspection line or similar.
- In-line is when the inspection happens in real-time in the main production line, e.g. using a probe or similar.

A designed experiment is very helpful for discovering the key variables influencing the quality characteristics of interest in the process. It is a way of systematically varying the controllable input factors in the process and determining the effect this has on the output product parameters. The variability in the manufacturing process can then be reduced, and often significant improvements of the product quality can be made from using designed experiments.

Designed experiments are an off-line quality-control tool because they are often used during development and the early stages of manufacturing; they play an important role in reducing variability.

When the important variables that affect the process output have been identified, it is usually necessary to model the relationship between the influential input variables and the output quality characteristics. Statistical techniques useful in constructing such models include regression analysis and time series analysis. Regression analysis and other statistical techniques are explained in Chapter 3 Page 23.

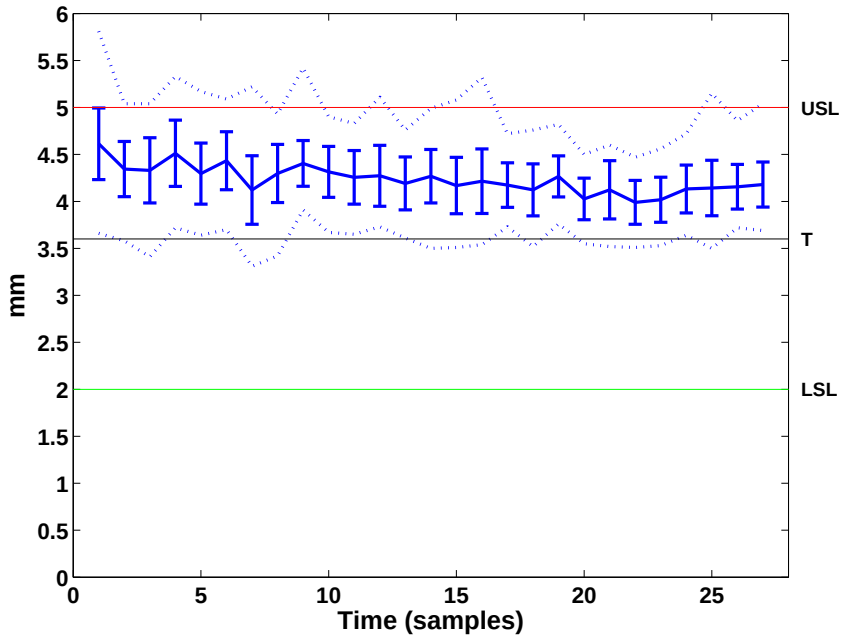

Figure 2.1: Control chart of the measured pellet length, using the calliper data from batch D in Paper A. Specified product limits are marked by horisontal lines. Vertical lines indicate one standard deviation, and dotted lines indicate maximum and minimum values.

2.2 Machine Vision

Humans are more generic than computers in many cases when it comes to analysing visual information. Computers, on the other hand, are objective, quantised and automatic. Digital images can be used for many purposes and have the advantage of being objective and non-intrusive. Image-based automatic inspection is also known as machine vision, or sometimes as computer vision, and is used for process control, machine settings, robot guidance and similar tasks in industrial applications [14]. Machine vision is based on the analysis of images to extract information for controlling a manufacturing process.

The method of machine vision typically consists of image acquisition using cameras, lenses and lighting equipment suitable for the situation. The images are analysed using digital image processing to get information about what is going on in the process, and usually also to make decisions on how to proceed based on the extracted information.

The basic image processing methods used are for example threshold, object segmentation, and pattern recognition. The segmentation is done in order to find the region of interest (ROI) in the image. The decisions made from analysing the images can be made using statistical methods, such as those described in Section 3.

Machine vision has been used for measuring astaxanthin in the aquaculture industry [17, 27, 37] and the size of fish feed pellets [49].

2.3 Colour Theory

Coloured light has varying radiant energy depending on wavelength. Coloured surfaces transmit and reflect different amounts of the incidentiary light at different wavelengths.

The spectral interaction between light and surfaces represents the basis for all representations of colour. The colour of an object is strongly dependent on its spectral reflectance.

As early as 1853 Grassmann stated that three independent variables are necessary and sufficient to psychophysically characterise a colour [59]. This theory states that the colour space is tridimensional, called tricolour. The restraint on the three primary stimuli is that they are colourimetrically independent, which

means that none of the primaries can be colour-matched by a mixture of the two others.

In the human eye, there are three types of cone cells with different spectral sensitivities: short (S), medium (M), and long (L) cone types. The names of the cones are labelled according to the wavelength of their peak sensitivity in the visible range of the electromagnetic spectrum. The S cones have their peak in the blue range, the M cones have their peak in the green range, and the L cones have their peak in the orange and red regime. Albeit these peaks are approximate, the cones are sometimes referred to as red, green, and blue [150]. The visible spectrum constitutes the natural colours, which can be seen in Figure 2.4.

Many colour primaries exist, and the most well-known set of primaries for reproducing colour is red, green, and blue (normally referred to as RGB). An example of a standard RGB (sRGB) image can be seen in Figure 2.2 with its individual colour dimensions visualised in Figure 2.3.

Figure 2.2: Example of a standard RGB representation of the technical magazine 'Ny Teknik'.

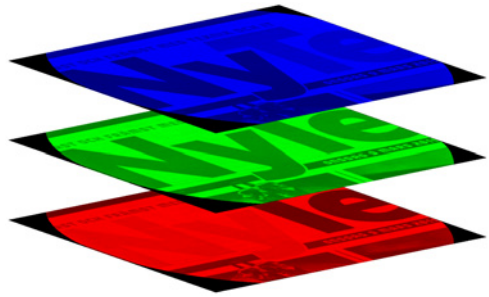

Figure 2.3: The standard RGB image in Figure 2.2 with the individual red, green, and blue layers visualised.

Another set of colour primaries is the CIE (1976) L^*, a^*, b^* (CIELAB) colour space which is perceptually uniform, specified by the International Commission on Illumination (CIE). L^* closely matches the lightness perceived by human vision, while a^* represents red and green, and b^* represents yellow and blue.

Small differences in colour are hard to see by the naked human eye. In comparison, a camera can quantise the colour differences and statistical methods can be developed to note significant differences. Humans can also be trained to see subtle colour changes, however this can can be difficult in some cases and can take several years to master.

2.3.1 Metamerism

When using three primary colours there are several different spectra that can give the same values for the primaries and thus appear as the same colour. Spectra with different spectral characteristics but resulting in the same tristimulus colour values are called metamers. Metameric colour stimuli are colour stimuli that have different spectral radiant power distributions but match in colour for a given observer [150]. Metamerism is also called colour aliasing in signal processing terms. Metamerism implies that two objects, which appear to have exactly the same colour, may have different colours under different lighting conditions.

The colour mismatch due to loss of metamerism when changing observer or lighting can be predicted numerically. Even though metamerism may cause some problems it is also the basis of the science of colour and the ability to reproduce colour images on paper and screen.

When reproducing images one could in theory make a spectral match or in practice a metameric match.

2.4 Near Infra-red

The photographic plate was invented in 1829 by Niepce and Daguerre and in the early 1880s it was noted that it had some near infra-red (NIR) sensitivity. In 1881 Abney and Festing recorded the spectra of organic liquids in the range 1 to 1.2 μm; 1000-1200 nm. This work represents the first serious NIR measurements and interpretations. Abney and Festing recognised both atomic grouping and the importance of the hydrogen bond in the NIR spectrum [22].

Not long after a spectrometer was constructed by W. W. Coblentz using a rock-salt prism and a sensitive thermopile connected to a mirror galvanometer. Around 1905 he produced a series of papers and recorded the spectra of several hundred compounds in the 1-15 μm wavelength region; 1000-15000 nm [33]. Coblentz discovered that no two compounds had the same spectrum, even when they had the same complement of elements; each compound had a unique "fingerprint". Later, Coblentz noticed certain patterns in the spectra; in this way many molecular groups were characterised and in this way a new tool for obtaining some structural information about compounds was established. Many chemical and organic components have a spectral peak in the infra-red (IR) range, with overtones in the NIR and visual frequencies of the electromagnetic spectrum.

Table 2.1: ISO 20473 specification of the spectral bands for optics and photonics.

Designation	Short designation	Wavelength (nm)
Ultraviolet, near UV	UV-A	315-380
Visible radiation, light	VIS	380-780
Infrared radiation, near IR	IR-A, NIR	780-1400
Infrared radiation, near IR	IR-B, NIR	1400-3000

The electromagnetic spectrum has different application ranges, as can be seen in Figure 2.4, and is therefore divided into different ranges. However, depending on the field of application, different definitions of these ranges exist. According to the International Organisation for Standardisation in ISO 20473 the visible range is 380-780 nm, and the NIR range is 780-3000 nm, see Table 2.1. Light is the visible part of the electromagnetic spectrum. The IR-B range is sometimes also referred to as short wave IR (SWIR). This standard notation is used in this thesis, except for the ultra-violet A (UV-A) region which is often specified with 315-400 nm (e.g. in ISO 21348).

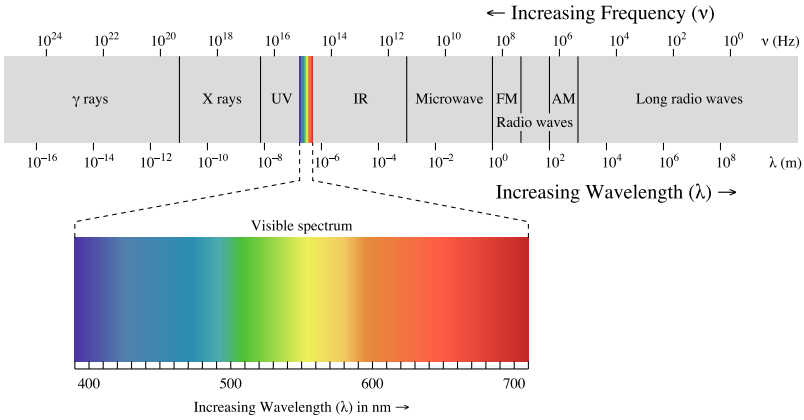

Figure 2.4: The electromagnetic spectrum with the visual region visualised by colour and wavelength (nm). Graphics by Philip Ronan.

By the continuous nature of spectral data, adjacent spectral bands are correlated.

NIR spectroscopy is a widely used technique for measuring surface properties and chemical content. NIR absorption is commonly measured as an indication of chemical content, in comparison to the scattering taking place in materials

which is indicative on the particle structure of the object. Also transmittance and reflectance can be measured using spectroscopy techniques. The spectral response of the NIR range is somewhat sensitive to temperature [12].

NIR spectroscopy has been used in the field of fish feed e.g. in a study using a spectroradiometer (325-1075 nm) for classification of four different fish feed pellet recipes [159], and for classification of feed material and feed pellets (1100-1690 nm) [44].

2.5 Spectral Imaging

By using multi-wavelength or multi-spectral image analysis it is possible to get more precise information about a surface material than the human eye is able to ascertain. The RGB system in normal cameras samples the visual light spectra in three bands: red, green and blue. Those are three broad bands of colour sampling and do not render high colour accuracy. Multi-spectral capturing devices samples the electromagnetic spectrum using a larger number of bands, and more narrow bands, leading to a higher spectral resolution and a more precise measurement of colour than the eye can see or RGB cameras can capture. With multi-spectral imaging, different spectra are distinguishable no matter if they are metameric or not.

Not only can spectral imaging measure the visual frequencies, it can also capture wavelengths that the human visual system cannot see, such as the ultra-violet (UV) and the NIR region. In comparison to spectroscopy, multi-spectral imaging includes both spectral information and spatial information simultaneously. A multi-spectral image is a data cube in the same way as an RGB image, but with more than three dimensions. In this way the information about the measured surface colour has been expanded and this light spectrum data can be used for statistical analysis of the surface chemistry.

Spectral imaging is called multi-spectral when using a small number of spectral bands, e.g. less than about 50, and hyper-spectral when using a large number of spectral bands (e.g. hundreds). Spectral imaging is the collective name for multi-spectral imaging, hyper-spectral imaging, imaging spectroscopy and similar methods.

There are different types of equipment for capturing multi- and hyper-spectral images based on a monochrome (grey-scale) camera, and they both capture the spectral bands sequentially.

In parts of the UV, the entire visual and parts of the NIR range it is possible to use a silicon-based sensor such as a charged-couple device (CCD) or a complementary metal-oxide-semiconductor (CMOS) as an image sensor. Both CCD and CMOS sensors are commonly used in commercial cameras, and if eventual spectral filters such as IR-filters are removed this type of cameras can be used for spectral imaging. Silicon-based sensors are not sensitive above about 1100 nm [14], therefore, in the NIR range e.g. a cooled, temperature stabilised mercury cadmium telluride (MCT) detector can be used.

One type of equipment uses optical filters in order to capture different parts of the spectrum, where each filter represents a spectral band. The optical filters are usually changed by using a filter wheel. A general broadband light source is used. This technique has the disadvantage that the filters introduce small geometrical differences between the captured spectral bands as the filters are not identical.

Another equipment type uses light-sources with different wavelengths instead of filters. This has the advantage that all spectral bands have the same optical properties, so each pixel has the same size and shape in all wavelengths.

A third type is a line-scan camera which samples one pixel-line of a specified range of the spectrum. This type of device is usually combined with a moving slider and broadband light sources to create spectral images [54]. A line-scan camera typically consists of an imaging spectrograph for a specified wavelength region, and a detector (sensor) such as CCD, CMOS or MCT.

Since an image sensor has varying sensitivity along the spectral range, and light sources have varying intensity along the spectra, there is a need for calibration of spectral images. Furthermore, the dark current in the camera sensor is sensitive to increased temperature [14]. Calibration is usually done by capturing images of standard black and standard white and calibrating the intensity of the spectral bands for successive images accordingly.

The visible part of a multi-spectral spectrum can be transformed to any colour space and be rendered under different illuminations. Multi-spectral images can be converted to tristimulus e.g. sRGB images, usually by reconstruction of the spectra [36, 107, 158], but it is not equivalent to taking the image using a regular RGB camera since some wavelengths in the spectral image might be missing and are just interpolated in the reconstruction. A normal RGB camera would capture all visible wavelengths but only quantised into three bands, while a multi-spectral device quantises them into multiple bands.

The image in Figure 2.2 was reconstructed to sRGB from a multi-spectral image, which also can be seen represented by its 20 spectral bands in Figures 2.5 and

2.6. In Figure 2.6 the different regions of different colours can readily be seen to differ spectrally, also in the NIR region.

Multi- and hyper-spectral image analysis has applications in many areas, for example archives [158], printing industry, colour inspection and sorting [14], forensic analysis, geology [53], pharmaceutical industry [31, 32, 54, 56, 61, 119, 120], and satellite imaging [53, 135]. Multi- and hyper-spectral imaging has shown good results in previous biological applications where it is of interest to detect subtle differences in colour and surface chemistry [19, 30, 31, 32, 37, 56, 62, 74, 80, 110, 133, 140, 149].

Production technologies such as multi- and hyper-spectral imaging systems for on-line quality control are of great benefit to the industry both in relation to process control and subsequent process optimization.

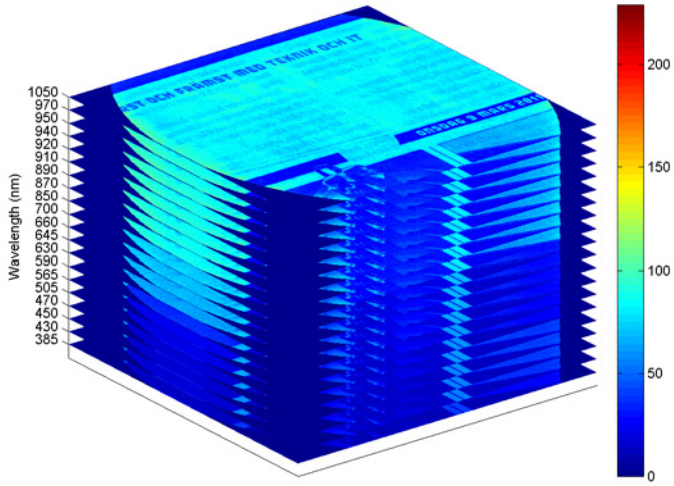

Figure 2.5: The multi-spectral original of the image in Figure 2.2 with the individual spectral bands visualised (using the jet colour map for intensity).

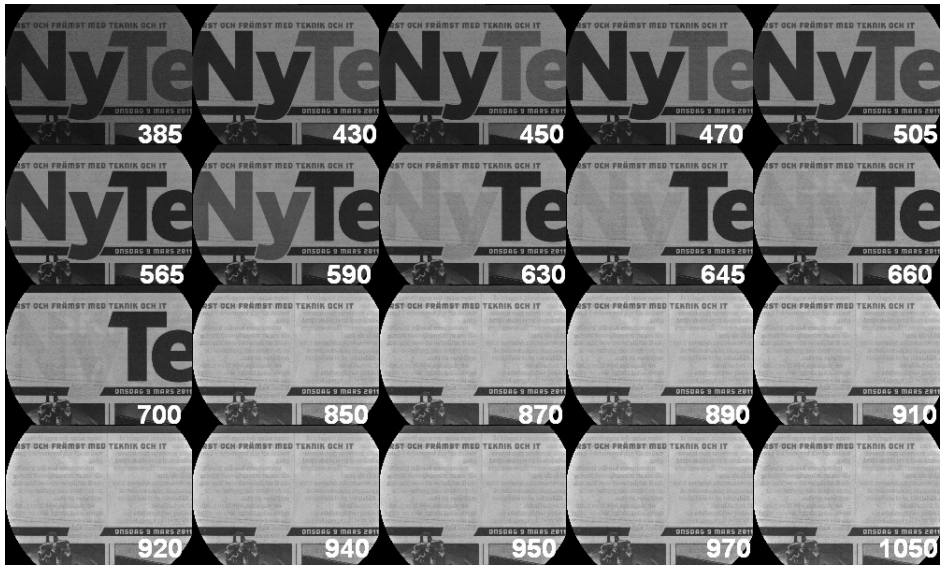

Figure 2.6: The multi-spectral original of the image in Figure 2.2 with the individual spectral bands (nm) and intensity in grey-scale.

Chapter 3

Data Analysis

As more advanced measurement techniques are developed there is also a corresponding need for using all measured variables in an understandable way. It is becoming easier to gather large amounts of data, but there is also a need to find the relevant structures in it. This chapter serves as a background on the statistical methods used for analysing images and other data in this thesis. The reader is assumed to have an understanding of the basic statistical terms.

3.1 Symbols

n	Total number of samples
p	Number of variables
i	Group numbering
n_c	Number of samples in a calibration set
n_v	Number of variables in a validation set
$\mathbf{X}$	Matrix of gathered data of n samples and p variables
$\mathbf{x}$	Vector of one data sample from matrix $\mathbf{X}$, with length p
$\mathbf{y}$	Vector of ground truth reference values, with length n
$\hat{\mathbf{y}}$	Vector of the predicted (estimated) value of $\mathbf{y}$
$\boldsymbol{\beta}$	Model coefficients

$\boldsymbol{\mu}$ Vector of arithmetic mean values
σ Standard deviation
$\boldsymbol{\Sigma}$ Covariance matrix of matrix $\mathbf{X}$

3.1.1 Hotelling's T^2

Hotelling's T^2 test can be used for multi-variate data in order to see if two group means are significantly different [43, 66]. Hotelling's T^2 calculates the statistical significance of the group means' difference.

The pooled covariance matrix is used, as calculated by Equation 3.1. For two sample groups, Hotelling's T^2 is calculated by Equation 3.2 and the following test statistic by Equation 3.3. Large values of the test statistic Z means that the groups are significantly different, and is compared to the F-distribution.

$$\boldsymbol{\Sigma} = \frac{(n_1 - 1)\boldsymbol{\Sigma}_1 + (n_2 - 1)\boldsymbol{\Sigma}_2}{n_1 + n_2 - 2} \,. \tag{3.1}$$

$$T^2 = \frac{n_1 n_2}{n_1 + n_2}(\boldsymbol{\mu}_1 - \boldsymbol{\mu}_2)'(\boldsymbol{\Sigma}^{-1})(\boldsymbol{\mu}_1 - \boldsymbol{\mu}_2) \,. \tag{3.2}$$

$$Z = \frac{n_1 + n_2 - p - 1}{(n_1 + n_2 - 2)p} T^2 \,. \tag{3.3}$$

3.1.2 Wilk's Λ

To discriminate between more than two groups it is desired that the within group variation is small compared to the between groups variation. Wilk's Λ consists in principle of the ratio of the within group variation ($\mathbf{W}$) and the total variation ($\mathbf{T}$), i.e. the within group plus the between group variation, see Equation 3.4. A value of Wilk's Λ which is close to zero indicates that the two groups are well separated.

$$\Lambda = \frac{\det(\mathbf{W})}{\det(\mathbf{T})} \,. \tag{3.4}$$

3.2 Pre-processing

Many statistical methods assume that the data matrix and the reference values are centred, i.e. that the arithmetic mean has been subtracted, see Equation 3.5.

$$\mathbf{X}_c = \mathbf{X} - \boldsymbol{\mu} \, . \tag{3.5}$$

Standard normal variate (SNV) is commonly used as a pre-processing method for normalising spectral data or similar [13, 117]. SNV is performed by subtracting the mean for each sample, and normalising using the standard deviation (SD) of the sample spectrum, see Equation 3.6.

When operating on all samples using values derived from the samples themselves, as in both centring and SNV, the rank of the data matrix usually decreases with 1.

$$\mathbf{X}_{snv} = \frac{\mathbf{X} - \boldsymbol{\mu}}{\boldsymbol{\sigma}} \, . \tag{3.6}$$

Other common pre-processing methods are normalisation, multiplicative scatter correction (MSC), derivation, and the auto-scale (ASC) normalisation [117].

3.3 Calibration and Validation

Statistical models usually require training in order to build a prediction model. Therefore the data is divided into a training set and a test set. This should be done in a random like fashion to avoid getting different structures in the two sets. If one has many samples this is simply done by just randomly dividing the total data set into these two sets, but if only a few samples are available then different schemes for dividing into training and test can be used, e.g. cross validation or bootstrap as described below. The prediction model is first trained on the training set, and then the resulting model is used for prediction on unseen data in the test set. This is a way to see how the model generalises for different data. In comparison to the training prediction error, the test error is usually considered a more honest estimate of the prediction error.

Many statistical models also need calibration of one or several parameters. Therefore, one can further divide the data so that instead of the training and test set, one has a calibration set and a validation set. The calibration set is then usually further divided into a training and test set. The model is then trained and tested repeatedly for different sets of parameter values, and by choosing the parameter giving the best performance, e.g. lowest test error, and then choose the model resulting from using that parameter on the calibration set. Finally, this model is used for prediction on the validation set.

3.3.1 Cross Validation

Cross validation (CV) is a method for estimating prediction error. It can for example be used if there is not enough data to split it into training, test and validation sets. The most common variant of CV is the k-fold CV which divide the data into training and test set using every k:th sample as test, this is then repeated k times and the prediction error estimates for each is combined. Typical choices of k are 5, 7 or 10, and $k = n$ is called leave-one-out cross-validation (LOOCV).

LOOCV uses only one sample as test and this is repeated n times so each sample is used as test only once. This is a computationally expensive method for larger data sets since it iterates n times. An overview of the LOOCV scheme can be seen in Figure 3.1. For LOOCV the error rate is almost unbiased for the true (expected) prediction error, but in this case they could have high variance, since the training sets are so similar to each other [63]. LOOCV has the advantage of repeatable results since it, in contrast to many other CV methods, does not rely on random division of the data.

Repeatability can be assessed using CV by leaving out replicates or groups of samples [18].

3.3.2 Bootstrap

Bootstrap is the practice of estimating properties of an estimator by measuring those properties when sampling from an approximating distribution. The usual way of doing it is by constructing a number of re-samples of the observed data set, obtained by random sampling with replacement from the original data set. The key to the strategy is to create alternative versions of data that "we might have seen". This means that the generated training sets contain some amount of duplicates.

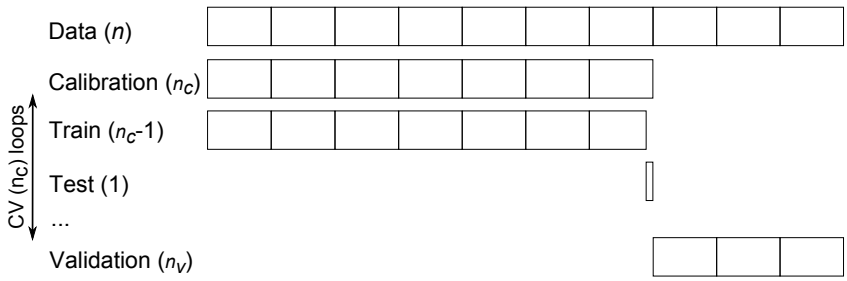

Figure 3.1: Schematic overview of the LOOCV used for calibration and validation of prediction. The calibration set consists of n_c samples, and the validation set of n_v samples. One sample at a time is left out for test in the calibration step.

3.4 Discriminant Analysis

The basic concept of discriminant analysis is to classify data that consist of two or more groups.

The discriminant method trains and builds its model on the training set of $\mathbf{X}$ and corresponding group labels in $\mathbf{y}$. When the method is training it knows about the samples' group belongings, also called a supervised method. In the next step the method validates this model on the test set of $\mathbf{X}$ which hence consists of data unseen to the model and the group labels are unknown for the method. Finally the group labels are used to calculate the classification rate (or some other error rate) of the model.

A traditional strategy for classification is to find a threshold that separates two groups; a decision boundary. Usually this is based on a way of measuring the distance between the two groups, e.g. using Manhattan distance or Euclidean distance, see Equations 3.7 and 3.8.

$$D = |\mathbf{x}_1| - |\mathbf{x}_2| \ . \tag{3.7}$$

$$D = \sqrt{(\mathbf{x}_1 - \mathbf{x}_2)'(\mathbf{x}_1 - \mathbf{x}_2)} \ . \tag{3.8}$$

The Mahalanobis distance is based on the Euclidean distance, see Equation 3.9, also taking the variance and covariance into account. When using two variables ($p = 2$) then the decision boundary is a line, for three variables it is a plane, and for more than three variables the decision boundary is a hyperplane.

Some of the basic and widely used methods of classification are the linear discriminant analysis (LDA) and quadratic discriminant analysis (QDA) [43, 46, 63]. LDA can be seen in Equation 3.10, and QDA is described by Equation 3.11. They are both based on the Mahalanobis distance and assume that the variables in each group are normally (Gaussian) distributed. LDA and QDA are based on a distance-to-the-group mean, weighted by the variance. No calibration is needed since they do not use any parameters.

LDA assumes that the groups' covariance matrices are the same, which furnish a linear decision boundary. In practice, the groups' covariance matrices can be pooled according to Equation 3.1 and used for LDA. On the contrary, for QDA the decision boundary is a quadratic function. An example of LDA and QDA can be seen in Figures 3.2 and 3.3 respectively.

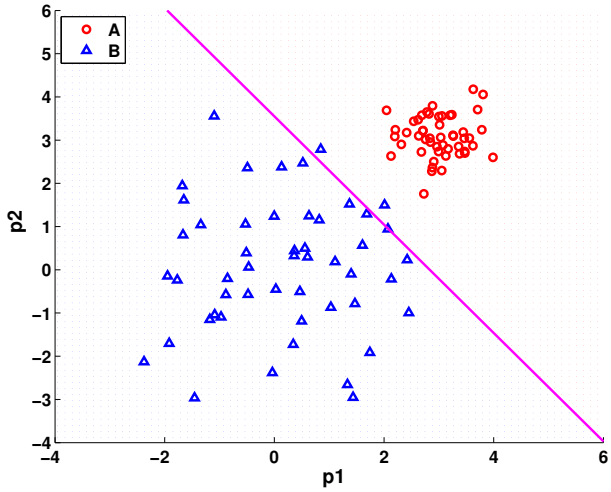

Figure 3.2: Example of classification of two normally distributed groups (A,B) with two variables using LDA. The two groups have different mean and standard deviations, and the decision boundary is shown as a straight line.

S_i is the discriminant score and for LDA it is the negative version of the squared distance between a sample $\mathbf{x}$ and the mean $\boldsymbol{\mu}_i$ of group i plus a prior term. $\boldsymbol{\Sigma}$ is the pooled covariance matrix of each group's covariance $\boldsymbol{\Sigma}_i$. The mean and the covariance matrices are calculated for the training data set, and then S_i is calculated for each group i for all samples in the test set used for classification. The prior distribution of each group is denoted p_i and is commonly the ratio between the number of samples in the group and the total number of samples.

For each sample $\mathbf{x}$ in the test set, its distance to the group mean $\boldsymbol{\mu}_i$ is calculated.

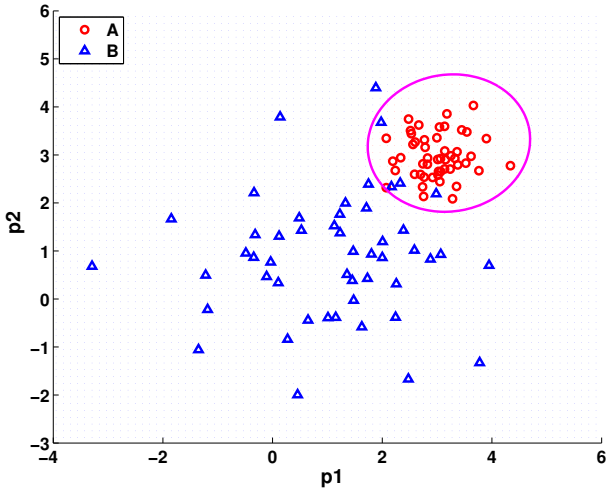

Figure 3.3: Example of classification of two normally distributed groups (A,B) with two variables using QDA. The two groups have different mean and standard deviations, and the decision boundary is shown as a quadratic line.

The highest score is chosen, which is equivalent to the highest probability that the sample belongs to that specific group.

$$D^2 = (\mathbf{x} - \boldsymbol{\mu}_i)' \boldsymbol{\Sigma}^{-1} (\mathbf{x} - \boldsymbol{\mu}_i) \ . \tag{3.9}$$

$$S_i = -\frac{1}{2} (\mathbf{x} - \boldsymbol{\mu}_i)' \boldsymbol{\Sigma}^{-1} (\mathbf{x} - \boldsymbol{\mu}_i) + \ln p_i \ . \tag{3.10}$$

$$S_i = -\frac{1}{2} \ln(\det(\boldsymbol{\Sigma}_i)) - \frac{1}{2} (\mathbf{x} - \boldsymbol{\mu}_i)' \boldsymbol{\Sigma}_i^{-1} (\mathbf{x} - \boldsymbol{\mu}_i) + \ln p_i \ . \tag{3.11}$$

Since the inverse of the covariance matrix $\boldsymbol{\Sigma}$ is used, this demands that the covariance matrix is invertible (nonsingular). This is usually the case if the number of observations is larger than the number of variables ($n > p$). The problem at hand is then called well-posed.

Even if the data is not normally (Gaussian) distributed it turns out that LDA and QDA still performs well in many cases [63].

3.5 Support Vector Machine

The support vector machine (SVM) is a supervised learning technique for discriminant analysis based on the theory of optimal separating hyperplanes (OSH) [63]. While LDA and QDA are based on the distance between a sample and the group mean, SVM is based on the distance to the nearest training data points; the margin. SVM has the option of being non-linear by using a kernel [34].

The basic idea with SVM is to construct an optimal separating hyperplane for the two groups by mapping the data to a higher-dimensional space. This method uses a soft margin to handle the situation of two non-linearly separable groups, meaning that a certain amount of the training samples are allowed to fall on the wrong side of the separating hyperplane which is defined by the slack amount. This situation results in a convex optimisation problem which can be solved by standard methods using quadratic programming.

An ideal example can be seen in Figure 3.4. The vector $\mathbf{w}$ is a normal vector perpendicular to the hyperplane, b is the bias, so the hyperplane is defined by a set of sample points $\mathbf{x}$ satisfying $\mathbf{w} \cdot \mathbf{x} - b = 0$.

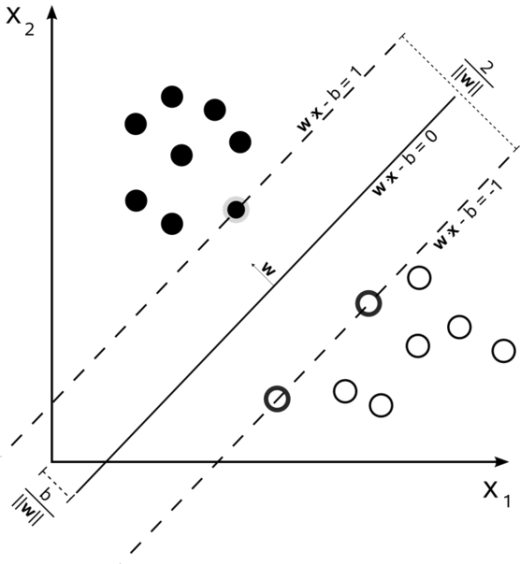

Figure 3.4: Maximum separating hyperplane with margin. The data is linearly separated since no overlap occurs, and no slack amount is needed.

SVM includes a kernel function, responsible for the transformation of the data into a higher-dimensional space. In this way the data is mapped from its orig-

inal input space into the higher-dimensional feature space. Once the data has been mapped, the aim is to train the model to define a separating hyperplane in the feature space so that the data are then mostly separable by a line. One advantage of using a kernel function is that the SVM method can perform classification without ever representing the feature space explicitly, thus reducing the computational cost. The kernel is located at the point of the dot product in the SVM algorithm [63]. In fact all methods that are based on a dot product can make use of kernel functions, where the dot product is replaced by the kernel function.

The Euclidean norm, also called the L_2 norm is based on the Euclidean distance, Equation 3.8, and the norm is shown in Equation 3.12. The L_2 norm measures the length of a vector and is based on the dot product.

$$\|\mathbf{x}\|_2 = \sqrt{\mathbf{x}'\mathbf{x}}\,. \tag{3.12}$$

Popular choices for kernel functions can be seen in Equations 3.13 and 3.14. A d:th degree polynomial is shown in Equation 3.13, and a radial basis function (RBF) can be seen in Equation 3.14. The parameters of variable choice are c (constant), s (linear scaling), d (degree of the polynomial) and γ [69]. The samples from each group are denoted $\mathbf{x}_1$ and $\mathbf{x}_2$ respectively.

$$K(\mathbf{x}_1, \mathbf{x}_2) = (s\langle \mathbf{x}_1 \cdot \mathbf{x}_2 \rangle + c)^d\,. \tag{3.13}$$

$$K(\mathbf{x}_1, \mathbf{x}_2) = \exp(-\gamma \|\mathbf{x}_1 - \mathbf{x}_2\|_2^2)\,. \tag{3.14}$$

The output of the kernel is dependent on the Euclidean distance of $\mathbf{x_1}$ from $\mathbf{x_2}$.

It should be noted that the RBF has a Gaussian form where $\gamma = 1/2\sigma^2$. The centre of the RBF is the support vector and σ will determine the area of influence it has over the data space.

3.6 Principal Component Analysis

Multivariate data, e.g from images, can be analysed using principal component analysis (PCA) for exploratory purposes. PCA is an unsupervised method and the most optimal method with respect to maximising the variance [63] and has been commonly used for dimension reduction to deal with ill-posed problems. If the relation of interest contains large variation, then PCA is a good method

for analysing the data [53]. The data is usually mean centred, and sometimes normalised e.g. using SNV.

PCA is a linear orthogonal transform which means that the transformed data's dimensions are independent (without any covariance/correlation) [113]. It is common to calculate PCA on the covariance matrix or the correlation matrix of the data. Next step is to find a linear transform of the data so that the covariance matrix becomes diagonal, i.e. to find the directions in which the data varies the most. This is usually solved by singular value decomposition (SVD) where the eigenvectors and their eigenvalues are calculated.

The eigenvectors forms the base of the transformed data and are called principal components (PC) (or sometimes latent variables). This is called a diagonalisation of the covariance matrix. The eigenvalues represents the variance along that component, and the first component represents the largest independent variance in the data. It should be noted that the components are formed by linear combinations of all variables in the data.

It is common to use PCA for reducing the dimensionality of data. Since the components are ordered by the amount of independent variance it is often assumed that most of the information can be kept using only the first couple of PCs. By this it is usually assumed that the PCs with the lowest amount of independent variance represent noise.

With these characteristics, PCA is usually used in order to investigate the relation of variables in data, as well as visualising data, or for compression.

3.7 Ordinary Least Squares Regression

Regression analysis consists of finding a relation between continuous reference values ($\mathbf{y}$) and one or many data variables ($\mathbf{X}$). Ordinary least squares (OLS) is a method for estimating a linear regression model, see Equation 3.15 where $\boldsymbol{\beta}$ is the model coefficients and $\boldsymbol{\varepsilon}$ is the offset. OLS calculates the regression model by minimising the sum of squared vertical distances between the observed data $\mathbf{X}$ and the estimated response $\hat{\mathbf{y}}$ [63]. In other words, this is minimising the residual sum of squares (RSS), see Equation 3.16.

$$\mathbf{y} = \mathbf{X}\boldsymbol{\beta} + \boldsymbol{\varepsilon}\,. \tag{3.15}$$

$$RSS = \sum_{n_c} (\mathbf{y} - \hat{\mathbf{y}})^2\,. \tag{3.16}$$

RSS is commonly used as a measure for model selection, since it takes all values in the data into account (and not just an average).

The OLS prediction model consists of as many parameters as the data itself (p), hence one drawback with OLS is the interpretation of the model. With many variables it would be of interest to determine a subset of the variables that exhibit the strongest effect for prediction.

3.8 Partial Least Squares Regression

The partial least squares regression (PLS regression, or PLSR) method [63, 131] is commonly used for regression analysis. It finds a linear regression model by projecting both X and y to a new space. The PLSR algorithm tries to find the directions in the X space that explains the maximum variance direction in the y space. Therefore, PLSR is also known as projection to latent structures regression. PLSR is similar to PCA in that it maximises the variance for orthogonal components consisting of linear combinations of all variables, but since both X and y are projected it is a bilinear factor method. Since PLSR is not scale invariant, the data is usually mean centred or normalised.

The number of components (factors) n_f tested in the calibration step is varied from 1 to a number less than or equal to p. The number of components to be used in the PLSR model can be decided using e.g. LOOCV on the calibration set, while minimising the CV prediction residual sum of squares (PRESS) [60], related to RSS, see Equation 3.17. Selecting the number of components can alternatively be done by minimising the CV mean of the RSS, see Equation 3.16, and to achieve a more parsimonious model the 'one standard error rule' [63] can be used for selection: The least number of components with RSS value inside the range of one standard error of the lowest value of RSS is selected.

$$PRESS_{n_f} = \sum_{n_c} (\mathbf{y} - \hat{\mathbf{y}}_{n_f})^2 \,. \tag{3.17}$$

Using n_f components on the calibration data results by the PLSR algorithm in a prediction model consisting of the coefficients in β. The prediction model is then validated on the validation samples.

The coefficient of determination R^2 is a measure of how much variation is explained by the model and is calculated for the prediction of the validation set. R^2 is basically the ratio of RSS and the total sum of squares (TSS). The R^2 can

be calculated both for calibration and prediction, and the R^2 for prediction on the validation set can be seen in Equation 3.18.

$$R^2 = 1 - \frac{RSS}{TSS} = 1 - \frac{\sum_{n_v}(\mathbf{y} - \hat{\mathbf{y}})^2}{\sum_{n_v}(\mathbf{y} - \frac{1}{n_v}\sum_{n_v}\mathbf{y})^2} \,. \tag{3.18}$$

The standard error of calibration (SEC) can be seen in Equation 3.19. Furthermore, the ratio of the standard error of prediction (RPD) can be calculated as a measure of how well the model predicts [147]. The RPD is the ratio between the standard error of prediction (SEP) and the standard deviation of the original data $\mathbf{y}$ (the reference values), see Equations 3.20 and 3.21.

$$SEC = \sqrt{\frac{PRESS}{n_c - n_f - 1}} \,. \tag{3.19}$$

$$SEP = RMSEP = \sqrt{\frac{1}{n_v}\sum_{n_v}(\mathbf{y} - \hat{\mathbf{y}})^2} \,. \tag{3.20}$$

$$RPD = \frac{SD}{SEP} \,. \tag{3.21}$$

The SEP is equal to the root mean square error of prediction (RMSEP). The advantage with RMSE is that it gives the mean error of the prediction using the same units as the original data. An RPD value of 1.0 means that the model cannot predict accurately, since this means that the mean error is equal to the standard deviation of the reference values. An RPD value higher than 2.5 is considered satisfactory for screening, and values of 5–10 are adequate for quality control according to Williams and Sobering (1993) [147].

3.9 Variable Selection

Interpretation of data is becoming more interesting when the amount of collected data is getting larger. For large data sets a simpler model is preferred. A prediction model containing ten variables is more comprehensible than that with a hundred or a thousand variables. Statistical methods that selects out a set

of interesting variables out of all variables are usually called variable selection, sparse, basis pursuit, or parsimonious methods [41, 63].

When it is easy to capture a large number of variables one can end up in a situation where the number of variables is larger than the number of observations; an ill-posed problem, also called a large p small n problem ($p \gg n$). Traditionally, a common solution to ill-posed problems is to do a PCA and then keep n, or less, number of components which renders a well-posed problem suitable for further statistical analysis. Also PLSR can for some cases be used for ill-posed problems. Potential disadvantages with this approach are that these methods use linear combinations of all variables, and some variance in the data is lost when excluding components.

An alternative approach to ill-posed problems is the so-called sparse methods. Sparse methods do not use linear combinations of all variables. Instead they usually use regularisation to deal with the ill-posed problem and select only a few variables that are included in the model.

3.9.1 LDA Subsets

One method for evaluating important variables is LDA classification on subsets of variables, using subsets with a cardinality of 1 up to p. First, one variable at a time is tested, then all combinations of two variables and so on. The number of combinations for each subset size (cardinality) is equal to the binomial coefficient, using combinations without repetition. In this way it can be investigated which variables, and which combinations of variables, are important for the classification of the groups.

LDA using subsets of samples is combined with CV for training and testing the classification. This method is similar to best subset selection [63] and it can be compared to stepwise selection methods [63] or leaps and bounds [51], with the difference that subset LDA tests all possible combinations. However, LDA using subsets is time consuming for large number of samples, variables and subset size.

3.9.2 Elastic Net

The elastic net (EN) performs a variable selection while doing regression [160]. In contrast with PLSR and similar regression methods it does not use linear combinations of all variables, it uses only a few variables which are found important; non-zero coefficients. By this EN excludes variables that do not contribute to

the result and thus are potential noise. Since only a few variables are selected as is, the EN regression model is easy to interpret. Interpretability is one of the important characteristics of a statistical method.

The EN tends to select variables that are correlated with each other, which is suitable for spectral data with intrinsic correlation.

EN uses two model parameters. The first parameter λ_1 is a factor for an L_1 norm used for determining the number of non-zero coefficients; the number of selected variables (cardinality). The L_1 norm is related to the Manhattan distance in Equation 3.7, and the norm can be seen in Equation 3.22.

$$\|\mathbf{x}\|_1 = \sum_{j=1}^{n} |x_j| \ . \tag{3.22}$$

The second parameter λ_2 is the factor of the Euclidean L_2 norm, see Equation 3.12. The L_2 norm is used for regularisation; dealing with an eventual ill-posed problem.

The EN regression model consists of the variable weights in $\boldsymbol{\beta}^{en}$, see Equation 3.23.

$$\beta_j^{en} = \underset{\beta_j}{\operatorname{argmin}} \left(\|\mathbf{y} - \mathbf{X}\beta_j\|_2^2 + \lambda_2 \|\beta_j\|_2^2 + \lambda_1 \|\beta_j\|_1 \right) \ . \tag{3.23}$$

The estimated coefficients in $\boldsymbol{\beta}^{en}$ are then multiplied (scaled) by $(1 + \lambda_2)$ to get the final EN solution.

The data $\mathbf{X}$ is normalised and the reference values $\mathbf{y}$ are centred.

The two parameters can be selected by using CV or similar on the calibration set, in order to try all combinations of the two parameters. The optimal parameter set can in this way be chosen by minimising RSS on the calibration set. If more than one combination of number of variables and λ_2 is found to give the best calibration result, then the lowest number of variables and the highest value of λ_2 can be used; giving the least complex model.

EN is a combination of two earlier methods, the least absolute shrinkage and selection operator (LASSO) [137] and ridge regression (RR) [65]. The LASSO uses the L_1 norm for variable selection and its solution can thus be obtained with EN by setting λ_2 to 0. RR uses the L_2 norm for regularisation, so EN is

combining these two nice properties of variable selection and regularisation into one method.

One of the advantages with the EN is that it tends to select groups of variables that are correlated. In comparison, the LASSO usually only selects one of them. However, the selecting of groups of variables implies that an appropriate number of non-zero coefficients are needed to include the relevant clusters.

The L_1 norm is sometimes referred to as the Manhattan distance or taxi cab geometry since its unity circle is a square, see Figure 3.5. It is commonly used for variable selection, and it might be abstract to understand but the exclusion of a variable happens when the solution touches a corner of the L_1 norm. Since the combination of L_1 and L_2 also has corners those are in charge of the variable selection, see Figure 3.5. Figure 3.5 shows the unity circles of L_1 and L_2 norms, as well as a combination of the two with power between 1 and 2, which has a unity circle in between.

In comparison to e.g. PLSR and similar methods, EN does not produce linear combinations of variables but selecting variables as is, which helps interpretation of the model.

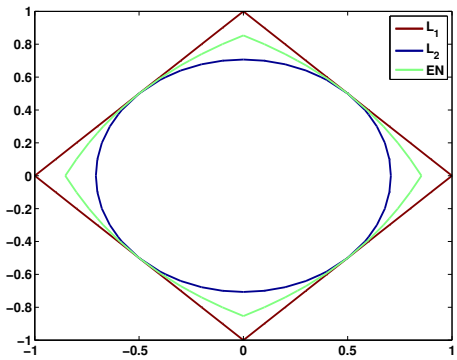

Figure 3.5: Unity circle using L_1 norm, L_2 norm, and the combination of L_1 and L_2 used in EN.

3.9.3 Sparse Discriminant Analysis

SLDA is designed for ill-posed problems and uses a modified version of EN for variable selection [160].

The SLDA algorithm calculates sparse discriminant component(s) that gives the

best classification of the groups. The number of components is one less than the number of groups. The data is then projected onto these components and classified using a simple classifier such as a threshold or an LDA.

3.10 Filter Selection

When dealing with spectral data it is usually some specific regions of the spectra that are of importance for the analysis, so instead of selecting a number of variables one can try to select entire ranges. A method for designing optical filters is described here, and the method is aimed at selecting a number of ideal rectangle-shaped band pass filters (BPF) as described in Kobayashi et al. (2011) [76] and Nakauchi et al. (2012) [102]. The filter properties consists of the centre wavelength (λ_c) and the half-bandwidth (w_h).

The filter design method integrates all spectral bands in the current filter range in order to simulate an optical filter. It then uses OLS regression while iteratively trying to find optimal filter parameters by minimising root-mean-square error of cross-validation (RMSECV). The method chooses a centre wavelength and width for the BPF. When the first BPF is found it is fixed while choosing the second one, and so forth. Stepwise random selection is used, as described in point 1-9 in [76].

Since the algorithm uses random selection, many iterations is to be preferred. Also, it is desirable to limit the size of the filters, both in respect to how optical filters are constructed, and also to reduce the number of possible combinations of BPFs. The number of possible combinations of 3 BPFs is approximately 10^{12}.

Chapter 4

Experimental Work

This chapter gives an overview of the studies presented in the published contributions in Part II, with discussion and summary of the results.

Three main areas within aquaculture have been investigated: the size of fish feed pellets, astaxanthin coating on fish feed pellets, and astaxanthin presence in salmonid fish. All studies used images captured with the VideometerLab device [23]. In the pellet size study grey-scale images were acquired, while the other studies used multi-spectral images. Furthermore, hyper-spectral images of astaxanthin coating were captured using a Specim SWIR (NIR) line-scan camera with a MCT sensor, and the novel SuperK set-up with diffused laser light. The images were used together with additional measurements of quality parameters such as pellet size, chemical measurements of astaxanthin and surface colour. In some cases the knowledge of astaxanthin type was used as label parameters. An overview of the data sets can be seen in Table 4.1, together with an overview of the spectral imaging equipment used in Table 4.2.

The performance of the spectral imaging devices used in this thesis has been validated previously for similar surface chemistry applications. The VideometerLab has been successfully used in food applications [24, 25, 26, 29, 37, 39, 40, 58, 94, 118], medical applications [31, 32, 56, 119], and sand measurement [30, 62]. The Specim SWIR set-up has been validated for food applications [73, 74]. The novel SuperK set-up has not previously been used for full-field images, but it has

Table 4.1: All data sets used in this thesis with their range of spectral imaging (nm), reference data and corresponding Appendix.

Sample type	Spectral range (nm)	Reference data	App.
Pellets	-	Diameter, length, time	A
Pellets	385-1050	Synthetic astaxanthin concentration	B
Pellets	385-1050	Synthetic astaxanthin concentration, astaxanthin type, pellet recipe	C
Pellets	385-1050 970-2500	Synthetic astaxanthin concentration	D
Pellets	385-1050 455-1015	Synthetic astaxanthin concentration	E
Fish	385-1050	Astaxanthin type, astaxanthin concentration, surface colour	F

Table 4.2: The spectral imaging devices used in this thesis with their spectral range, number of spectral bands and image size in pixels.

Device name	Spectral range (nm)	Spectral bands	Image size
VideometerLab	385-1050	20	1280×960 [1]
Specim SWIR	970-2500	256	320 (line)
SuperK	455-1015	113	1600×1200

[1] In Paper E a configuration of 1200×1200 was used.

been validated for measurements of diffuse reflectance, also known as sub-surface laser scattering (SLS), with dairy products as case [104].

Machine vision and spectral imaging has previously been used for biological applications where it is of interest to detect subtle differences in colour and surface chemistry. Vision systems are suitable for quality inspection in the food and feed industry since they provide non-destructive and non-contact testing, which is of paramount importance in this field. Spectral imaging has specifically been practised for quality assurance of food and feed products [14, 19, 50, 54, 68, 134], with food applications such as poultry [80, 110], fish fillets [37, 129, 132, 133, 149], beef [26, 73, 74], minced meat [25, 40], barley [7], maize kernels [78], vegetables [14, 29], microbial growth [75], and apples [140]. Spectral imaging is not as commonly used previously for animal feed applications, but there are studies on classifying the type of constituents used in feed [45, 114, 116, 155], and detecting contamination of farm feed [84, 124, 143, 154].

The colour of salmonid fish fillets has previously been inspected by tricolour measurements [27, 151], tricolour imaging [64, 99, 151, 152], and spectroscopy [17, 47, 109, 148]. Dissing et al. (2011) [37] predicted natural astaxanthin concentration levels in salmonid fish fillets by multi-spectral images from the VideometerLab, but besides this there are no other studies in the literature on measuring the pigmentation of salmonid fish by spectral imaging.

In the Ph.D. thesis of Dissing (2011) [39] many different food applications were analysed using the multi-spectral VideometerLab device. This thesis differs from that of Dissing since it is aimed specifically at aquaculture applications and use three different types of spectral imaging equipment.

In this thesis spectral imaging on feed pellets was accomplished, which has not been documented in the literature before. While pharmaceutical pellet coating has been analysed by image analysis and spectral imaging [120], coating of feed pellets by spectral image analysis as furnished here, has not previously been reported. Astaxanthin use for feed production and pellet coating has not been analysed by image analysis previously in the literature. Classification between salmonid fish that has eaten natural or synthetic astaxanthin has been done previously by liquid chromatography [139], whereas in this thesis it is done by spectral imaging.

4.1 Pellet Size

The aquaculture feed production industry is confronted by the challenge during production of controlling the size of the pellets. The problem is due to temperature and pressure changes in the extrusion process, as described in Section 1.1 Page 3.

In the aquaculture industry it is of high importance that the fish receive feed of proper size. The size of the pellets is adapted to the size of the fish so that the fish are able to eat the feed properly and grow as expected. It has been shown that the growth rate of fish is closely related to the pellet size of the feed [8, 136, 145]. Therefore, when producing feed pellets for aquaculture there is a need to control the size of the output product.

By using image analysis of a large amount of piled pellets it is possible to predict the average pellet size. Measuring the size distribution of small particles is often referred to as granulometry or sometimes as particle size distribution analysis [96, 97]. The method used here was based on mathematical morphological operations; the opening operation which consists of an erosion followed by a dilation operation [122]. A disk was used as a structuring element because of its symmetrical shape. The opening result was analysed using a kind of derivative called pattern spectrum (PS) [95]. These are well-used methods for calculating particle size distribution and are usually performed on segmented objects, but here this method was applied on images of disordered and overlapping pellets.

The pellets use both diameter and length for size measurements. The diameter is the specified product size and thus the most important size parameter for the industry. It was shown that both the diameter and length increase with time during pellet production so therefore a general size measurement based on the visible pellet area was feasible. The image analysis results were compared to the pellet size measured with a calliper.

For comparison, and showing the principle of the method, an example is shown with segmented binary images of the same pellets as used in batch D in Paper A Page 65 which have a target diameter of 3.0 mm. The size change during a 45 minute batch production can be seen by comparing the images in Figures 4.1 and 4.2. The same images using the opening operation with a disk of radius 21 pixels (∼3.0 mm diameter) can be seen in Figures 4.3 and 4.4. The opening operation is showing if a disk of the specified size can fit inside the object. Hence, if the pellet is smaller than the disk it will be removed from the image. The corresponding PS showing the estimated general size distribution of pellet area can be seen in Figure 4.5, which shows similar tendencies as the pattern spectrum of disordered pellets shown in Figure 4.6 from Paper A.

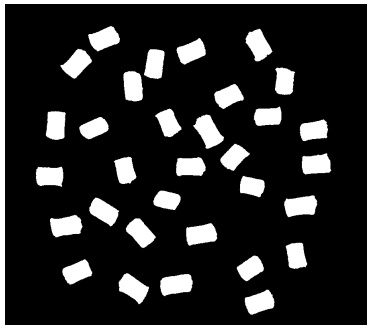

Figure 4.1: Segmented pellets at the beginning of the production process. These are example pellets from batch D in Paper A.

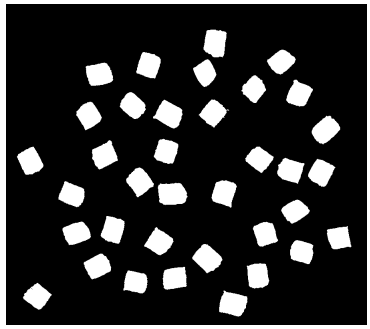

Figure 4.2: Segmented pellets at the end of the production process. These are example pellets from batch D in Paper A.

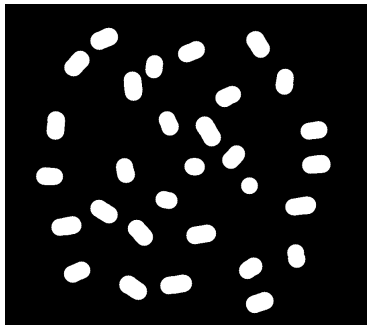

Figure 4.3: The opening operation calculated on the image in Figure 4.1 with segmented pellets at the beginning of the production process. A disk of 21 pixel radius (∼3.0 mm diameter) is used as structuring element.

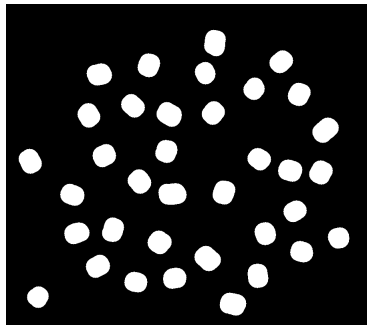

Figure 4.4: The opening operation calculated on the image in Figure 4.2 with segmented pellets at the end of the production process. A disk of 21 pixel radius (∼3.0 mm diameter) is used as structuring element.

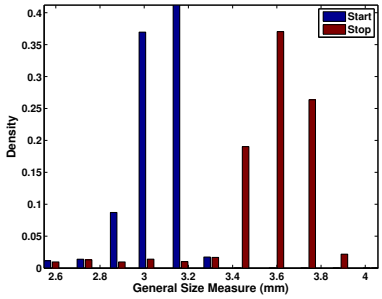

Figure 4.5: The pattern spectrum for the beginning and end of the production, calculated on the images with segmented pellets in Figures 4.1 and 4.2.

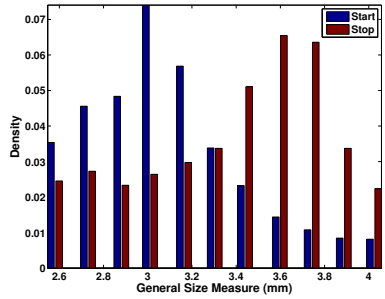

Figure 4.6: The pattern spectrum for the beginning and end of the production, using images of disordered pellets in Paper A.

In the proposed method, no image object segmentation is needed. The results show that it is possible to extract a general size distribution from an image of piled disordered pellets representing both length and diameter of the pellets in combination as an area using the grey-scale image opening operation, as can be seen in Paper A. An overview of the size index method can be seen in Figure 4.7.

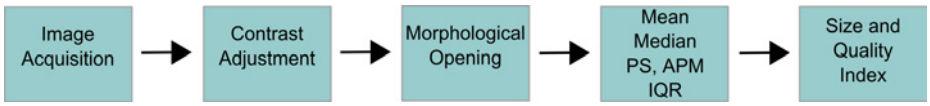

Figure 4.7: Overview of the pellet size method used. The size index is calculated using one of the methods mean, median or the pattern spectrum maximum (APM). The pattern spectrum (PS) is used as a size distribution estimate. The interquartile range (IQR) is calculated to get a measurement of the spread of the size distribution and as another quality measure.

4.2 Astaxanthin Coating

Fish feed pellets are coated with fish oil with added astaxanthin, as described in Section 1.1. Astaxanthin cannot be synthesised in animals and humans so the only way to obtain it is through the diet. Astaxanthin is very expensive; it is usually the most expensive ingredient in the feed at the same time as it is the ingredient of smallest amount. Astaxanthin is added as a coating on the

feed pellets after the extrusion step. Fish oil with added astaxanthin is used for the coating and the concentration level of astaxanthin is measured in mass in mg/kg or as parts per million (ppm). Some amount of astaxanthin is lost in the production since not all of the coating oil ends up on the pellets. Because of this and the high cost, there is a need for optimising quantities of astaxanthin used in the fish feed production.

Astaxanthin is a carotenoid and belongs to the class of phytochemicals known as terpenes, and also classified as a xanthophyll. It is colourful and regarded as a pigment and an antioxidant. The European Commission categorise astaxanthin as a food additive colour with the E-number E161j. The colour and antioxidant function of astaxanthin is due to the extended chain of conjugated (alternating double and single) double bonds at the centre of the compound. As many carotenoids it is soluble in lipids.

The primary natural and original source of astaxanthin is the microalgae *Haematococcus pluvialis* where it exists in esterified form, while it can also be found in *Phaffia* yeast [20, 70, 71]. Astaxanthin can also naturally be found in the flower called Autumn Adonis (*Adonis annua*) [123].

Astaxanthin has a type of red colour and examples of natural astaxanthin in oil, synthetic astaxanthin and ordinary fish oil can be seen in Figures 4.8, 4.9, and 4.10.

Figure 4.8: Natural astaxanthin solved in oil in a petri dish, shown in an sRGB version of a multi-spectral VideometerLab image.

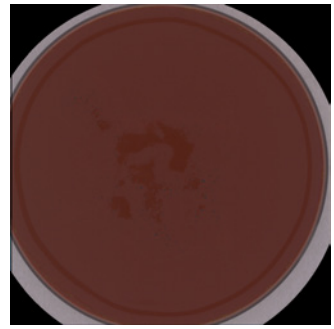

Figure 4.9: Synthetic astaxanthin solved in water in a petri dish, shown in an sRGB version of a multi-spectral VideometerLab image.

When capturing spectral images of fish feed pellets coated with fish oil with added astaxanthin, the acquired reflection spectrum is a mix of the astaxanthin, the fish oil and the underlying pellet recipe. This mix is due to the light

Figure 4.10: Fish oil in a petri dish, shown in an sRGB version of a multi-spectral VideometerLab image.

scattering taking place in the surface material, and eventually also in the underlying material (the pellet), see Figure 4.11. It is possible that the fish oil and the pellet recipe are making spectral responses that partly occlude the spectral characteristics of astaxanthin.

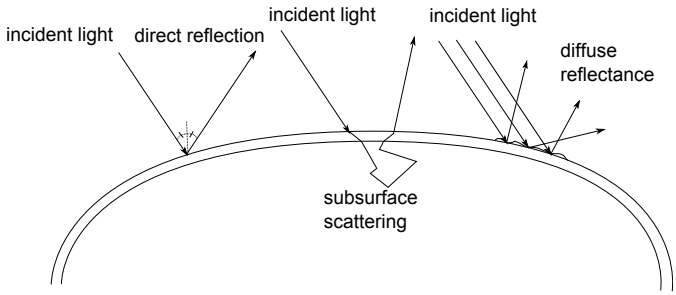

Figure 4.11: Schematic figure of how incident light is reflected or refracted in surface material. Direct reflection, subsurface scattering and diffuse reflection are shown.

The absorption spectra of natural and synthetic astaxanthin solved in fish oil was captured, along with the spectrum for plain fish oil. The spectra were captured in the visual and NIR range using a NIRSystems 6500 absorption spectrometer. The absorption spectra were transformed to reflection values using the standard relation $A = -\log(R)$, where A is the absorption value and R is the reflection value. The resulting spectra is used in the astaxanthin coating studies in this thesis, and was also used in part in [37]. It shows a clear separation between natural astaxanthin, synthetic astaxanthin, and plain fish oil in the visible range of 450-650 nm, as well as some separation in the NIR range e.g. around 900 nm and 1200-1600 nm. The full range captured spectra with all types can be seen

in Figure 4.12.

Investigation of the spectral properties of astaxanthin in the NIR range above 1000 nm has also been done by Yamane et al. (1996), who measured absorbance in the range of 1100-2500 nm using a spectrophotometer [153], and Amarie et al. (2010), who used a spectrometer up to about 1400 nm [3]. Our obtained spectrometer spectra corresponds fairly well to previous studies of astaxanthin [3, 21, 156], who found absorbance peaks of astaxanthin in the visible range around 450-505 nm and secondary peaks around 500-600 nm for various solvents. In the NIR regime they found peaks at 870 nm, as well as 1160-1300 nm, 1916 nm, and 2480 nm. However, none of these studies investigated the difference between astaxanthin and fish oil.

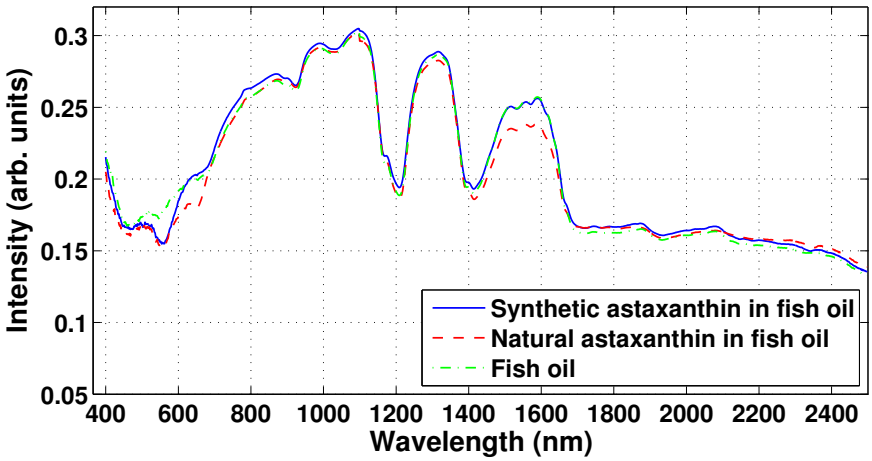

Figure 4.12: Spectrometer spectra of synthetic astaxanthin in fish oil, natural astaxanthin in fish oil, and plain fish oil. The spectrometer absorbance values have here been converted to reflectance.

4.2.1 Overview

Initially, it was tested if it is possible to discriminate between pellets with (50 ppm) and without (0 ppm) synthetic astaxanthin coating using multi-spectral VideometerLab images of pellets lying on their side. If this were possible then further analysis of astaxanthin content would be conducted and based on the results. The multi-spectral images captured reflectance in 20 wavelengths in the range of 385-1050 nm. Two different pellet recipes with synthetic astaxanthin coating were tested in this study. The advantage of having all of the pellets lying

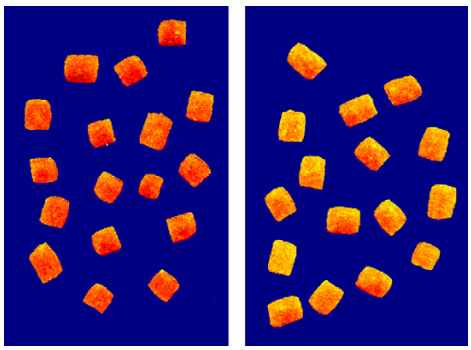

Figure 4.13: PC2 of a PCA of the multi-spectral image of EcoLife20 pellets in Paper B. Pellets coated with synthetic astaxanthin in fish oil (left), and pellets coated with fish oil (right).

on their side is a data set with less variation in the spectral reflection values, but the disadvantage is that it is not how the pellets appear in the production where they are disordered in piles of many pellets. The spectral values (pixels) from the multi-spectral images were compiled using summary statistics for each pellet: mean, median, variance, skewness, kurtosis, and maximum value. Classification using LDA on pellet mean or median values showed overall best results. PCA analysis showed that the second largest variance component in the images is due to the astaxanthin coating, see Figure 4.13. This study showed that it is possible to discriminate between coating with and without astaxanthin coating by multi-spectral imaging, which is a good base for further prediction of astaxanthin concentration level. Furthermore, it showed the importance of having the same pellet recipe and production batch as base since some of the differences detected was possibly not caused by the difference in astaxanthin coating but also differences in the underlying pellet. This study is in Paper B Page 87.

The concentration level of the astaxanthin coating is the most important astaxanthin quality parameter for the pellet industry; therefore it was investigated if it is possible to predict the synthetic astaxanthin coating concentration level by spectral imaging. Moreover, it was also investigated if it is possible not only to predict using pellets lying on their side, but also using disordered pellets in a pile or a filled bin. An example of disordered pellets coated with different concentration levels of synthetic astaxanthin can be seen in Figure 4.14. In the industry many different pellet recipes are used, and any one recipe can contain varying raw materials depending on availability and price. Therefore it is of interest to assess a robust model for astaxanthin concentration prediction which is not affected by the underlying compound. For this purpose, four different

pellet recipes were used in this study. Synthetic astaxanthin coating concentration level on four pellet recipes and multi-spectral VideometerLab images in the visual and part of the NIR range (385-1050 nm) were predicted in Paper C Page 101.

The disordered pellet images represent how the pellets appear in the manufacturing process and instead of segmenting each pellet those images were analysed using non-overlapping image subregions, also called macropixels or disjoint blocks [61, 119].

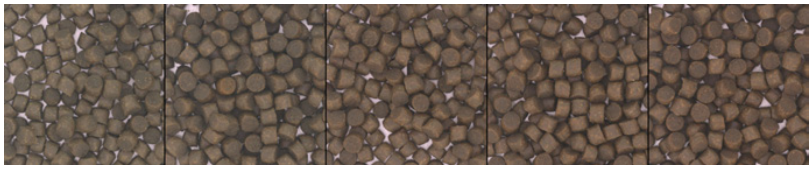

Figure 4.14: SRGB version of VideometerLab images of disordered pellets with the coating concentration level of synthetic astaxanthin from left to right: 0, 20, 40, 60, 80 ppm. Image from Paper C.

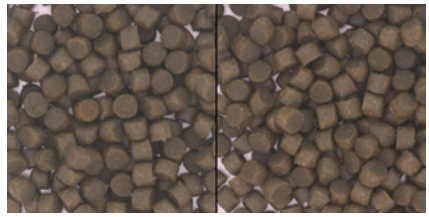

Figure 4.15: SRGB version of VideometerLab images of disordered pellets coated with synthetic astaxanthin (left), and natural astaxanthin (right), both with 20 ppm. Image from Paper C.

The results show that it is possible to predict the level of synthetic astaxanthin coating using PLS regression on each recipe separately. Addressing the robustness of prediction with respect to the underlying pellet compound, it also shows that it is possible to predict the concentration level independent of recipe, when using a model calibrated on all recipes. The concentration prediction is good enough for screening for all recipes, and suitable for quality control for two recipes. Also it shows that a filled dish of disordered pellets can be used for the inspection tasks. The most important spectral bands for astaxanthin concentration prediction are in the visible range of 400-600 nm, as well as just above 900 nm, with the large peaks around 450-505 nm. This corresponds well to the separation shown in the spectrometer spectra in Figure 4.12.

Natural astaxanthin is an important ingredient for organic fish feed production.

Since natural astaxanthin is not always available in large amounts in the market, only one coating concentration level was done using natural astaxanthin. It was therefore investigated if it is possible to predict the difference between pellets coated with natural astaxanthin and pellets coated with synthetic astaxanthin. An example of pellets coated with natural and synthetic astaxanthin can be seen in Figure 4.15. Since astaxanthin is naturally dissolved in oil and synthetic astaxanthin is furnished dissolved in water, the synthetic astaxanthin was centrifuged in order to dissolve it in oil. Consequently, it was also investigated if it is possible to discriminate between pellets coated with synthetic astaxanthin and centrifuged synthetic astaxanthin. The results show that it is possible to predict the type of astaxanthin used in the coating using discriminant analysis. The most selected spectral bands for astaxanthin prediction are in the visible range of 450-600 nm, as well as NIR bands just above 900 nm. This was part of the study in Paper C.

Coating concentration prediction was further studied using hyper-spectral imaging in the NIR range of 970-2500 nm. Since the spectrometer spectra showed some difference between the coating types in the NIR range this was of interest to investigate further using spectral imaging. Also a dense set of 256 spectral bands was used. The results show that it is possible to predict the level of synthetic astaxanthin coating using either hyper-spectral imaging or three simulated filters. Both PLSR and the filter design method put emphasis on the wavelengths found to be important for astaxanthin spectral characteristics, mostly between 1400 and 1600 nm. The prediction error for PLSR is lower than the error for the filter design results. However, the filters are easier to implement for industrial quality inspection [73, 76, 102]. This investigation was done in Paper D Page 133.

Finally, prediction of synthetic astaxanthin coating concentration was performed using hyper-spectral imaging in the visual and part of the NIR range. Here, a new instrument for hyper-spectral imaging was introduced: the SuperK set-up. It is based on a spectral broad laser light source and was used together with a parallel study with the commercially available multi-spectral VideometerLab imaging system. This was a comparison only for astaxanthin prediction and does not investigate how the two systems compare in general. It was concluded that the new SuperK system can be used for chemical surface inspection using hyper-spectral image analysis with very good results.

The results show that it is possible to predict the synthetic astaxanthin concentration in the coating well enough for quality control using both multi- and hyper-spectral image analysis. It shows that the SuperK and VideometerLab devices perform about equally well predicting the synthetic astaxanthin concentration in the pellets, by only measuring surface reflections. This also implies that the presented devices and methods can be used in general for quality inspec-

tion of various coating substances using similar coating techniques. In addition, the higher spectral resolution of the SuperK system combined with sparse statistics for analysing the image data made it possible to identify the most significant spectral regions for the particular detection of astaxanthin, see Paper E Page 151.

4.2.2 Statistical Methods Used

In the initial study, in Paper B, the statistical methods LDA, QDA and SVM with kernels were used. Also PCA with SNV normalisation was done, using the five first PCs for classification. The first five PCs explain a vast majority of the variance, but since many PCs are left out this means that some of the variance is not present in the following classification. PCA is appropriate to use in this way if the PCs left out only contains noise, but if parts of the important variance were left out when excluding components then the classification is not improved by the PCA step. This is crucial, since the variance is an important part of the LDA and QDA classifier, as described in Section 3.4 Page 27. This might be an explanation of why discriminant analysis on PC1-5 gives the highest classification error for both pellet types and all presented classification methods except one.

In most of the tests LDA performed better than QDA, which was interpreted such that the problem is linear. This could also be explained by the fact that QDA uses two covariance matrices and thus need more samples to become stable. By the recommendations [34, 46] of $10p^2$ observations; for 20 variables a data set of 4000 samples should be used, while in this study there was $\sim$2000 samples per test.

Using SVM for classification of astaxanthin presence in pellet coatings did not show as good overall results as LDA and QDA. SVM using kernels is a non-linear method, while LDA is a linear method. Hence, an LDA model is easier to interpret than SVM with kernels.

While ordinary LDA performs well in many cases, it was also compared to SLDA and LDA using subsets in Paper C. SLDA was used for variable selection when performing classification. LDA using subsets finds combinations of two or three spectral bands which could perform the best classification. In this way a good indication which spectral bands are important for the particular problem is achieved. Ordinary LDA produces a loading vector that can give a hint of the variable importance, and while sparse prediction methods do not always give better results, their prediction models are easier to interpret.

For predicting the astaxanthin coating concentration level several regression methods were used. PLSR is commonly used in chemometrics and other fields, and has successfully been used for natural astaxanthin concentration prediction in salmonid fish fillets [37]. PLSR was used here in all three papers predicting the concentration level, see Papers C, D, and E. Also iPLS was used to explore the spectral range in Paper E, indicating the same important region as the other methods also detected.

Moreover, the OLS regression was used in a filter design method formed to find optimum filter ranges for prediction using the spectral data, see Paper D. Continuing with sparse statistical methods, EN was used for regression of astaxanthin coating concentration in order to interpret the spectral data in Paper E. Both the filter design and EN results were compared to PLSR results.

EN regression implies calibration of two parameters, which was performed using two LOOCV and choosing the combination of parameters with the lowest RSS. Example of error maps can be seen in Figures 4.16 and 4.17, where the combination of L_1 and L_2 norm parameters, the number of selected variables and λ_2, form surface maps. The error maps are from the data in Paper E, and show structures with high and low error for different parameter combinations.

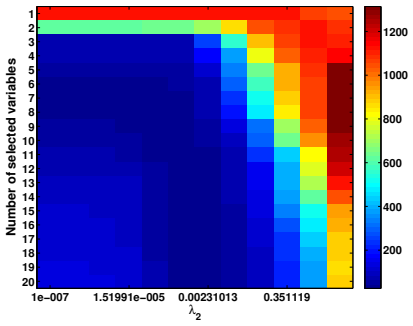

Figure 4.16: EN regression calibration by minimising RSS, done by one LOOCV for each of the two parameters; the number of selected variables and λ_2. This is the calibration error map for the VideometerLab data in Paper E.

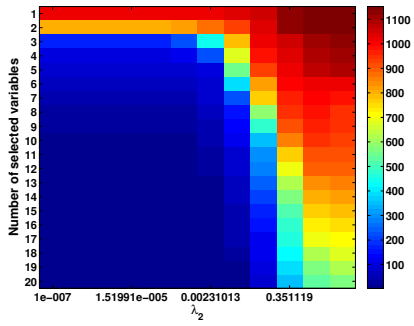

Figure 4.17: EN regression calibration by minimising RSS, done by one LOOCV for each of the two parameters; the number of selected variables and λ_2. This is the calibration error map for the SuperK data in Paper E.

The filter design method for selecting optimal optical filters, described in Section 3.10 Page 38, also uses two parameters. And also here as with EN, it is not possible to test all possible values and combinations; therefore stepwise random selection was used in order to search for the most optimal spectral position and

width of a filter. In Figures 4.18, 4.19, and 4.20, it can be seen that when the first filter is decided the optimal range of parameters for the next filter is vastly reduced. This implies that perhaps not as many search iterations are needed in the succeeding steps. The error maps are from the Specim data in Paper D.

In Paper E the PLSR model was used for predicting and visualising the astaxanthin concentration distribution pixel-wise in the pellet images. Other works on spectral imaging have also done this; trained a statistical model on region average spectra and then applied it to unseen images pixel-wise. It is debated whether it is correct to do so or not, so it is recommended to train and predict using the same type of features. However, this should only be seen as a visualisation.

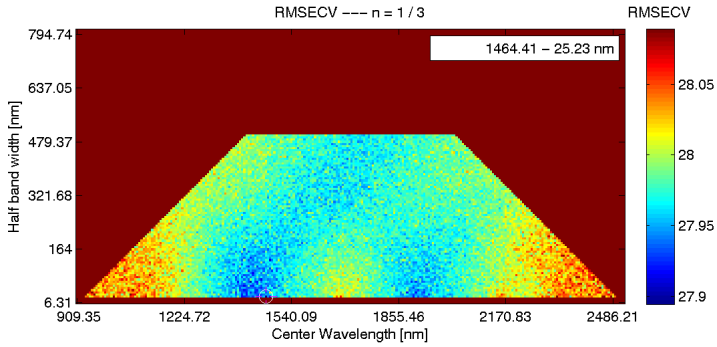

Figure 4.18: Filter design by stepwise random selection and minimising RMSECV for the 1st filter. This is the error map for the Specim data in Paper D.

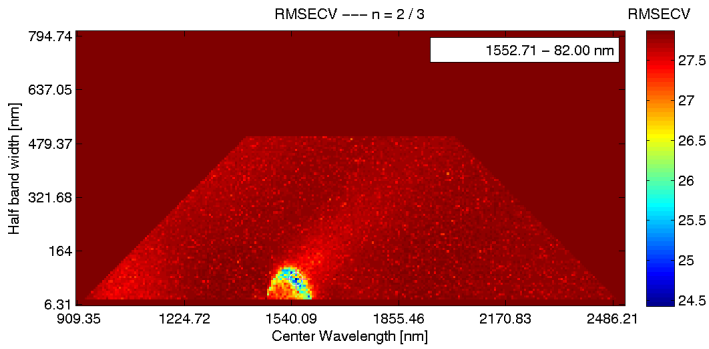

Figure 4.19: Filter design by stepwise random selection and minimising RMSECV for the 2nd filter. This is the error map for the Specim data in Paper D.

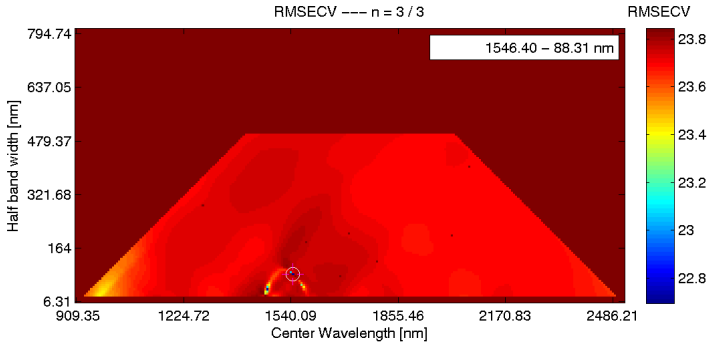

Figure 4.20: Filter design by stepwise random selection and minimising RMSECV for the 3rd filter. This is the error map for the Specim data in Paper D.

4.3 Astaxanthin in Salmonid Fish

The colour of salmonid fish is one of the most important quality parameters for customers, as mentioned in Section 1.1. Using pellets coated with astaxanthin, the astaxanthin colouration of the fish was assessed. It was investigated how natural and synthetic astaxanthin give different fish meat colour. The goal was to be able to differentiate between fish having been fed with natural and synthetic astaxanthin, since the organic salmonid fish market has to use natural astaxanthin in the feed. Furthermore, it was tested whether the best predictions come from vision analysis of the steak biopsy or the fillet of the fish.

The fish colour was measured using three different systems: multi-spectral imaging using the VideometerLab, CIELAB point measure using a Minolta Chroma Meter, and also by using visual judgement with a SalmonFan. The SalmoFan is commonly used in the industry and requires manual inspection and subjective judgement. The VideometerLab records 20 spectral bands, the tricolour CIELAB device measures three visible light variables, and the SalmoFan uses one variable for the colour intensity of the fish. In this way three different colour inspection methods with different number of variables were used.

A total of 45 rainbow trout (*Oncorhynchus mykiss*) were used in the study. The fish were bread in indoor tanks holding 15° Celsius, and they were segregated intro three holding tanks with 15 fish in each tank, resulting in three groups of fish:

- Control: Fish fed with feed using no additional astaxanthin.

- Natural: Fish fed with feed coated with 25 ppm of natural astaxanthin.
- Synthetic: Fish fed with feed coated with 25 ppm of synthetic astaxanthin.

Each fish was cleaned and de-headed before cut into both a steak and fillet. Two biopsies, left and right, were done for each steak. After cutting, the samples were placed in plastic petri dishes and inspected by the three vision systems respectively.

Finally, the chemical content of astaxanthin was determined using high pressure liquid chromatography (HPLC) analysis. The HPLC results show that the average astaxanthin content is different between the three groups. Especially between the natural and synthetic astaxanthin group there is a large difference in average astaxanthin concentration. Also, a large variation of astaxanthin content between the fish was found.

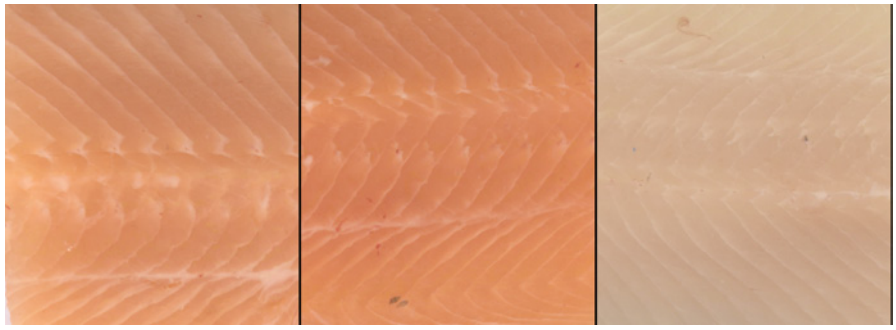

Figure 4.21: Trout fillet images of the three different groups: Fish fed with feed using natural astaxanthin (left), synthetic astaxanthin (middle), and no additional astaxanthin (right). Here showing cropped sRGB representations of the multi-spectral VideometerLab images from Paper F.

Examples of multi-spectral images of fish fillet with different astaxanthin type pigmentation can be seen in sRGB in Figure 4.21. The region of interest (ROI) in each fillet image was segmented using the first factor of the maximum autocorrelation factor (MAF) method [135]. The spectral images were normalised using SNV on pixels and features used were mean spectra and percentiles. Sparse statistics using SLDA was performed in order to discriminate between fish meat from fish fed with synthetic astaxanthin, natural astaxanthin and no astaxanthin. SLDA was compared to using LDA with subsets.

The spectral response of astaxanthin in fish meat is different from that of astaxanthin in oil due to how the astaxanthin is bind in the flesh. This means

that the prediction model of astaxanthin in fish meat would be different from the prediction model for astaxanthin coating of fish feed pellets.

Also, the CIELAB values of the fish meat was compared with using an ordinary SalmoFan sensor panel, with LDA and QDA classification.

Because of the relatively few samples, all classification methods were repeated by doing a bootstrap with randomly chosen sets for 50-100 iterations and calculating the mean of the classifications. In this way it is possible to get an indication on how the prediction methods generalise.

The results show that the control group, which was not fed with astaxanthin, is quite easy to separate from the two astaxanthin groups, while it is more difficult to separate the natural and synthetic groups, as can be seen in Figure 4.22. See Paper F Page 189.

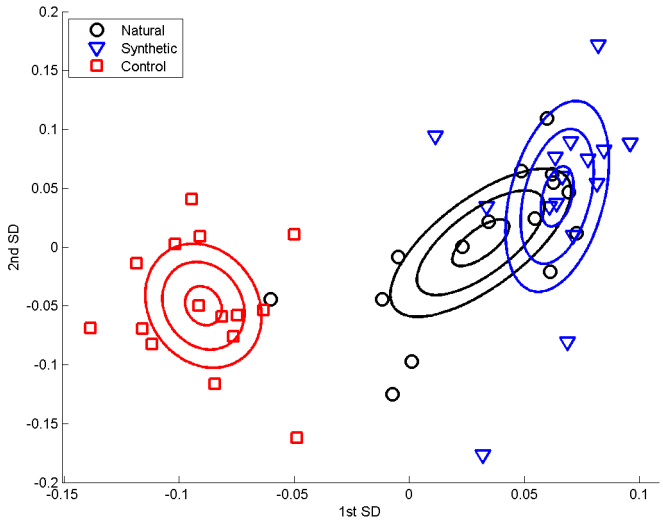

Figure 4.22: The three groups of rainbow trout fed with natural astaxanthin, synthetic astaxanthin, and no astaxanthin (control group) respectively, data from Paper F. The samples are plotted using the two sparse discriminant components from SLDA, and estimated normal distribution contours are visualised for each group.

With relatively few samples and large variation within the groups with regards to astaxanthin content this classification is challenging. Even though normalisation was used in order to reduce the effect of different concentration level

between the groups, it is hard to reduce the difference completely. We cannot exclude the cause of concentration level completely in the results. An apparent overlap of synthetic and natural astaxanthin groups can be seen in the presented scatter plots, and it is possible that the classification is distinguishing the groups dependent on concentration level. However, when compensating for the concentration difference by using OLS regression residuals in the classification the results were still not improved.

Using tricolour CIELAB measurements it shows that the classification of natural and synthetic astaxanthin is slightly better using the steak than the fillet. For discriminating between fish fed with natural and synthetic astaxanthin the CIELAB measurements show better performance than the SalmoFan values. Using spectral imaging, the results show that fillet is better than steak for classifying between synthetic and natural astaxanthin. Machine vision seems to be a good and automatic alternative to the SalmoFan, and also a potential resource for inspecting the type of pigmentation in salmonid fish.

4.4 Industrial Implementation

In order for the measurements to be at-line or on-line there is a need for them to be fast and practical. Capturing a multi-spectral image with the VideometerLab using 20 spectral bands takes less than three seconds, where each band image typically use an exposure time of approximately 130 ms. Capturing only one band for grey-scale images thus takes a minimal amount of time. The mechanical part of selecting and inspecting the samples might take a time amount in order of one second. In the mechanical part of the inspection it is important that the samples are placed appropriately for image capturing. The Specim camera takes a couple of seconds for capturing one image due to the moving slider used to produce an image from the line-scan device. However, the SuperK system in the present set-up takes a couple of minutes for capturing one image, though it will likely be faster in the future.

For the data processing part, the preparation of the data consists of image segmentation using a threshold and morphological operations, then calculating the mean of the segmented region. Training the prediction algorithm can take a long time, but when the model is done then evaluating a sample is rather fast. Predicting a sample is done using one or two simple arithmetic operations such as a vector multiplication. All of these processing operations are typically performed in a fraction of a second, depending on the implementation.

This makes it possible to inspect a sample in about five seconds time, which is

sufficient for this type of industrial application.

Temperature is affecting the spectral response of the NIR range [12]. The temperature in a food and feed factory can be higher than normal room temperature used in this experimental work. Therefore, the sample temperature should be investigated and calibrated for when implementing the method in the industry. And furthermore, heating of the camera sensor demands continuous calibration of the sensor since the dark current is very sensitive to increased temperature [11, 14].

Practically it is needed to use a shield for minimising surrounding light and producing a controlled light source. In the food and feed industry a camera and device housing of dust and moisture resistant stainless steel is recommended [1]. The system will be subject to dust and grease which could reduce the image quality. To minimise this, the camera can be put behind a thin transparent piece of glass or plastic, but that also act as a lens so it needs to be of high quality. The transparent cover could be covered with a surface layer that can minimise dust content and reflections [111].

Chapter 5

Conclusions

This chapter summarises the scientific publications of this thesis, in Part II, together with the background and discussion of the research in Part I. The chapter is concluded by a section with closing remarks on the work.

5.1 Discussion

The first objective of the thesis was to investigate the possibility of on-line quality assurance of pellet size in relation to the extrusion of fish feed products. The aquaculture feed production industry faces the challenge of controlling the size during production of the pellets, while the pellet size is crucial for the growth rate of fish.

The pellet size was analysed using images of a large amount of piled pellets with image analysis based on morphological opening operation. The opening result was analysed using a modified derivative giving the size distribution curve of all pellets in the images at every time point during the production. The opening operation is well-used for calculating particle size distribution and is usually done on segmented objects, but here this method was applied on images of disordered and overlapping pellets. It was shown that both the diameter and length of the pellets were increasing with time during pellet production so

therefore a general size measure based on the visible pellet area was feasible with good results.

The second objective was to investigate the possibility of at-line quality assurance of astaxanthin coating in the extrusion of fish feed products. Fish feed pellets are coated with fish oil with added astaxanthin, which is usually the most expensive ingredient in the feed. Because of the high cost, there is a need to optimising quantities of astaxanthin used in the fish feed production.

It was investigated if it is possible to predict the synthetic astaxanthin coating concentration level by spectral imaging. Moreover, it was also investigated if it is possible not only to predict based on pellets lying on their side, but also using disordered pellets in a pile as they appear in the production. In the industry many different pellet recipes are used, and any one recipe may have varying raw materials. Therefore it is of interest to assess a robust model for astaxanthin concentration prediction which is not affected by the underlying compound. For this purpose, four different pellet recipes were used, as well as different imaging devices. The results turned out to give good results for quality control of astaxanthin coating concentration by spectral imaging.

The third objective was to investigate the possibility of determining the astaxanthin type detected in salmonid fish meat. The colour of salmonid fish is the most important quality parameter for customers. Using pellets coated with astaxanthin, the astaxanthin colouration of the fish was assessed.

The goal was to be able to differentiate between fish meat from fish having been fed with natural and synthetic astaxanthin. Furthermore, it was tested whether the best predictions come from multi-spectral image analysis of the steak biopsy or the fillet of the fish. Multi-spectral images were analysed using percentiles and sparse statistics in order to discriminate between fish meat from fish fed with synthetic astaxanthin, natural astaxanthin and no astaxanthin. Also, the fish meat was analysed using a tricolour detector, which was compared with using an ordinary SalmoFan sensor panel. The results show that the control group, which was not fed with astaxanthin, is quite easy to separate from the two astaxanthin groups, while it is more difficult to separate the natural and synthetic groups.

As stated in the fourth objective, recent statistical methods have been used to achieve the other objectives for this thesis. The recent statistical methods have been compared to traditional methods. Since it is easy today to gather vast amounts of data it is important to analyse and select the properties of interest. When using data with many variables it is of interest to select the ones which are relevant to the problem at hand. Also of importance is that the statistical model used is comprehensible. Interpretability is in many cases a factor of interest.

The recent sparse statistical methods used herein calculate models that are easy to interpret.

Spectral imaging offers both spatial and spectral information in combination which makes it a good potential technique for surface inspection. Spectroscopy is a well-used method for spectral information but it only measures a spot at a time and hence does not provide spatial information in the same manner as spectral imaging. With this said, spectral imaging needs to be trained on known regions. Hence we need reference values which are often region based and not pixel-based. Therefore many in the spectral imaging field are using a region average from the images as data, which is not exactly the same as spectroscopy but has many similarities. One of the advantages is that one can cover an entire region and not only a point, while an average is not always representative of a region with large variation. However, the pixels in a region can be used as samples which preserve the region variation but sometimes put some demand on the computations using vast number of samples. The pixels of spectral images can also be analysed unsupervised in order to find variation or correlation in the data that could be of potential interest and be interpreted in a useful manner.

The objective of this thesis was not to assess detailed spatial information. However, by using spectral imaging the reflection spectra from many samples can be captured rapidly giving a more robust result. For future work on spectral imaging of fish meat the spatial details are of interest for detecting different regions and content mixes of e.g. fat, collagen, muscle, and overall colour. A suitable method for this is e.g. spectral unmixing.

5.2 Conclusions

This thesis consists of work combining techniques from image analysis, spectral imaging, chemometrics, statistical process control, and multi-variate statistics with applications in the aquaculture industry. The methods and results are presented through publications in both the field of image analysis and the field of fish.

The results of the work demonstrate a high potential of image analysis and spectral imaging for assessing the product quality of fish feed pellets, astaxanthin and fish meat. It is shown how image analysis can be used to inspect the pellet size with good correlation to the measured pellet size. Furthermore, the experimental work show how spectral imaging can be used to inspect both the concentration and type of astaxanthin coating of pellets, which is important both from the industry's perspective and so that the fish get good nutrition.

Spectral imaging has likewise shown good results for detecting the astaxanthin type in fish meat, which is important on the organic fish market.

Spectral imaging has a great potential for non-contact surface quality inspection of biological materials. This technology and method can be a useful tool for optimising the industrial process, e.g. the utilisation of the expensive astaxanthin. An automatic vision system measures without physical contact which is of paramount importance in the food and feed industry and makes it suitable for nondestructive on-line measurement.

The development of automatic quality inspection methods by machine vision can improve the industry's position in the competition for high quality products and efficient processes.

Part II

Contributions

Appendix A

Image Analysis of Pellet Size for a Control System in Industrial Feed Production

Martin Georg Ljungqvist, Michael Engelbrecht Nielsen,

Bjarne Kjær Ersbøll, Stina Frosch

Published in PLoS ONE, Public Library of Science, 2011 [91].

Abstract

When producing aquaculture fish feed pellets, the size of the output product is of immense importance. As the production method cannot produce pellets of constant and uniform size using constant machine settings, there is a demand for size control. Fish fed with feed pellets of improper size are prone to not grow as expected, which is undesired by the aquaculture industry. In this paper an image analysis method is proposed for automatic size-monitoring of pellets. This is called granulometry and the method used here is based on the mathematical morphological opening operation. In the proposed method, no image object segmentation is needed. The results show that it is possible to extract a general size distribution from an image of piled disordered pellets representing both length and diameter of the pellets in combination as an area.

A.1 Introduction

In the aquaculture industry it is of outmost importance that the fish get feed of proper size. The feed is usually in pellet form, where the pellets contain the nutrients that the fish need to grow and stay healthy. The size of the pellets is adapted to the size of the fish so that the fish can grow as expected. It has been shown that growth rate of fish is closely related to the pellet size of feed [8, 136, 145]. Therefore, when producing feed pellets for aquaculture there is a need to control the size of the output product, and this is a challenging task.

An extruder machine is commonly used for fish feed production. The feed material is extruded through a die plate with holes of a certain diameter which determines the diameter of the pellets. On the other side of the disk is a set of rotating knives that cut the material into shorter cylinder-shaped pellets. The length of the pellets is affected both by the velocity of the knives and the pressure inside the machine.

When the extruder machine has been running for some time, the holes in the die plate get clogged with raw material. The time-frame for this to happen depends on the composition of the raw material and the pellet size produced. This clogging of holes restrains further material – either completely or partly – from flowing through the holes and therefore affects the output of the machine.

Additionally, the pressure inside the extruder rises during operation, inducing a rise in the velocity of the feed as it passes through the holes, resulting in a drift of the pellet size. Moreover, the temperature of the machine increases, and

this might affect its physical properties, both velocity and pressure. Changes in pressure and temperature result in the problem that the pellet size changes over time during a batch production.

Today, size monitoring is done by manual inspection in order to adjust the settings or restart the machine. This is both labour-demanding and relies on experienced assessors. An automatic vision system for on-line quality control would be of great benefit to the industry, both for process control and product optimisation. If automatic size measurement could indicate when the pellet size is outside the defined range, this information could be used to adjust machine settings such as the knife speed, screw speed, filling rate or other means of controlling the pellet expansion process, thereby controlling the pellet size and ensuring uniformity.

Measuring the size distribution of small particles is often referred to as granulometry or sometimes as particle size distribution analysis [97]. The proposed method is based on image analysis using mathematical morphology and in particular using the so-called morphological openings used for size distribution analysis. This technique was proposed by Matheron (1975) [96], a vast amount of work on granulometry on binary images was also done by Serra (1982) [122] and the technique has been further developed for grey-scale images [141, 142].

Morphological openings are widely used for granulometry in image analysis and have been used for many applications [6, 35, 79, 101, 144]. These all use an image segmentation method before performing the morphological opening.

Another approach to granulometry is the use of frequency transform analysis, as can be seen in Zadorożny et al. (2002) [157], where a specific segmentation method is not needed. The same paper also used the technique of scale-space [81, 82, 83], which can likewise be seen in Clemmensen et al. (2010) [30]. A similar approach without segmentation can be seen in Jägersand (1995) [67].

Measuring fish feed pellet size by image analysis has previously been done by Parsonage (2001), who used a stepwise grey-scale threshold to segment the pellets in underwater images [112]. Moreover it has also been done in the work by Foster et al. (1995) using a grey-scale threshold and classification based on binary shape and size of image objects [49]. The threshold method, with corresponding binary shape features, is limited since it only works on single pellets and is therefore not suitable for the problem presented in this paper; measuring piled, disordered pellets.

Besides these, the area of determining the size of fish feed pellets has, to the authors' knowledge, not been further investigated. Image analysis has not previously been used in production quality control of feed pellets.

The aim of the present work is to develop an on-line control system based on image analysis for real-time inspection of pellet size during industrial production. This will be done using the well-known method of morphological opening, which can be interpreted as a mathematical analogy to sieving. By calibrating the method to a threshold of what is and what is not an acceptable size, the industry can use the method to get automatic and instant feedback about pellet size in order to adjust the machine settings during production.

Moreover, since the method is to be on-line in the production plant where the pellets are still moist, it should be investigated how the size measurements of moist and dry pellets correlate. It is of interest to investigate if it is possible to predict the size of pellets in dry condition from measurements made of moist pellets.

A.2 Materials and Methods

The shape of the pellets is close to cylindrical with a length and a diameter, where the diameter is the product size referred to in the industry. It is assumed that both length and diameter change during the production time.

Initially, the size increase of pellets during production was investigated both by image analysis and by manual measurement. The image analysis was done using grey-scale images of 24 pellets of a certain size category and measuring the length and width of pellets in pixels using a threshold and binary operation for the major and minor axes of the pellets. The size of pellets at production start was compared to the size at production stop of the same batch. Manual measurement was done on 51 pellets from each time sample of batch C and D using a Mahr 16EX calliper (Mahr GmbH Esslingen) with a resolution of 0.01 mm and error limit of 0.02 mm.

A.2.1 Image Acquisition

All images were taken using a Point Grey Scorpion SCOR-20SOM grey-scale camera, with the pellets placed in a plastic petri dish (diameter 9 cm) inside an integrated sphere (Ulbricht sphere) with uniform diffuse lighting from light-emitting diodes placed around the sphere. This kept the amount of shadow to a minimum, and the upper part of the pellet pile were almost without shadows. The combined camera and light set-up used was the VideometerLab device (Videometer A/S, Hørsholm, Denmark). The image dimension used was 800

× 600 pixels. In this situation one pixel equals approximately 0.072 × 0.072 millimetres, hence the image represents approximately a 57.6 × 43.2 mm area.

A.2.2 Sample Preparation

Pellets were collected from a production batch at specific time intervals and a total of four batches were analysed, see Table A.1. Images of dry pellets were taken from all four batches. Additionally, for batches C and D images were captured directly after the pellets were extruded, meaning that the pellets had a high level of moisture, whereas the finished product is dry.

Table A.1: **The batches analysed**

	Size (mm)	Sampling time (min)	Observations	Repetitions	Total time (min)
Batch A	1.1	30	10	5	270
Batch B	1.1	60	6	1	300
Batch C	1.1	5	11	1	50
Batch D	3.0	1-5	27	1	45

Product size (millimetres), time between sampling (minutes), number of observations, number of repetitions for each observation and total batch time (minutes).

Two different pellet product sizes were used to investigate whether there would be any difference related to product size and the result of the proposed method. The product size refers to the nominal diameter, which was 1.1 mm and 3.0 mm, respectively, for the analysed pellet batches.

A.2.3 Image Analysis

By analysing images of pellets, with sizes ranging from normal to large, a model for distinguishing the relative size of pellets in an image can be made.

To start with, the images were adjusted for contrast before being analysed using contrast-limited adaptive histogram equalization (CLAHE).

The granulometry method used was a morphological opening operation. Since we did not know the orientation of the piled pellets in an image, this operation was performed so that it was independent of rotation.

The morphological opening operation performs an erosion operation followed by a dilation operation using a so-called structuring element. A structuring element is a mathematical binary shape; here we used the shape of a disk, see Figures A.1 and A.2. If the structuring element can fit inside an area of the image then the whole structural element will appear in the result of the transformation.

The parts of the original image that the operator does not fit inside will not be a part of the result. This means, that if the objects in the image are smaller than the element size, then the result will be of low intensity. This is achieved because the erosion operation leaves a disk-shaped area consisting of the lowest pixel value found inside the disk-element region of the image for each viable position of the element inside the image. Dilation does the same thing but uses the maximum value for each region.

The erosion, dilation and opening for an image A and a structuring element B are defined as:

$$A \ominus B = \bigcap_{b \in B} A_{-b} \tag{A.1}$$

$$A \oplus B = \bigcup_{b \in B} A_b \tag{A.2}$$

$$A \circ B = (A \ominus B) \oplus B. \tag{A.3}$$

The opening operation can be interpreted as finding objects of a certain size and, to some extent, of a certain shape. See Figures A.3 – A.6 for examples of resulting images of this method.

For comparison, different structuring elements were tested: disk, octagon, ball and diamond. All showed similar performance (results not shown), and therefore the disk operator was chosen, since it constitutes a good approximation of general pellet size with both increasing length and width.

By increasing the radius of the disk and summing the image intensity for each radius, an opening intensity curve is achieved. The advantage of this method is that it can be used on an image filled with pellets; segmentation is not necessary. The method will not give a size distribution based on each single pellet. Rather is it an overall assessment on a pile of pellets which makes a size index measure.

The opening intensity corresponding to each disk element size used is similar to what one would get using the scale-space method and represents a measure of the size information in the image. When a disk size cannot fit into most of the pellets

Figure A.1: **Structuring element.** Disk of radius 1-11 pixels created using the Euclidean distance.

Figure A.2: **Structuring element.** Disk of radius 1-11 pixels created using a decomposition method with a neighbourhood of 4 pixels.

in an image, the intensity output from the opening operation will be low. When the pellet size increases the location of the major intensity drop in the intensity curve changes. The opening intensity curve is also known as the granulometric curve. In order to analyse the changes in the decline of the intensity curve, we calculate the derivative of the opening intensity by calculating the differences between each opening operation.

Successive sample points over time have different opening intensity curves and this reflects the change in size distribution. Various methods for analysing the opening intensity curves have been tested and are described below.

Initially a structuring element disk with no approximation was used. The disk was created using the Euclidean distance, see Figure A.1. Further on, a disk with some approximation was used to reduce calculation time, see Figure A.2. The disk with approximation is less than a perfect disk but instead it is decomposable [2], which vastly increases the computational speed. The decomposition technique of Jones et al. (1996) was used [72].

A.2.4 Pattern Spectrum

In granulometry, the derivative is often replaced by the so-called Pattern Spectrum (PS) [95]. The pattern spectrum is defined as the difference between the intensity values of successive morphological opening operations divided by the sum of all pixel values in the original image. The pattern spectrum is equivalent to the negative derivative of the opening intensity normalised by the total pixel sum. The pattern spectrum is also known as Pecstrum and is interpreted as the estimated particle size distribution function.

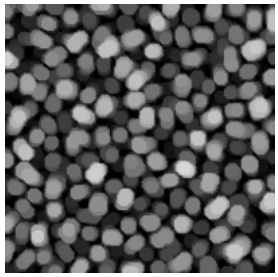

Figure A.3: **Image opening.** Morphological opening using a disk with radius of 5 pixels on start-up sample pellets.

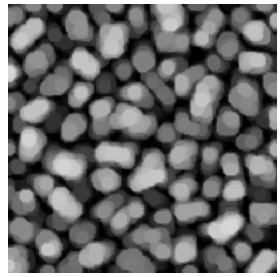

Figure A.4: **Image opening.** Morphological opening using a disk with radius of 5 pixels on stopping sample pellets.

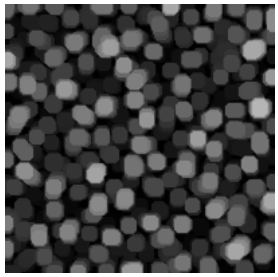

Figure A.5: **Image opening.** Morphological opening using a disk with radius of 6 pixels on start-up sample pellets.

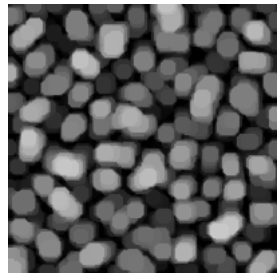

Figure A.6: **Image opening.** Morphological opening using a disk with radius of 6 pixels on stopping sample pellets.

The discrete pattern spectrum of image A using structuring element B is defined as:

$$P(n, B) = \frac{M[A \circ nB] - M[A \circ (n+1)B]}{M[A]} \tag{A.4}$$

where M represents the area measured in the intermediate operations, and nB is the structuring element with the size increased n times.

When analysing pellets of increasing size, we can use that the maxima in the pattern spectrum changes location. For analysing the change in size over time, we use the opening intensity at the position of the pattern spectrum maximum as a size index, here called APM.

A.2.5 Size Index

Another way of analysing the morphological opening intensity curves is to take the average of each of these curves to reveal the progression. Typically this would result in an increasing sequence.

In statistical process control, the median is often used instead of the mean to get more robust results. By taking the median value of each opening intensity curve, this would give a good measure of the size changes. This measure represents looking in the vertical direction at the middle of the successive intensity curves. Moreover, the Interquartile Range (IQR) can be used for analysing variation of the opening results. The IQR is constituted as the difference between the first and third quartiles of the curve [100].

An overview of the proposed size index method can be seen in Figure A.7.

All image analyses and statistics were carried out using Matlab 7.9 (The Mathworks Inc., Natick, MA, USA).

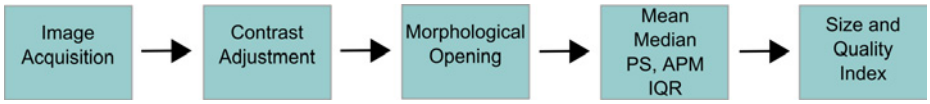

Figure A.7: **Method overview.** Block diagram of the method used. The size index is calculated using one of the methods mean, median or APM. The pattern spectrum is used as a size distribution estimate. IQR is calculated to get a measurement of the spread of the size distribution and as another quality measure.

A.3 Results

In the initial image analysis of single pellets, the size of 24 pellets at production start was compared to the size of 24 pellets at production stop, see Figures A.8 and A.9. The comparison using image analysis shows an increase in both length and width (diameter). Both length and width (diameter) were significantly different at a 0.1% significance level, indicating that the area of a pellet in an image increases with time.

A.3.1 Calliper Measurement

Manual measurements was done on the pellet width (diameter) and length using a calliper. The results show a clear increase in both the diameter and the area (length × width) of the pellets over time, see Table A.2. The mean values of the calliper measurements at start and stop of both batch C and D in dry condition are significantly different at a 0.1% significance level. The statistical power for these calliper measurements of the diameter is set to 80%, which results in an estimated accuracy of 0.09 mm for batch C (1.1 mm) and 0.055 mm for batch D (3.0 mm) at a 5% significance level. This means, that we trust the calliper measurements as a base for comparison of the image analysis results.

Table A.2: **Image analysis and calliper measurements**

	Production diam. (mm)	Calliper diam. (mm)	Opening radius (pixels)	Opening diam. (mm)
		Start	Start	Start
Batch A	1.1	-	7	1.008
Batch B	1.1	-	4	0.576
Batch C	1.1	1.236	7	1.008
Batch D	3.0	3.094	21	3.024
		Stop	Stop	Stop
Batch A	1.1	-	9	1.296
Batch B	1.1	-	6	0.864
Batch C	1.1	1.805	8	1.152
Batch D	3.0	3.610	25	3.600

Pellet size results in pixels and millimetres for start and stop of the batch production. Production diameter (mm) is the target size of the produced pellets. Calliper diameter (mm) is the manually measured size of 51 pellets. Morphological opening radius (pixels) is the radius with the highest density in the pattern spectrum. Opening diameter (mm) is the opening radius converted from pixels to diameter in millimetres. Calliper measurements were only done on batch C and D. Pellets in dry condition.

A.3.2 Opening Intensity Curve

The morphological openings were applied to all batches in order to calculate the size index. Comparing the morphological opening curves for start and stop samples reflects a change in the pellet size distribution, see Figure A.10 for batch A. The derivative of the opening intensity of batch A can be seen in Figure A.11.

The corresponding images for start and stop samples of batch A can be seen in Figures A.12 and A.13.

The successive morphological opening intensity curves are an indication of pellet size changes in an image and the result for batch A can be seen in Figure A.14. A close-up on the morphological opening intensity for batch A showing the size changes over time can be seen in Figure A.15. Each derivative extremum in the intensity derivative indicates a change in the opening intensity, the result for batch A can be seen in Figure A.16.

The size index calculated by the opening intensity mean, as well as the size index calculated by the opening intensity median, both indicate the trend of the size change in all tests, see Figure A.17 for batch D.

The opening intensity mean on dry pellets for batches C and D was compared to the calliper measurements' mean area value. Since the opening operation measures both diameter and length of the pellets in an image, both are included as area in this correlation. The correlation of the two curves of batch C is 0.52, see Figure A.18, and for Batch D the correlation is also 0.52. Moreover it can be seen that the trend-lines of the image analysis result correlate positively with the trend-lines of the calliper measurements' mean value. For both batches C and D, the trend-lines of the image analysis and calliper measurements are increasing. An overview of the comparison between image analysis and calliper measurements can be seen in Table A.2. For full results on correlation between image analysis and calliper measurements, see Table A.3.

Comparing the size index with the calliper diameter measurements gives that the Root Mean Square Error (RMSE), i.e. the deviation between the two methods, is 0.07 mm for batch C with production size 1.1 mm, and 0.06 mm for batch D with production size 3.0 mm, see Table A.4. This means that the image analysis method shows good estimated accuracy.

Both the mean and median of the morphological opening intensity show similar patterns, the correlation between the two is at least 0.92 for the batches analysed, see Table A.5.

The IQR of the opening intensity is a variation measure and shows that the pellet size variation increases over time in a similar manner as the size, see Figure A.19.

Table A.3: **Image analysis and calliper measurements correlation**

	Full Disk	Decomposable Disk	Trend-line
Batch C			
Mean	0.5185	0.5199	1.0000
Median	0.5597	0.5610	1.0000
APM	0.5118	0.5102	1.0000
IQR	0.3886	0.3888	1.0000
Batch D			
Mean	0.5172	0.5129	1.0000
Median	0.4381	0.4369	1.0000
APM	0.4821	0.4757	1.0000
IQR	0.4428	0.4410	1.0000

Size change correlation between image analysis (size index and spread) and calliper area measurements (length × diameter). Correlation for different disk approximation types for batches C and D are shown. The size index is calculated using morphological openings and then using the mean, median or the opening intensity at the position of the pattern spectrum maximum (APM). The Interquartile Range (IQR) is used as a variation measurement. Pellets in dry condition.

Table A.4: **Image analysis method compared to calliper measurements**

	SD (mm)	RMSE (mm)
Batch C (1.1 mm)		
Mean	0.0547	0.0749
Calliper	0.0528	-
Batch D (3.0 mm)		
Mean	0.1236	0.0590
Calliper	0.1390	-

The deviation between the size index using mean of the morphological opening intensity and the calliper diameter measurements. SD is the Standard Deviation and RMSE is the Root Mean Square Error. The size index was normalised using the mean of the calliper measurements in order to get a scale with millimetres. A disk without approximation has been used for the opening operation. Pellets in dry condition.

Table A.5: **Image analysis method correlation**

	Moist Pellets	Dry Pellets
Batch A		
Median	-	0.9907
APM	-	0.9901
Batch B		
Median	-	0.9942
APM	-	0.9972
Batch C		
Median	0.9253	0.9494
APM	0.9864	0.9952
Batch D		
Median	0.9703	0.9493
APM	0.9743	0.9658

The correlation of various ways to calculate the size index. The correlation coefficient is here calculated between the mean of the morphological opening intensity and the median or APM of the same intensity. A disk without approximation was used.

A.3.3 Pattern Spectrum

The pattern spectrum shows a good estimation of the size distribution. The pattern spectrum size distribution is similar to the one obtained with the calliper measurements, see Figure A.20 and compare with the pattern spectrum in Figure A.21. Analysing the values of the pattern spectrum to the right of the maximum value results in a good size change estimation similar to taking the mean or median of the morphological opening intensity curve. Also the opening intensity at the pattern spectrum maximum (APM) shows similar results, see Table A.2. The trend-lines of APM and calliper measurements are both increasing.

A.3.4 Dry and Moist Condition

Batches C and D were analysed by the proposed method both in moist and dry conditions. The results obtained were not completely similar but the trends where almost identical, see Figure A.22. The median of the opening operation intensity curves for moist and dry condition correlate at 0.96 for both batch C

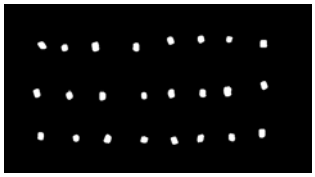

Figure A.8: **Pellets.** Binary image of pellets at production start.

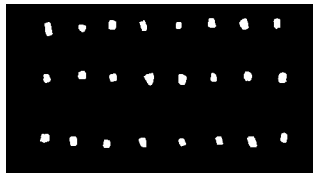

Figure A.9: **Pellets.** Binary image of pellets at production stop.

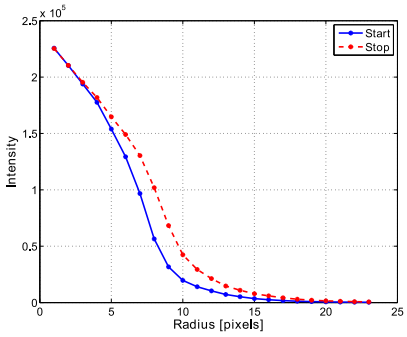

Figure A.10: **Opening intensity.** Morphological opening intensity for the start-up sample 1 (blue) and the stopping sample 10 (red) in Batch A.

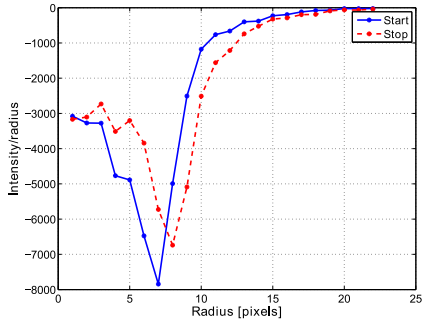

Figure A.11: **Opening derivative.** The first derivative of the start sample 1 (blue) and stop sample 10 (red) opening intensity in Figure A.10.

and batch D. It seems that the moist condition renders slightly higher size results than the dry condition for both batch C and batch D, however the difference is not large. This means that measurements of the moist pellets can be related to the dry pellets and the method can therefore be used for on-line quality control.

A.3.5 Summing Up

It is concluded that the image opening intensity mean, intensity median and APM all perform well as a size index measure on a dish filled with pellets. Intensity median had the highest correlation with calliper measurements for batch C, and APM had the highest correlation for batch D, see Table A.3. While APM performs similarly to intensity mean and intensity median, it needs slightly more computation without gaining any information in comparison. We also see that measurements on moist pellets have a high correlation with measurements on dry pellets and that we can therefore predict the dry pellet size from measure-

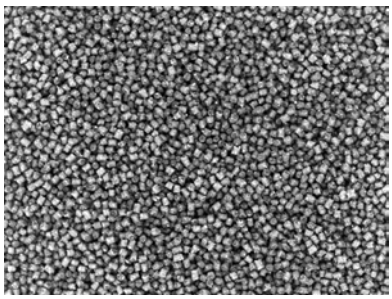

Figure A.12: **Pellets.** Image of pellets at production start. Batch A.

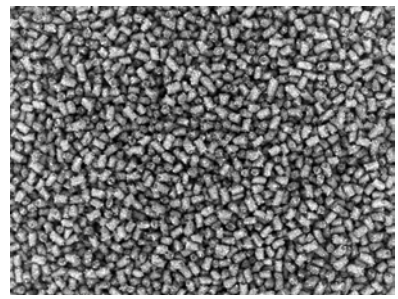

Figure A.13: **Pellets.** Image of pellets at production stop. Batch A.

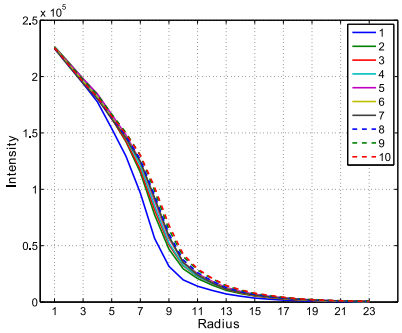

Figure A.14: **Opening intensity.** Morphological opening intensity for all time samples (1-10) in Batch A. This is the result of the image opening operation.

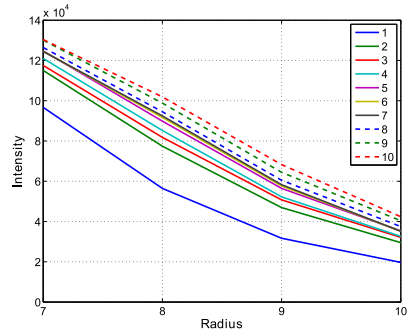

Figure A.15: **Opening intensity.** Close-up of Figure A.14 showing the changes in opening intensity for all time samples. Morphological opening intensity for all time samples (1-10) in Batch A.

ments on the moist pellets.

No particular difference could be seen in the behaviour of the opening measurements between product size 1.1 mm (batches A, B, C) and 3.0 mm (batch D). This implies, that the proposed method works for different production size categories.

Furthermore, based on the results obtained, it is concluded that the contrast level of the images affects the robustness of the size measure. The contrast level of the images is thus an important parameter for this method to perform well. For robust results of the size measurement, the image contrast should be as high

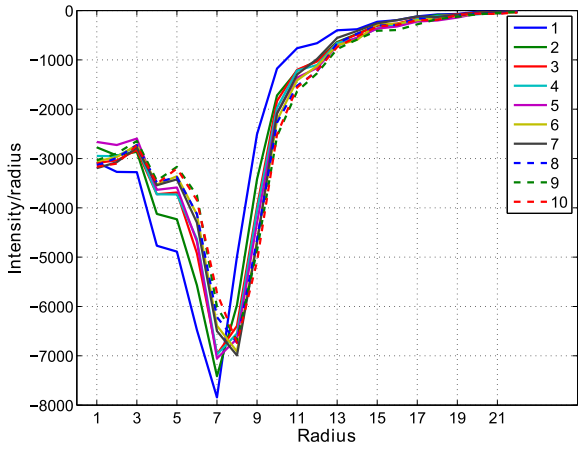

Figure A.16: **Opening derivative.** The first derivative of the opening intensity for all time samples (1-10) in Batch A.

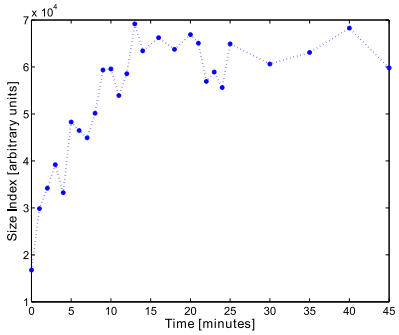

Figure A.17: **Size index.** The size index using the median of morphological opening intensity on pellets from batch D.

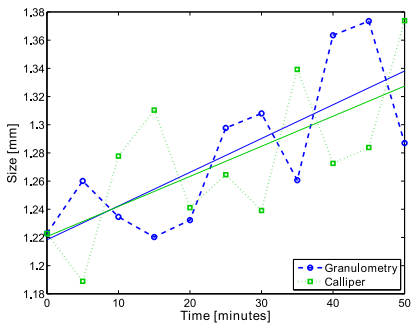

Figure A.18: **Size index comparison.** The median of morphological opening intensity of dry pellets (blue) compared to the calliper diameter measurements of dry pellets (green), and their trend-lines, batch C. Size index values normalised for comparison purpose.

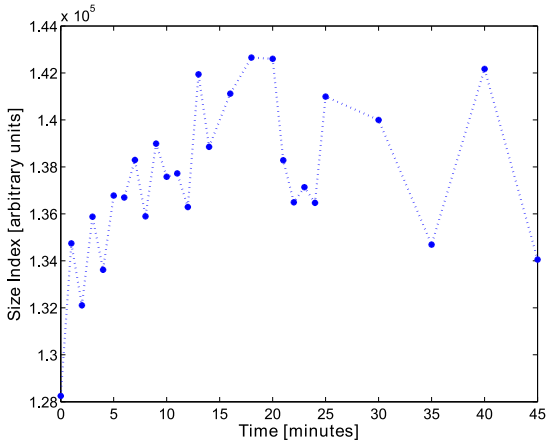

Figure A.19: **Size variation.** The size variation using the Interquartile Range (IQR) on batch D.

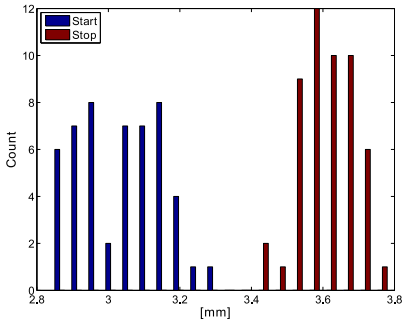

Figure A.20: **Calliper measurement.** The manual, calliper-measured diameter of the start (blue) and stop samples (red) of 51 pellets from batch D. Pellets in dry condition.

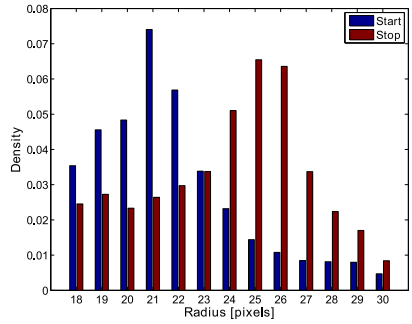

Figure A.21: **Pattern spectrum.** The pattern spectrum showing the estimated area size distribution of start (blue) and stop (red) samples of batch D. Using image analysis with morphological opening. An image area of pellets of approximately 57.6 × 43.2 mm was used (800 × 600 pixels).

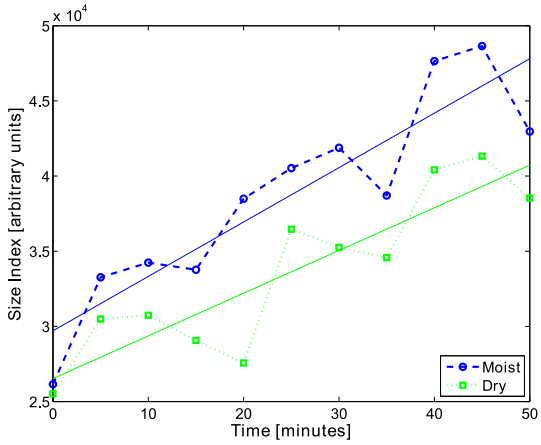

Figure A.22: **Size index of dry and moist.** The median of the morphological opening intensity for batch C in moist (blue) and dry condition (green), and their trend-lines.

as possible.

A.4 Discussion

Previous work in this field has used segmentation before the morphological opening step, which could be a source of error and it also consumes computation time. In the present study it is demonstrated that a general size indication can be found using the morphological opening method on piled pellets without the segmentation procedure. Moreover it is shown that, of all the methods tested, the mean and median is the best method for analysing the opening intensity curve in order to estimate the pellet size progression.

When the pellets are piled, there is an angular distribution of how many are lying down, standing up, and at angles in between. It is therefore required that the model works even if the pellets are rotated. The measurement using the proposed method is of a projected area of arbitrarily rotated pellets. As the product size of the pellets changes, the proportions will change accordingly. This affects the distribution of lying and standing pellets and how they cast shadows on each other. If the diameter and/or the length have increased, the pellet volume will increase and thus the projected area in the image will increase. Therefore we measure the general size change on pellets randomly distributed in the image space.

The results clearly show that it is possible to extract a general size index from an image of piled pellets. The proposed method is suitable for on-line measurement of pellet size changes and will be of high importance to the pellet producing industry. This method is expected to work generally for granulometry situations and could be used for further applications.

The resulting size index can be used to calibrate a production batch for start-up size and a threshold size. The size measurement information can be used to adjust production parameters, as well as to make a quality characteristic control chart for size monitoring in the production. The size index seems to have a logarithmic trend for all the batches analysed. Further on it will be natural to use statistical quality control methods such as a moving average to analyse the size index in the production.

It was shown that the results obtained for moist and dry pellets are highly correlated. This result makes it possible to use the proposed method on moist pellets in the production and still be able to give a measurement of the size of the pellets in dry condition. The decrease in pellet size indication between moist and dry condition is interpreted such that the pellet size is smaller when water has evaporated from the pellet.

The difference in robustness of the results could be related to the total production time of the sampled batch, where samples from a batch with long production time would be more robust since short fluctuations in size would not be as influential here as in batches C and D with shorter time between samples.

The results of using an approximated (and decomposable) disk with a non-approximated disk are similar, see Table A.3, however the pattern spectrum shows more artefacts when using an approximated disk. The approximation's deviation from the theoretical disk area introduces a slight irregularity in the opening intensity curve and is hence clearly visible in its derivative with re-occurring spikes for certain radius values. However, these artefacts are at equal positions for all measurements and are assumed not to influence the result of the measuring method. A good indication of this can be seen in the disk comparison in Table A.3, where it can be seen that the differences in correlation with the calliper measurements are very small between using a non-approximated disk and an approximated disk. These irregularities can be avoided, though, if non-integer radius values are used, i.e. the radii should be estimated from actual area of the decomposable disks.

The reason for using an approximated disk is to reduce computation time. The computational time using a non-approximated disk is about 10-times longer for batches of size 1.1 mm (A, B, C), and about 30-times longer for the 3.0 mm batch (D). The computational time for a morphological opening is dependent on

the image size and the size of the structuring element. This means that the time penalty is worse when detecting large objects while using a non-approximated disk. Since the difference in the achieved size index between using an approximated disk and a non-approximated disk is small, the proposed method using an approximated disk shows acceptable calculation times for on-line measurement in the industry.

A more smooth behaviour of an opening intensity derivative can be achieved by performing a spline polynomial estimation of the intensity curve and then deriving this analytically. Polynomial estimation of morphological opening results can e.g. be seen in Morales-Hernández et al. (2010) [101].

The proposed method will not be affected if, due to moisture, pellets aggregate such that they could be interpreted as one large pellet. Such a cluster will not be interpreted as a large pellet, since the structure of the constituent pellets will still be visible.

Further investigation on how the following factors impact the result should be performed: lighting, camera, position of camera and pellets as well as pellet type. The lighting and hence the shadows is a topic believed to impact the result and should be investigated in more detail. Further investigations could e.g. be done using the scale-space method, frequency transforms or image profiles.

Acknowledgments

The work presented has received funding from BioMar A/S and the EU under the Seventh Framework Programme FP7/2007-2013 under grant agreement number 214505.10.

Appendix B

Multi-spectral Image Analysis for Astaxanthin Coating Classification

Martin Georg Ljungqvist, Bjarne Kjær Ersbøll,

Michael Engelbrecht Nielsen, Stina Frosch

Abridged version presented and published in the proceedings of the Scandinavian Workshop on Imaging Food Quality (SWIFQ), at the Scandinavian Conference on Image Analysis (SCIA), Ystad, Sweden, 2011 [86]. Long version published in Journal of Imaging Science and Technology (JIST), 2012 [87].

Abstract

Industrial quality inspection using image analysis on astaxanthin coating in aquaculture feed pellets is of great importance for automatic production control. The pellets were divided into two groups, one with pellets coated using synthetic astaxanthin in fish oil, and the other with pellets coated only with fish oil. In this study multi-spectral image analysis of pellets captured reflection in 20 wavelengths (385–1050 nm). Linear Discriminant Analysis (LDA), Principal Component Analysis (PCA), Support Vector Machine (SVM) were used as statistical analysis. The features extracted from the multi-spectral images was pixel spectral values as well as using summary statistics such as the mean or median value of each pellet. Classification using LDA on pellet mean or median values showed overall good results. Multi-spectral imaging is a promising technique for non-invasive on-line quality food and feed products with optimal use of pigment and minimum amount of waste.

B.1 Introduction

Industrial quality inspection using image analysis is an area undergoing extensive development. Pigment inclusion in aquaculture feed pellets is an area of great interest for automatic visual analysis for statistical production control and optimisation.

Astaxanthin is a naturally occurring carotenoide with high antioxidant activity essential for reproduction, growth and survival, and important for the development of colour in salmonide fish [128]. The primary use of astaxanthin within aquaculture is as a feed additive to ensure that farmed salmon and trout have similar appearance to their wild counterparts [138]; it is the pigment that makes salmonide fish red. The colour appearance of fish products is important for customers. Astaxanthin is very expensive [9] and therefore optimising quantities used in fish feed production is important.

An automatic vision system for on-line quality control of pigment inclusion will be of great benefit to the industry, both in relation to process control and process optimisation.

This paper is based in part on an earlier study by Ljungqvist et al. (2010) [88]. Besides this, to the authors' knowledge no further work has previously been done on analysing the coating of fish feed using image analysis. Multi-spectral image analysis has shown good results in previous biological applications, where

it has been of interest to detect subtle differences in colour and surface chemistry [19, 30, 31, 32, 37, 38, 56, 74, 80, 93, 110, 133, 140, 149].

The aim of this project is to investigate the possibility of distinguishing between feed pellets coated with fish oil with and without added astaxanthin using multi-spectral image analysis in order to investigate what spectral features are of interest for further analysis of astaxanthin coating.

B.2 Material and Methods

B.2.1 Material

The feed types used were EcoLife20 and AquaLife R90 (BioMar A/S, Brande, Denmark), both with the radius of 4.5 mm. Each of the two types of fish feed pellets were divided into two groups. One group constitutes pellets coated with fish oil with an additional 50 ppm of a synthetic version of astaxanthin; group A (astaxanthin). The other group was the same type of pellet, coated using the same fish oil without additional astaxanthin; group B (base). The fish oil typically contains a small amount of natural astaxanthin, but this is assumed to be less than 1 ppm and should therefore not affect the results. The distribution of the surface coating was unknown and some amount of variation was likely to have occurred.

The pellets of type EcoLife20 were all produced on the same day, while the pellets of the two groups of AquaLife R90 where produced on different days. This means that the difference between group A and group B of AquaLife R90 is not only the added synthetic astaxanthin in the coating, but could also be differences in the constituent raw materials.

Two feed types were used in order to test the robustness of the astaxanthin coating prediction. A total of 2223 EcoLife20 pellets were used, and a total of 2158 AquaLife R90 pellets were used, see Table B.1.

B.2.2 Imaging Equipment

The equipment used was a camera and lighting system called VideometerLab (Videometer A/S, Hørsholm, Denmark) which supports a multi-spectral resolution of up to 20 wavelengths. These are distributed over the ultra-violet A

Table B.1: Number of analysed pellets in each group. Group A represents pellets coated with synthetic astaxanthin in fish oil, and group B is pellets coated only with fish oil.

	Size (mm)	Group A samples	Group B samples	Total samples	Production day
EcoLife20	4.5	1165	1058	2223	Same
AquaLife R90	4.5	1207	951	2158	Different

(UVA), visible (VIS) and first near infrared (NIR) region. The range is from 385 to 1050 nm, as shown in Table B.2.

This system uses a Point Grey Scorpion SCOR-20SOM grey-scale camera and the objects of interest are placed inside an integrating sphere (Ulbricht sphere) with uniform diffuse lighting from light sources placed around the rim of the sphere. All light sources are light-emitting diodes (LED) except for 1050 nm which is a diffused laser diode. The curvature of the sphere and its white matt coating ensures a uniform diffuse light so that specular effects are avoided and the amount of shadow is minimised. The device is calibrated radiometrically with a following light and exposure calibration. The system is also geometrically calibrated to ensure pixel correspondence for all spectral bands [48].

The Scorpion camera has a 12 bit analogue to digital converter (ADC), and the system used 8 bit data output from the camera. The correction for calibration gives reflectance intensity output of 32 bit precision.

The image resolution is 1280 $\times$ 960 pixels. Each file contains 20 images, one for each spectral band. This results in a multi-spectral image cube with dimensions of 1280 $\times$ 960 $\times$ 20. In this situation one pixel represents approximately 0.072 $\times$ 0.072 millimetres.

B.2.3 Spectral Equipment

In order to explore further the spectral properties of astaxanthin, a spectrometer was used. Absorption spectra of synthetic astaxanthin in a solution of fish oil along with spectra of plain fish oil were recorded in the VIS and NIR range using a NIRSystems 6500 absorption spectrometer (Foss NIRSystems Inc, USA) The absorption spectra were transformed to reflection values using the standard relation $A = -\log(R)$, where A is absorption value and R is the reflection value.

Table B.2: The wavelength of the light sources in the VideometerLab device and their spectral representation.

Band	Wavelength (nm)	Colour
1	385	Ultraviolet A
2	430	Violet
3	450	Violet, Blue
4	470	Blue
5	505	Green
6	565	Green
7	590	Yellow, Orange
8	630	Red
9	645	Red
10	660	Red
11	700	Red
12	850	NIR
13	870	NIR
14	890	NIR
15	910	NIR
16	920	NIR
17	940	NIR
18	950	NIR
19	970	NIR
20	1050	NIR

Every 2nd nanometre (nm) was recorded in the VIS and NIR range.

B.2.4 Image Analysis

Initially, the pellets were segmented from the background using an intensity threshold on the multi-spectral images, see Figures B.1 and B.2. Colour standard RGB image representations of the multi-spectral images was made only for visualisation in this paper, by multi-spectral colour-mapping using penalised least square regression described in Dissing et al. (2010) [36].

The basic pellet compound gives a spectral response which will be present in both group A and B. Each pixel is thus a combination of the reflectance of a set of constituents. This mix is assumed to be of equal amount for each pellet type except for the difference in the astaxanthin coating that we want to isolate in our classification.

The ground truth is that we know that certain pellets are coated with synthetic astaxanthin, but since the surface distribution is unknown, it is unclear how much synthetic astaxanthin each of these pixels contains. This gives us an uncertain one-to-many relationship situation.

One way to solve this uncertainty is to represent each pellet using the mean or median of all pixels in a pellet as sample values. In this manner we even out the variance of all pixels in a pellet and each pellet becomes a distinct observation.

In addition to the pellet pixel mean and median values, further summary statistical features to describe the coating distribution were extracted based on pellet pixel values: skewness, kurtosis, variance and maximum value.

B.2.4.1 Principal Component Analysis

Our multivariate data from the images were analysed using principal component analysis (PCA) for exploratory purposes. PCA is the most optimal method with respect to maximising the variance [63] and has been commonly used for dimension reduction to deal with ill-posed problems. If the relation of interest contains large variation, then PCA is a good method for analysing the data [53].

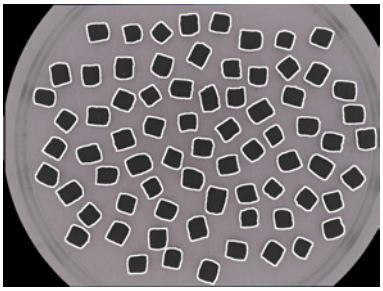

Figure B.1: EcoLife20 pellets with synthetic astaxanthin in fish oil as coating (group A) with the segmentation result overlaid (*white*). Standard RGB image using multi-spectral colour-mapping using penalised least square regression.

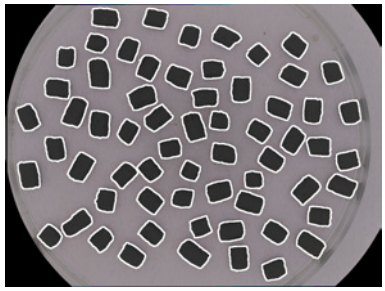

Figure B.2: EcoLife20 pellets with fish oil coating (group B) with the segmentation result overlaid (*white*). Standard RGB image representation using multi-spectral colour-mapping using penalised least square regression.

B.2.4.2 Preprocessing

The pre-processing method standard normal variate (SNV) was used in combination with PCA. SNV is performed by subtracting the mean for each sample, and normalising using the standard deviation of the sample spectrum [117]. SNV normalises each sample individually.

B.2.4.3 Discriminant Analysis

To discriminate between the two groups we want the within group variation to be small compared to the between groups variation. Wilk's Λ consists in principle of the ratio of the within group variation ($\mathbf{W}$) and the total variation ($\mathbf{T}$), i.e. the within group plus the between group variation, see Equation B.1. A value of Wilk's Λ which is close to zero indicates that the two groups are well separated.

$$\Lambda = \frac{\det(\mathbf{W})}{\det(\mathbf{T})} \,. \tag{B.1}$$

For statistical discriminant analysis methods we use linear discriminant analysis (LDA) and quadratic discriminant analysis (QDA) [63]. These are both based on the Mahalanobis distance, and assume that the observations in each group are normally distributed. LDA and QDA are based on a distance-to-the-group

mean, weighted by the variance. A training set of 70% of the samples were used here, along with a test set of 30% of the samples.

B.2.4.4 Support Vector Machine

For further discriminant analysis we used the support vector machine (SVM), which is a supervised learning technique based on the theory of optimal separating hyperplanes (OSH) [63]. While LDA and QDA are based on the distance between a sample and the group mean, SVM is based on the distance to the nearest training data points; the margin.

The basic idea with SVM is to construct an optimal separating hyperplane for the two groups by mapping the data to a higher-dimensional space. This method uses a soft margin to handle the situation of two non-linearly separable groups, meaning that a certain amount of the training samples are allowed to fall on the wrong side of the separating hyperplane which is defined by the slack amount.

SVM includes a kernel function, responsible for the transformation of the data into a higher-dimensional space. In this way the data is mapped from its original input space into the higher-dimensional feature space. Once the data has been mapped, the aim is to train the model to define a separating hyperplane in the feature space so that the data are then mostly separable by a line. One advantage of using a kernel function is that the SVM method can perform classification without ever representing the feature space explicitly, thus reducing the computational cost. The kernel is located at the point of the dot product in the SVM algorithm [63].

Popular choices for kernel functions can be seen in Equations B.2 – B.3. A d:th degree polynomial is shown in Equation B.2, and a radial basis function (RBF) can be seen in Equation B.3. The parameters of variable choice are c (constant), s (linear scaling), d (degree of the polynomial) and γ. The samples from each group are denoted $\mathbf{x}_1$ and $\mathbf{x}_2$ respectively.

It should be noted that the radial basis function has a Gaussian form, where $\gamma = 1/2\sigma^2$. The centre of the RBF is the support vector and σ will determine the area of influence it has over the data space.

For the kernel parameters, 120 values logarithmically distributed between 0 and 10 were tested for the parameters γ and d and the best result was chosen for each kernel respectively. For the polynomial kernel, the parameters c and s were both set to 1. The value of 0.5 was used as the soft margin parameter.

$$K(\mathbf{x}_1, \mathbf{x}_2) = (s\langle \mathbf{x}_1 \cdot \mathbf{x}_2 \rangle + c)^d \,. \tag{B.2}$$

$$K(\mathbf{x}_1, \mathbf{x}_2) = \exp(-\gamma \|\mathbf{x}_1 - \mathbf{x}_2\|^2) \,. \tag{B.3}$$

The SVM implementation used in this study is the SVM Light package [69].

B.3 Results and Discussion

Comparing the SNV-normalised mean spectra of the two groups of EcoLife20 shows that the largest differences between pellets coated with synthetic astaxanthin in fish oil (group A) and pellets coated only with fish oil (group B) were at 970, 950 and 565 nm (in order of magnitude), see Figure B.3. Both 970 and 950 nm are in the NIR range, while 565 nm represents the green colour which is next to yellow. Also 1050 nm shows to separate the groups. For AquaLife R90 the largest differences between the group spectra are in the visual range around 400 nm and also slightly above 600 nm.

The spectrometer results show a large deviation between synthetic astaxanthin in fish oil and plain fish oil in the range of 500 – 600 nm, see Figure B.3. This corresponds well with the results from the VideometerLab images and partly corresponds with previous studies of astaxanthin [21, 156].

The mean spectra of the two groups of both EcoLife20 and AquaLife R90 are significantly different at a 0.1% level. This is promising for classification between the two coating groups. On the other hand, Wilk's Λ of the group means of EcoLife20 pellets is 0.987, and for AquaLife R90 it is 0.826. The high values here reflect the situation of high variation within the groups and a low variation between the groups. So, even though the group means are well separated, there is a vast overlap of the two groups.

Classification tests of EcoLife20 show that LDA on the pellet means or pellet medians gave the best result with a classification correctness of about 93%. See Table B.3 for test results.

Classification tests of AquaLife R90 show that QDA on the pellet medians gave the best result with a classification correctness of 100%.

The results from LDA and QDA show for all tests that group A is misclassified into group B more often than the opposite. This could be because of the variation in the astaxanthin distribution on the pellets, in that if some pellets have less astaxanthin on the surface than others they might get misclassified.

Using LDA and QDA on the other summary statistics features (skewness, kurtosis, variance and maximum value) gave results of lower correctness for both pellet types (results not shown).

Considering the fact that the AquaLife R90 pellets of the different groups where produced on different production days, there is a chance that this fact affects the classification rate. If the two groups also contain differences in raw material batches, this could potentially increase the differences between the two groups of this pellet type and thereby improve the classification result. This gives us a confounding situation where we are not certain whether it is the synthetic astaxanthin coating that is classified, the constituent raw material differences, or a combination of the two. In future experiments this should be avoided by using the same production day for both groups. For further analysis in this area the results are likely to show variation dependent on the mixture of the pellet types in relation to the variation in feed compounds that will affect the spectral response.

Having LDA train on the mean pixel values of some of the EcoLife20 pellets, 1126 pellets from group A and 1026 pellets from group B, and then using this model on pellet pixel values for the remaining 39 and 32 pellets respectively rendered a pixel classification correctness of only 54%. The same test for AquaLife R90 shows a pixel classification correctness of 55%. This lower value in comparison to classification on the pellet mean values is interpreted as an indication of high variance of the spatial coating distribution on the pellets and/or high variance in the feed composition at the pixel level.

Using PCA before doing LDA or QDA on the pellet mean values did not improve the results, see Table B.3. This may be an indication that maximising the variance is not a well-suited method for this particular problem, which was also indicated by the high variation within groups in comparison to the variation between groups. PCA maximises the variance without specifically considering the variance between the two groups in the data. PC2 shows the largest difference between the two groups, see Figure B.4. The first five principal components explain 98% of the total variance of the pellet mean values, and still the result of the discriminant analysis on these five components rendered worse classification in comparison to using the plain 20 variables in the data.

In most of the tests LDA performed better than QDA, this is interpreted such that the problem is linear. This could also be explained by the fact that QDA uses two covariance matrices, instead of LDA:s one matrix, and in combination with data of 20 dimensions this could make QDA a bit numerically unstable. LDA also showed better results than SVM for the EcoLife20 pellets. For AquaLife R90 LDA or QDA showed better results than SVM for classification using the pellet mean or pellet median values, while the classification using PC1-5

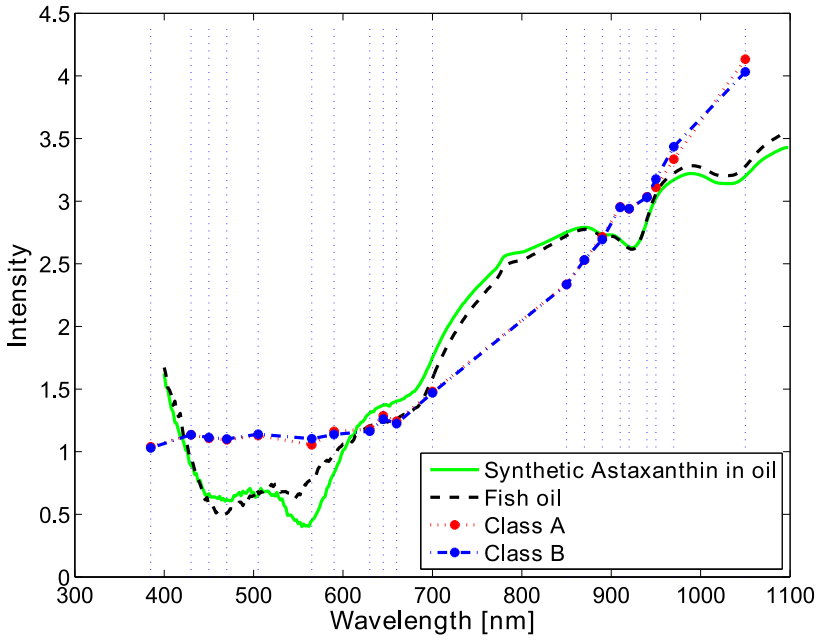

Figure B.3: Spectrometer reflectance of synthetic astaxanthin in oil (*green*) and plain fish oil (*black*). Multi-spectral images (reflectance) mean of group A (pellets with synthetic astaxanthin in fish oil) (*red*) and group B (pellets with fish oil) (*blue*) of the EcoLife20 type. Spectrometer spectra converted from absorption to reflectance. All spectra are normalised using SNV to fit in the same plot. The wavelengths captured for the images by the VideometerLab are marked by vertical dotted lines.

Table B.3: The misclassification of pellet coating type for different kinds of features. Displayed values are total test error for classification of the two groups A (astaxanthin) and B (base).

EcoLife20	LDA	QDA	SVM (RBF)	SVM (Poly)
Mean	0.0646	0.0901	0.1291	0.0811
Median	0.0736	0.0931	0.1456	0.0841
Mean, SNV, PC1-5	0.1396	0.2162	0.1727	0.1637
AquaLife R90				
Mean	0.0046	0.0031	0.0093	0.0031
Median	0.0015	0.0000	0.0185	0.0031
Mean, SNV, PC1-5	0.0185	0.0201	0.0155	0.0108

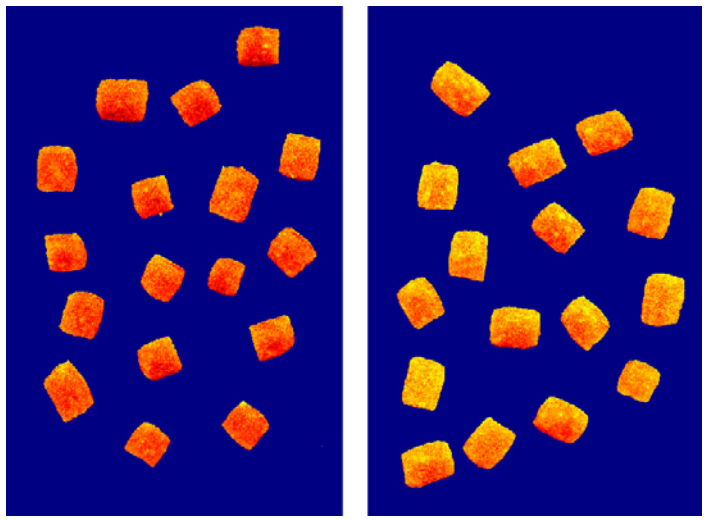

Figure B.4: The 2nd principal component of the multi-spectral image (reflectance) of EcoLife20 pellet pixels. Pellets coated with synthetic astaxanthin in fish oil, group A (*left*). Pellets coated with fish oil, group B (*right*).

on the pellet means showed better results using SVM than the LDA and QDA. LDA and QDA are quite quick to compute while the SVM takes significantly longer time.

To sum up, the results show that it is possible to distinguish between feed pellets with and without inclusion of synthetic astaxanthin in the coating using multi-spectral image analysis. However, more work is needed in order to make the method robust for different pellet types and also for different amounts of astaxanthin. Since astaxanthin is expensive, it is important to have a good accuracy in the method. This will later be of importance for developing rapid and non-invasive on-line quality food and feed products with optimal use of pigment and minimum amount of waste.

Acknowledgments

The work presented has received funding from BioMar A/S and the EU under the Seventh Framework Programme FP7/2007-2013 under grant agreement number 214505.10.

Appendix C

Multi-spectral Image Analysis for Robust Prediction of Astaxanthin Coating

Martin Georg Ljungqvist, Stina Frosch,

Michael Engelbrecht Nielsen, Bjarne Kjær Ersbøll

Long version submitted to Applied Spectroscopy 2012. A shortened version was accepted for publication in 2013 [90].

Abstract

The aim of this study was to investigate the possibility of predicting the presence, type and concentration level of astaxanthin coating of aquaculture feed pellets by multi-spectral image analysis. Both natural and synthetic astaxanthin was used, and several different concentration levels of synthetic astaxanthin in combination with four different recipes of feed pellets. The imaging device used was a VideometerLab with 20 spectral bands in the range of 385–1050 nm. Linear discriminant analysis (LDA), quadratic discriminant analysis (QDA), and sparse linear discriminant analysis (SLDA) was used for classification and variable selection. Partial least squares regression (PLSR) was used for prediction of the concentration level. The results show that it is possible to predict the level of synthetic astaxanthin coating using PLSR on either the same recipe, or when calibrating on all recipes. The concentration prediction is good enough for screening for all recipes, and suitable for quality control for two recipes. Moreover it shows that it is possible to predict the type of astaxanthin used in the coating using discriminant analysis. Also it shows that a filled dish of randomly placed pellets can be used for the inspection tasks. Finally, the most selected spectral bands are in the range of 400–600 nm, as well as just above 900 nm.

C.1 Introduction

Astaxanthin is a naturally occurring carotenoid with a high antioxidant activity essential for growth and survival and important for the development of colour in salmonid fishes [128]. The primary use of astaxanthin within aquaculture is as a feed additive to ensure that farmed salmon and trout have similar appearance to their wild counterparts [138]. Astaxanthin is very expensive [9] and therefore optimisation and quality control of its use in fish feed production is of importance.

Synthetic astaxanthin is more easily available and costs slightly less than natural astaxanthin and is therefore used more often in industry. However, there is a demand for natural astaxanthin for the organic salmonid fish market, where natural astaxanthin is mandatory.

An automatic vision system for at-line pigment quality control of concentration level and type would be of great benefit to the industry both in relation to process control and process optimisation. Furthermore, the astaxanthin coating type can be verified by the customers in the organic salmonid fish market.

Multi-spectral imaging of astaxanthin coating has previously been done in an earlier study by Ljungqvist et al.[87] which showed that it is possible to predict the presence of astaxanthin in fish feed pellet coating. However, they did not use different types of astaxanthin, nor did they use different concentration levels of astaxanthin coating.

Besides this, to the authors' knowledge, no further work has previously been done on analysing the coating of fish feed using image analysis. A study by Zhu et al. [159] used a spectroradiometer (325–1075 nm) for classification of four different fish feed pellet recipes, however they did not use image analysis.

Multi-spectral image analysis has shown good results in previous biological applications where it is of interest to detect subtle differences in colour and surface chemistry [19, 30, 31, 32, 37, 56, 74, 80, 110, 133, 140, 149].

The aim of this study is to investigate the possibility of predicting the presence, type and concentration level of astaxanthin coating of aquaculture feed pellets by multi-spectral image analysis. Furthermore, the aim is to make this coating prediction robust for different underlying pellet recipes in order to make a model that can predict astaxanthin coating irrespective of the composition of the underlying pellet recipe.

- Hypotheses: By multi-spectral image analyses it is possible to:

    1. Discriminate between synthetic astaxanthin coating and natural astaxanthin coating
    2. Discriminate between synthetic astaxanthin coating and fish oil coating
    3. Discriminate between synthetic astaxanthin coating and centrifuged synthetic astaxanthin coating
    4. Predict the concentration level of synthetic astaxanthin coating by regression analysis
    5. Predict the concentration level of synthetic astaxanthin coating by regression analysis – irrespective of the composition of the pellet recipe

Moreover, it is of interest to select the spectral bands of most importance for the particular problem. We also want to investigate if the analysis is influenced by the way the pellets are arranged geometrically. First investigating pellets standing on end or lying on their side, and finally investigating the difference in images with single pellets or clusters of pellets.

C.2 Materials and Methods

C.2.1 Pellets

Four different feed recipes with the same amount of protein (but of different origin) were investigated and all but one contained the same amount of oil, see Table C.1. The four recipes were all based on normal commercial fish feed for salmonid fish. The recipes were named after their dominant ingredient; the standard recipe was called control (CON), then there was maize gluten (MG), soya protein concentrate (60%) (SPC) and a control recipe with a different amount of oil (CON31). All pellets had an approximate production diameter of 4.5 mm.

The feed material was extruded through a die plate with holes of a certain diameter which determined the diameter of the pellets. On the other side of the disk was a set of rotating knives that cut the material into shorter cylinder-shaped pellets. Vacuum coating of the pellets took place after the extrusion. All pellets were stored dark and dry in sealed plastic bags for about twelve months between production and image acquisition.

Table C.1: Recipes of the pellets, with ingredient amount in percentage. The recipe names are: Control (CON), Maize gluten (MG), Soya protein concentrate (SPC), and Control 31 (CON31). All recipes have the same total amount of protein. CON, MG and SPC have the same total amount of oil.

Ingredients	CON	MG	SPC	CON31
Fish oil	17	18	21	24
Wheat flour	23	13	11	14
Fish meal	60	29	28	62
Maize gluten	0	40	0	0
Soya (60%)	0	0	40	0
Total	100	100	100	100
Total content				
Protein	45	45	45	45
Oil	24	24	24	31

C.2.2 Coating

The pellets included in this study consist of several classes; pellets coated with fish oil using different amounts of added synthetic astaxanthin (20, 40, 60, 80 parts per million (ppm)), as well as pellets coated with fish oil with 20 ppm of added natural astaxanthin. Moreover, a coating of only fish oil without additional astaxanthin was used. Fish oil in itself typically contains a small amount of natural astaxanthin, however this was assumed to be less than 1 ppm and here was referred to as a coating of 0 ppm concentration. Astaxanthin is commonly measured in ppm, and it is measured in mass so here ppm corresponds to mg/kg.

The pellets of recipe CON and CON31 had five coating concentration levels in total (0, 20, 40, 60, 80 ppm) of synthetic astaxanthin. The pellets of recipe MG and SPC had three concentration levels in total (0, 20, 60 ppm) of synthetic astaxanthin, see Table C.2.

The synthetic astaxanthin used was a cold water dispersible (BASF SE, Germany). It was dissolved in water.

The synthetic astaxanthin of 20 ppm was also centrifuged to be dissolved in oil.

The natural astaxanthin used consists of (a 50/50 mix of) mono- and di-esters of fatty acids. It was extracted from shrimps and was dissolved in oil [103].

The distribution of the surface coating was unknown and some amount of variation was likely to have occurred.

The common pellet compound for each recipe gives a spectral response which will be present for all concentration levels and astaxanthin types. Each pixel is thus a combination of the reflectance of a set of constituents. This mix was assumed to be of equal amount for each pellet recipe except for the difference of the astaxanthin coating concentration and astaxanthin type that we want to isolate in our model.

C.2.3 Equipment

The equipment used for image acquisition was a camera and lighting system called VideometerLab (Videometer A/S, Hørsholm, Denmark) which supports a multi-spectral resolution of up to 20 spectral bands [23]. These are distributed over the ultra-violet A (UVA), visible and first near infra-red (NIR) region.

Table C.2: All 18 available pellet types. Coating concentration of synthetic astaxanthin dissolved in fish oil, for the different pellet recipes. Amount of astaxanthin added to the fish oil coating in ppm. Fish oil coating is represented by 0 ppm.

Recipe	Astaxanthin	Concentration (ppm)				
CON	Synthetic	0	20	40	60	80
CON	Natural	-	20	-	-	-
CON	Synth Centr.	-	20	-	-	-
MG	Synthetic	0	20	-	60	-
SPC	Synthetic	0	20	-	60	-
CON31	Synthetic	0	20	40	60	80

The spectral range is from 385 to 1050 nm, see Table C.3. In comparison to spectroscopy, multi-spectral imaging includes both spectral information and spatial information simultaneously.

This system uses a Point Grey Scorpion SCOR-20SOM grey-scale camera. The objects of interest are placed inside an integrating sphere (Ulbricht sphere) with uniform diffuse lighting from light sources placed around the rim of the sphere. All light sources are light-emitting diodes (LED) except for 1050 nm which is a diffused laser diode. The curvature of the sphere and its matt-white coating ensure a uniform diffuse light so that specular effects are avoided and the amount of shadow is minimised. The device is calibrated radiometrically with a following light and exposure calibration. The system is also geometrically calibrated to ensure pixel correspondence for all spectral bands [48].

The image resolution is 1280 $\times$ 960 pixels. Each file contains 20 images, one for each spectral band. In this situation one pixel represents approximately 0.072 $\times$ 0.072 millimetres. The Scorpion camera has a 12 bit analogue to digital converter (ADC), and the system uses 8 bit data output from the camera. The correction for calibration gives reflectance intensity output of 32 bit precision.

C.2.4 Spectroscopy

In order to explore the spectral properties of astaxanthin further, a spectrometer was used. Absorption spectra of synthetic astaxanthin in a solution of fish oil along with plain fish oil were recorded in the visible and NIR range using a NIRSystems 6500 absorption spectrometer (Foss NIRSystems Inc, USA). The absorption spectra were transformed to reflection values using the standard

Table C.3: The wavelength of the light sources in the VideometerLab device and their spectral representation.

Band	Wavelength (nm)	Colour
1	385	Ultraviolet A
2	430	Violet
3	450	Violet, Blue
4	470	Blue
5	505	Green
6	565	Green
7	590	Yellow, Orange
8	630	Red
9	645	Red
10	660	Red
11	700	Red
12	850	NIR
13	870	NIR
14	890	NIR
15	910	NIR
16	920	NIR
17	940	NIR
18	950	NIR
19	970	NIR
20	1050	NIR

relation $A = -\log(R)$, where A is the absorption values and R is the reflection values. Every 2nd nanometre (nm) was recorded in the visible and NIR range.

C.2.5 Image Acquisition

A petri dish filled with pellets arranged randomly resembles the at-line inspection that industry would desire for this application. The situation represents the disordered way in which the pellets lie on the conveyor-belt and in the final bin at the end of the production line. In comparison to spectroscopy which measures a point, multi-spectral imaging also includes spatial information which covers many pellets simultaneously and would arguably give a more robust result.

For each of the total 18 pellet types (recipe, concentration level and astaxanthin type) a total of 4 images of scattered pellets (Scat) were acquired using the VideometerLab, and 4 images of filled plastic petri dishes (diameter 9 cm)

of pellets (Fill) were taken. Furthermore, a total of 60 Fill images of CON pellets with 20 ppm synthetic astaxanthin (30 images) and 20 ppm natural astaxanthin (30 images) coating were captured. The pellets were at normal room temperature during image acquisition.

The pellets were segmented from the light-grey background using a grey-scale threshold in combination with morphological methods [122].

For the Fill images, optimally the pellets should be segmented individually. However, since that was not feasible for this type of images the segmented pellet cluster was divided into subregions of maximally 100×100 pixels and the mean of each region was used as a sample. One full subregion represented approximately the area of three pellets. A subregion rather than the individual pellet was therefore considered a sample. This was done in order to increase the number of samples to avoid an ill-posed problem so we could complete the statistical analysis described in the section below. On average one image consisted of about 120 subregions (samples).

Adjacent subregions tend to be positively correlated (spatial autocorrelation), since one pellet can be divided and fall into several subregions, yet since we had a large number of subregions, the proportion of autocorrelated subregions was reduced and this was assumed not to affect the results.

For the Scat images the mean value of each pellet was used as a sample.

Standard red-green-blue (sRGB) colour image representations of the multi-spectral images for this paper were done by multi-spectral colour-mapping using penalised least square regression described in Dissing et al.[36].

C.2.6 Data Analysis

The analyses of the images of the pellets were done in order to investigate hypotheses 1–5 presented above.

The reference values (ground truth) was that we knew that the pellets were coated with a specific amount of synthetic or natural astaxanthin; the nominal values. However, since the surface distribution was unknown, the coating variation from pixel to pixel was unknown. A way to solve this was to represent each pellet in the Scat images using the pixel mean values as samples. In this manner we evened out the variance of all pixels in each pellet and a distinct sample was achieved; each pellet became an observation. For the Fill images, the mean of each subregion was used.

The number of samples is denoted n and the number of variables (the 20 spectral bands) is denoted p. The stored data of n samples and p variables is denoted as matrix $\mathbf{X}$. The ground truth reference values (the known concentration levels of astaxanthin) are stored in vector $\mathbf{y}$ with length n. The predicted (estimated) value of $\mathbf{y}$ is denoted $\hat{\mathbf{y}}$.

All image analyses and statistics were carried out using Matlab 7.9 (The Mathworks Inc., Natick, MA, USA).

C.2.6.1 Principal Component Analysis

The multivariate data from the images was analysed using principal component analysis (PCA) for exploratory purposes [53]. PCA is an unsupervised method, and the most optimal method with respect to maximising the variance [43, 63]. If the relation of interest contains large variation, then PCA is a good method for analysing the data. The pre-processing method, called standard normal variate (SNV) [117], was used, followed by PCA. SNV is performed by subtracting the mean and normalising using the standard deviation of the data.

C.2.7 Model Selection and Validation

In order to calibrate the statistical model parameters, a calibration set of 70% of the samples was used. Then the chosen model was validated on the remaining 30% of the validation samples. The calibration and validation set was chosen randomly, with all concentration levels present in both. The same calibration and validation set was used in all tests where calibration was needed.

For validation or parameter calibration of the statistical models the leave-one-out cross-validation (LOOCV) method was used, were each sample is used as validation once. For LOOCV the error rate is almost unbiased for the true (expected) prediction error, but in this case they could have high variance, since the training sets are so similar to each other [63].

When parameter calibration was needed, LOOCV was used on the calibration set. When calibration was not needed, the calibration set was used as a training set with the validation set as test set, and also in these situations, for comparison, LOOCV was used on the entire data set.

C.2.7.1 Discriminant Analysis

Statistical discriminant analysis of the images was made for testing hypotheses 1-3, as well as for performing classification of pellets lying on their side and standing on end. This analysis performed discrimination tests with only two groups of samples.

Since we have five distinct levels of synthetic astaxanthin concentration, we can perform discriminant analysis of this data regarding each concentration level as a group. This is a way of partly investigating hypotheses 4-5 to see if the concentration levels in the images are separable.

Hotelling's T^2 test was used in order to see if the two group means were significantly different [43, 66].

The classification methods used were linear discriminant analysis (LDA), quadratic discriminant analysis (QDA)[43], and sparse linear discriminant analysis (SLDA) [28].

The LDA and QDA are both based on the Mahalanobis distance, and assume that the observations in each group are normally distributed. LDA and QDA are based on a distance to the group mean weighted by the variance. LDA and QDA do not need calibration, so therefore both LOOCV on the training set, as well as the fixed training and test sets, were used independently to validate the discriminant models.

C.2.7.2 Variable Selection

In order to identify which wavelengths are of most interest for classification of coating types, two different methods were used.

The first method for evaluating spectral bands was LDA classification on all possible subsets of 1, 2 and 3 bands. LOOCV was used for each test and the lowest classification error was selected. The number of combinations for each subset size (cardinality) is equal to the binomial coefficient, using combinations without repetition. In this way we investigated which bands, and which combinations of bands, were important.

The other method was SLDA, which is designed for ill-posed problems where the number of variables is larger than the number of observations; a so-called large p small n problem ($p \gg n$). That was not the case in this study, but since

SLDA performs both variable selection and classification it suits our purposes well on those aspects. SLDA uses the elastic net (EN) for variable selection [160]. The EN tends to select variables that are correlated with each other.

Two model parameters are needed for EN: λ_1 for the L_1 norm for determining the number of non-zero coefficients, and λ_2 for the Euclidean L_2 norm for regularisation. The regularisation was less important here since we did not have ill-posed problems. The regression model consists of the variable weights (coefficients) in $\boldsymbol{\beta}^{en}$, see Equation C.1.

$$\beta_j^{en} = \underset{\beta_j}{\operatorname{argmin}}\left(\|\mathbf{y} - \mathbf{X}\beta_j\|_2^2 + \lambda_2\|\beta_j\|_2^2 + \lambda_1\|\beta_j\|_1\right). \tag{C.1}$$

The estimated coefficients are then multiplied by $(1 + \lambda_2)$ to get the final EN solution.

The two parameters were selected using LOOCV on the calibration set. The λ_1 parameter steers the selection of variables and was calculated so that the number of selected variables was varied from 1 to 10. The λ_2 parameter was varied with 12 logarithmic steps from 10^{-7} to 10. The data $\mathbf{X}$ was normalised before each calculation of the SLDA so that each variable got unit length.

The SLDA algorithm calculates one or more sparse discriminant component(s) that gives the best classification of the groups. The number of components is one less than the number of groups.

In order to compare LDA on subsets and SLDA we used Wilk's Λ, which in principle consists of the ratio of the within group variation ($\mathbf{W}$) and the total variation ($\mathbf{T}$), i.e. the within group plus the between group variation: $\Lambda = \frac{\det(\mathbf{W})}{\det(\mathbf{T})}$. A value of Wilk's Λ which is close to zero indicates that the two groups are well separated. The band combination with the lowest value of Wilk's Λ was chosen.

C.2.7.3 Regression

The concentration level was analysed using the partial least squares regression (PLSR) method [63, 131]. The number of samples in the calibration set was n_c, and the number of components (factors) n_f tested in the calibration step was varied from 1 to 20 (p). The data was mean centred, and the number of components to be used in the PLSR model was decided using LOOCV on

the calibration set, while minimising the prediction residual sum of squares (PRESS), see Equation C.2.

$$PRESS_{n_f} = \sum_{n_c} (\mathbf{y} - \hat{\mathbf{y}}_{n_f})^2 \,. \tag{C.2}$$

Then this model, using n_f components, was validated on the validation samples.

The coefficient of determination R^2 is a measure of how much variation is explained by the model and was calculated for the prediction of the validation set. R^2 is basically the ratio of the residual sum of squares (RSS) and the total sum of squares (TSS), see Equation C.3.

$$R^2 = 1 - \frac{RSS}{TSS} = 1 - \frac{\sum_{n_v} (\mathbf{y} - \hat{\mathbf{y}})^2}{\sum_{n_v} (\mathbf{y} - \frac{1}{n_v} \sum_{n_v} \mathbf{y})^2} \,. \tag{C.3}$$

Furthermore, the ratio of the standard error of prediction (RPD) was calculated as a measure of how well the model predicts. The RPD is the ratio between the standard error of prediction (SEP) and the standard deviation (SD) of the reference values $\mathbf{y}$ (the reference values): $RPD = SD/SEP$.

The SEP is equal to the root mean square error of prediction (RMSEP). An RPD value of 1.0 means that the model cannot predict accurately, since this means that the mean error is equal to the standard deviation of the reference values. An RPD value higher than 2.5 is considered satisfactory for screening, and values of 5–10 are adequate for quality control, according to Williams and Sobering [147].

C.2.8 Recipes

How the underlying pellet composition affects the image-based prediction of synthetic astaxanthin was also tested, in order to make a robust model that can predict astaxanthin coating irrespective of the composition of the underlying pellet recipe.

The prediction model from one recipe was used to predict the coating of another pellet recipe with either two groups (0, 60 ppm) or three groups (0, 20, 60 ppm) of coating with added synthetic astaxanthin. Further on, combinations of three recipes were used to train the prediction model and the remaining recipe was

used for prediction (test). Finally, all four recipes were used both for training and for testing, randomly divided into a training set (70% of the samples) and a test set (30% of the samples).

C.3 Results

The spectrometer results show a large spectral difference between fish oil with added (synthetic/natural) astaxanthin and plain fish oil in the range of 450 – 600 nm, as well as a spectral difference between fish oil with natural astaxanthin and fish oil with synthetic astaxanthin in the approximate range of 600 – 700 nm, see Figure C.1. The spectrometer results show similar characteristics and separation as the spectra from the VideometerLab images of astaxanthin in fish oil, see Figure C.2.

An example of a Scat image is shown in Figure C.3, and an example of a Fill image is shown in Figure C.4, and with subregions visualised in Figure C.5. Pellets with the centrifuged synthetic astaxanthin coating can be seen in Figure C.6, and with the natural astaxanthin coating in Figure C.7. All concentration levels of the CON pellets can be seen in Figure C.8, and the four different pellet recipes with plain fish oil coating can be seen in Figure C.9.

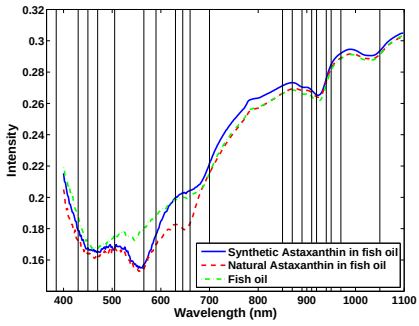

Figure C.1: Spectrometer spectra of synthetic astaxanthin in fish oil, natural astaxanthin in fish oil, and plain fish oil. The values are converted to reflectance. The wavelengths of the VideometerLab are marked by vertical lines.

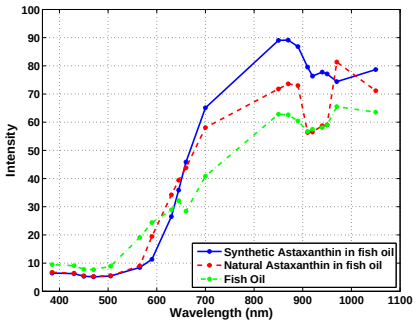

Figure C.2: VideometerLab reflectance spectra of synthetic astaxanthin in fish oil, and natural astaxanthin in fish oil, and plain fish oil.

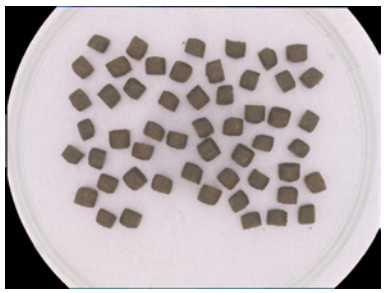

Figure C.3: Standard RGB version of a Scat image (scattered pellets lying on their side) of CON pellets with coating using synthetic astaxanthin level of 20 ppm.

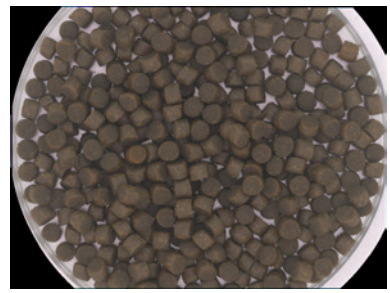

Figure C.4: Standard RGB version of a Fill image (a petri dish filled with pellets) of CON pellets with coating using synthetic astaxanthin level of 20 ppm.

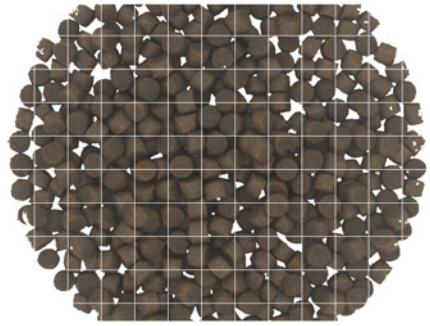

Figure C.5: The image in Figure C.4 (CON pellets with coating using synthetic astaxanthin level of 20 ppm), with the background segmented and subregions visualised.

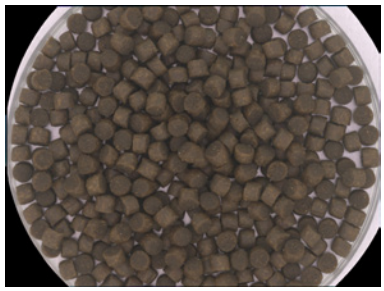

Figure C.6: Standard RGB version of a Fill image of CON pellets with coating using centrifuged synthetic astaxanthin level of 20 ppm.

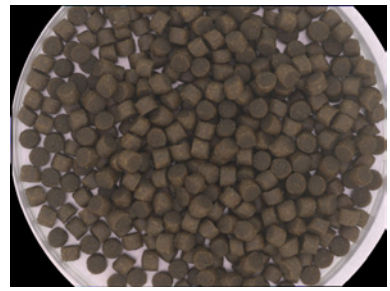

Figure C.7: Standard RGB version of a Fill image of CON pellets with coating using added natural astaxanthin level of 20 ppm.

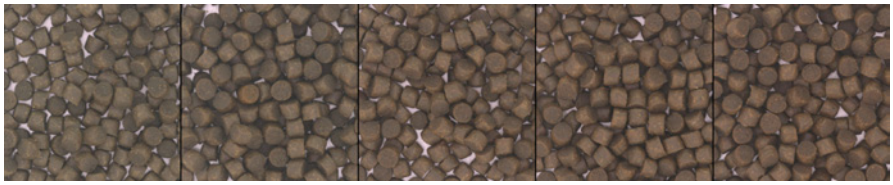

Figure C.8: Standard RGB version of Fill images of CON pellets. The concentration level of synthetic astaxanthin is from left to right: 0, 20, 40, 60, 80 ppm.

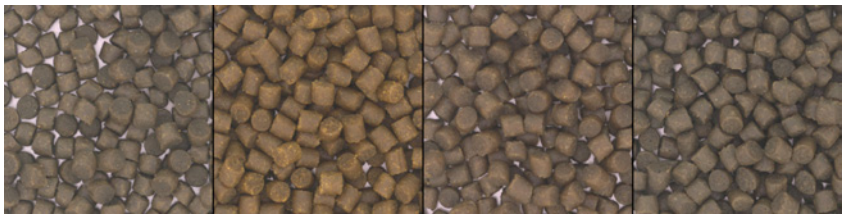

Figure C.9: Standard RGB version of Fill images of pellets with plain fish oil as coating (0 ppm). The pellet recipe from left to right is: CON, MG, SPC, CON31.

C.3.1 Classification

The investigation of the discrimination hypotheses 1, 2 and 3 is presented here, along with the investigation of the difference between the end and the side of the pellets. All two-group classification tests (see Table C.4 and 0, 60 ppm tests in Table C.5) have group means that are significantly different at a 0.1% significance level using Hotelling's T^2 test. This indicates that the spectral reflectance of the two groups in each test is separable.

The results also show that there is a distinct difference in the spectral response between the end and the side of the pellets since LDA gives 99.7% classification of pellets standing on end and lying on their side, see Table C.4. This does not necessarily mean that there is a difference in astaxanthin coating concentration between end and side. The mean standard deviation for all spectral bands for the pellets standing on end is 3.13, and for the pellets on their side (Scat) 3.60. In comparison, for the Fill images of the same pellet type, the standard deviation is 6.11.

Furthermore, LDA classification of synthetic astaxanthin coating (60 ppm) and fish oil coating (0 ppm) using Scat images gives a 100% correct classification

result. LDA on MG and SPC with levels 0, 20, and 60 ppm show that both Scat and Fill images give a classification of 99-100%, see Table C.5.

The discriminant analysis of the CON pellets shows that LDA performs a 99% classification of synthetic astaxanthin coating and natural astaxanthin coating, on both Scat and Fill images. The mean spectra of the two groups with one standard deviation marked can be seen in Figure C.10, where it shows that the two groups' mean spectra have a large overlap, while the standard deviations differs somewhat.

Using the method of LDA with subsets shows that LDA on combinations of three spectral bands gives a 95% classification of synthetic astaxanthin coating and natural astaxanthin coating on both Scat and Fill images, see Table C.6. The vast majority of the spectral bands chosen are in the range of 450 – 590 nm, which corresponds well to the spectrometer results of astaxanthin.

Wilk's Λ selects spectral bands in the range of 450 – 660 nm, which corresponds well to LDA subsets while it includes two longer wavelengths, see Table C.7.

Using SLDA on Scat images gives a 99% classification using 9 spectral bands, and for the Fill images gives a 98% classification using 10 bands, see Table C.8. The bands chosen cover the full range of the total 20 spectral bands used, with the majority in the visible range, and only two bands in the NIR range. The bands selected by SLDA include many of the bands selected by LDA subsets and Wilk's Λ. The two groups projected on the sparse discriminant component can be seen in Figure C.11.

Classification of synthetic astaxanthin coating and coating using centrifuged synthetic astaxanthin using LDA shows a 87% classification for Scat images, and only 70% for Fill images, see Table C.4.

By using three spectral bands on Scat images, LDA with subsets gives a classification of 80%, and only 67% using three bands on Fill images. The bands selected are mostly in the range of 430 – 505 nm for the Fill images. In contrast, for Scat images, mostly NIR bands are selected, see Table C.6.

Nevertheless, Wilk's Λ selects spectral bands mostly in the range of 385 – 470 nm, but for the Fill images the NIR band of 920 nm is also selected, see Table C.7.

Classification of synthetic astaxanthin coating and coating using centrifuged synthetic astaxanthin by SLDA gives an 85% classification using 10 bands on Scat images, and 68% using the Fill images, see Table C.8.

The classification of synthetic astaxanthin coating and coating using centrifuged synthetic astaxanthin using LDA, LDA subsets and SLDA all give better results for Scat images than for Fill images. However, they all give relatively poor results in comparison to classification between synthetic astaxanthin coating and natural astaxanthin coating.

In order to investigate whether it is reasonable to use the image subregions as sub-samples, the 60 Fill images of CON pellets were analysed in order to discriminate between synthetic and natural astaxanthin coating. The mean of the whole segmented pellet cluster in each Fill image was used as samples (n=60), and this was compared to subregions on 4 images of each group (n=1034). The results of this show that, for the mean values of the full pellet clusters, both LDA and QDA with LOOCV give 100% classification. For the subregions, the classification is about 99.9% for LDA and QDA, see Table C.4. This shows that it is possible to get approximately the same result with subregions as without subregions for this classification problem, so therefore it is sound to use subregions in this study.

Also, using these 60 images it was tested if one, two, three or four subregions per image might be enough to discriminate between these two groups. These subregions were in the centre of the segmented pellet cluster and the four subregions were not adjacent to each other. Using LDA and LOOCV it can be seen that using one subregion per image is enough to get a 100% correct classification of the type of astaxanthin coating used on the pellets. The same result was also achieved with 2, 3 and 4 subregions per image.

Table C.4: Classification of pellet coatings using LDA with LOOCV as well as with a training and test set. The total number of samples of each data set is presented. Fill: A filled petri dish subdivided into regions. Scat: Pellets scattered and segmented as individual pellets. Amount of astaxanthin added to the fish oil coating was 20 ppm.

Recipe	Test Groups	Image Type	LDA CV error	LDA Test error	Samples n
CON	Pellet end, Pellet side	–, Scat	0.0031	0.0000	320
CON	Synthetic, Natural	Scat	0.0065	0.0145	463
CON	Synthetic, Natural	Fill	0.0126	0.0097	1034
CON	Synthetic, S.Centrifuged	Scat	0.1297	0.1399	478
CON	Synthetic, S.Centrifuged	Fill	0.2972	0.2816	1033

Table C.5: Classification of concentration level of synthetic astaxanthin in the pellet coating using LDA with LOOCV as well as with a training and test set. The total number of samples of each data set is presented. Fill: A filled petri dish subdivided into regions. Scat: Pellets scattered and segmented as individual pellets. Amount (concentration) of astaxanthin added to the fish oil coating in ppm. Fish oil coating is represented by 0 ppm.

Recipe	Conc. Groups (ppm)	Image Type	LDA CV error	LDA Test error	Samples n
CON	0,60	Scat	0.0000	0.0000	363
CON	0,20,40,60,80	Scat	0.0316	0.0170	791
CON	0,20,40,60,80	Fill	0.0979	0.1044	2430
MG	0,60	Scat	0.0000	0.0000	277
MG	0,20,60	Scat	0.0000	0.0000	547
MG	0,20,60	Fill	0.0055	0.0092	1462
SPC	0,60	Scat	0.0000	0.0000	288
SPC	0,20,60	Scat	0.0020	0.0000	510
SPC	0,20,60	Fill	0.0030	0.0050	1343
CON31	0,60	Scat	0.0000	0.0000	388
CON31	0,20,40,60,80	Scat	0.0000	0.0000	1057
CON31	0,20,40,60,80	Fill	0.0225	0.0192	2442

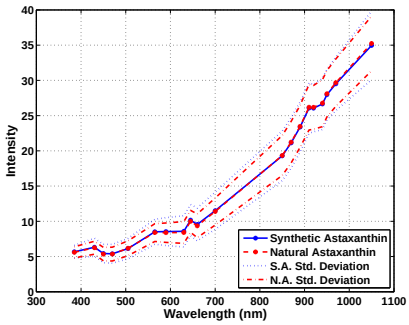

Figure C.10: VideometerLab reflectance spectra of CON Fill image subregions. Images of pellets with added synthetic astaxanthin and added natural astaxanthin, with one standard deviation visualised.

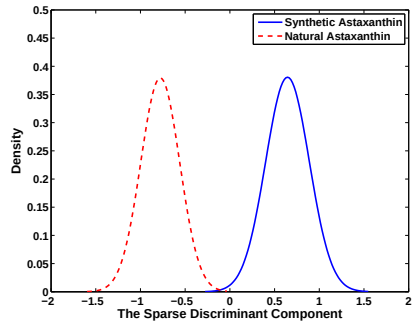

Figure C.11: Estimated density of CON Scat pellets with synthetic astaxanthin and natural astaxanthin, projected on the sparse discriminant component (SD) (consisting of 9 selected spectral bands) calculated by SLDA.

Table C.6: Classification of coating type using LDA on subsets (band combinations). Classification was done between synthetic and natural astaxanthin, as well as between synthetic astaxanthin and centrifuged synthetic astaxanthin, all of CON recipe. One band at a time was tested, along with two and three bands in combination. Lowest classification error presented along with the spectral band(s) used for the result.

Test	Image Type	Nbr of Band(s)	LDA CV error	Band(s) (nm)
Synth., Nat.				
	Scat	1	0.3261	450 nm
	Scat	2	0.1425	470, 505 nm
	Scat	3	0.0518	470, 505, 590 nm
	Fill	1	0.4845	1050 nm
	Fill	2	0.1799	450, 505 nm
	Fill	3	0.0474	450, 505, 565 nm
Synth., S.Centr.				
	Scat	1	0.4079	385 or 450 nm
	Scat	2	0.2469	890, 970 nm
	Scat	3	0.2092	890, 950, 970 nm
	Fill	1	0.4550	920 nm
	Fill	2	0.3466	450, 505 nm
	Fill	3	0.3291	430, 450, 505 nm

Table C.7: Variable selection for separation of coating type using Wilk's Λ with LOOCV on subsets (band combinations). Separation was done between synthetic and natural astaxanthin, as well as between synthetic astaxanthin and centrifuged synthetic astaxanthin, all of CON recipe. One band at a time was tested, along with two and three bands in combination. Lowest value of the LOOCV presented along with the corresponding spectral band(s).

Test	Image Type	Nbr of Band(s)	Wilk's Λ	Band(s) (nm)
Synth., Nat.				
	Scat	1	0.8300	450 nm
	Scat	2	0.8431	450, 660 nm
	Scat	3	0.8559	450, 470, 660 nm
	Fill	1	0.9978	660 nm
	Fill	2	0.9979	645, 660 nm
	Fill	3	0.9979	590, 645, 660 nm
Synth., S.Centr.				
	Scat	1	0.9338	430 nm
	Scat	2	0.9342	430, 450 nm
	Scat	3	0.9358	430, 450, 470 nm
	Fill	1	0.9945	920 nm
	Fill	2	0.9948	385, 920 nm
	Fill	3	0.9953	385, 430, 920 nm

Table C.8: Classification of coating type using SLDA. Classification was done between synthetic and natural astaxanthin, as well as between synthetic astaxanthin and centrifuged synthetic astaxanthin, all of CON recipe. Classification error on the validation set presented, along with the spectral bands used in the sparse discriminant component.

Test	Image Type	Nbr of Bands	SLDA Error	Bands (nm)
Synth., Nat.				
	Scat	9	0.0072	385, 450, 470, 505, 590, 630, 660, 850, 1050
	Fill	10	0.0161	385, 430, 450, 505, 590, 630, 645, 660, 850, 940 nm
Synth., S.Centr.				
	Scat	10	0.1469	385, 450, 630, 645, 660, 890, 920, 950, 970, 1050 nm
	Fill	10	0.3204	385, 430, 450, 505, 565, 590, 850, 910, 970, 1050 nm

C.3.2 Astaxanthin Concentration Level

The investigation of hypothesis 4, which is to predict the concentration level of synthetic astaxanthin coating, is presented here. The explorative analysis of the concentration level of synthetic astaxanthin coating using PCA on CON31 pellets shows that PC2 and PC3 seem to describe the concentration scale, however with large overlap, see Figure C.12.

For the classification of the five different concentration levels of synthetic astaxanthin coating of the CON pellets it turns out that the LDA gives a classification of 93.2% using the Scat images, and a classification of 90.2% using the Fill images. While the same levels for the CON31 pellets give a classification of 100% using the Scat images, and 97.8% using the Fill images, see Table C.5 for further results.

For PLSR the PRESS value drops significantly until 10 components approximately, and then flattens out for all tests. The PLSR results show good results for all recipes respectively with R^2 values above 0.9 both for Fill and Scat images, as well as RPD values above 3, which is considered good enough for screening [147], see Table C.9 and Figure C.13. For MG and SPC using Scat images the RPD is above 5, which is considered good enough for quality control. It shows that the results for the Scat images are better than the results for the

Fill images.

The PLSR components' weights show the contribution of different spectral regions to the model, and thus their significance. Looking at the 7 first components from the PLSR model of the CON31 pellets, we see that there are large weights between 400 and 600 nm, as well as just above 900 nm, with the large peaks around 450 - 505 nm, see Figure C.14. This well corresponds to the spectrometer results and with the band selection results shown above.

Table C.9: PLS regression for synthetic astaxanthin concentration level prediction. For CON and CON31 using synthetic astaxanthin with the concentration levels: 0, 20, 40, 60, 80 ppm, and for MG and SPC the levels are: 0, 20, 60 ppm.

Recipe	Image Type	Comp.	R^2 Calibr.	R^2 Pred.	SEC Calibr.	SEP Pred.	RPD
CON	Scat	12	0.9445	0.9414	5.9383	6.0125	4.1396
CON	Fill	14	0.9120	0.9148	8.4456	8.2693	3.4274
CON31	Scat	15	0.9496	0.9517	6.3635	6.1658	4.5597
CON31	Fill	14	0.9151	0.9114	8.2489	8.4279	3.3618
MG	Scat	13	0.9749	0.9718	3.6093	3.7612	5.9695
MG	Fill	14	0.9330	0.9239	6.5283	6.9120	3.6283
SPC	Scat	13	0.9680	0.9682	4.1889	4.0709	5.6287
SPC	Fill	12	0.9143	0.8411	5.6904	7.5572	2.5133

C.3.3 Recipe Tests

The investigation of hypothesis 5 is presented here, namely to see if it is possible to find a common component for astaxanthin prediction, independent of the underlying compounds in the recipes. It is of interest to see if the spectral characteristic of synthetic astaxanthin is clearly identifiable, independent of the base spectra from the pellet recipe in order to make a robust model.

The mean spectral reflection of each recipe, with a coating of 20 ppm synthetic astaxanthin in fish oil, can be seen in Figure C.15.

The model from one recipe was used to predict the coating on another pellet recipe with either two groups (0, 60 ppm) or three groups (0, 20, 60 ppm) of coating with added synthetic astaxanthin. Using LDA with two groups (0, 60 ppm) shows that models trained on MG and SPC data respectively can predict synthetic astaxanthin presence in any of the other three recipes with a 100% correct classification, see Table C.10. Likewise, CON31 showed good results for

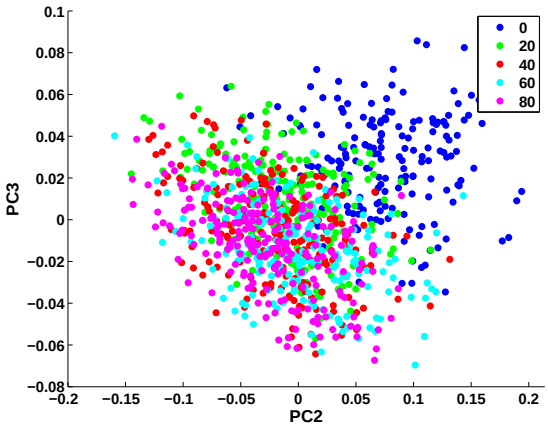

Figure C.12: Score plot of PC2 and PC3 from a PCA with SNV of Scat images of CON31 pellets with coating using synthetic astaxanthin levels of 0, 20, 40, 60, 80 ppm.

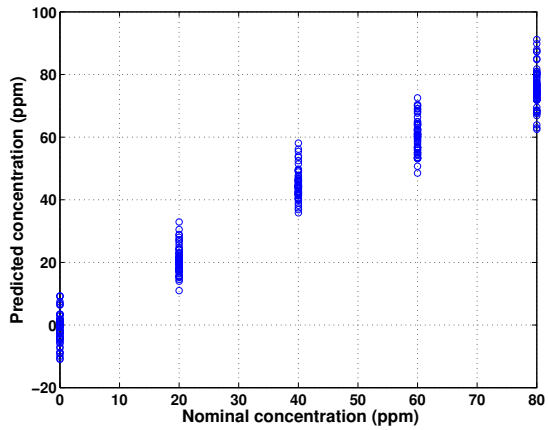

Figure C.13: PLSR prediction of synthetic astaxanthin concentration level (ppm) on the validation set, using Scat images of CON31 pellets, using 15 PLSR components.

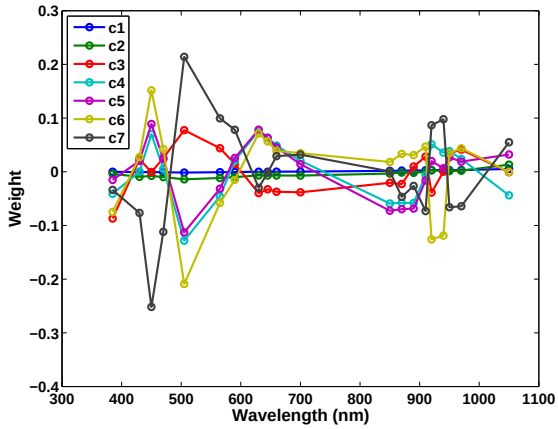

Figure C.14: PLSR components from the prediction of synthetic astaxanthin concentration level on the validation set, using Scat images of CON31 pellets. Here showing the first 7 of the total 15 PLSR components.

prediction on CON and SPC, while CON showed poor results for predicting synthetic astaxanthin presence on the other three recipes.

Coating concentration classification using LDA with three groups (0, 20, 60 ppm) shows that only three combinations give good results (MG-SPC, SPC-CON31, CON31-CON), see Table C.11. Conversely, the same tests using PLSR give different results, with only one combination showing good results (SPC-MG).

Moreover, all samples from the Scat images from all recipes were used together for training the model and testing it, and using LDA with LOOCV gave a 100% correct classification of the three groups of 0, 20 and 60 ppm synthetic astaxanthin. Using 1,2,3-subset LDA shows that the two best bands are 450 and 505 nm, which corresponds partly to the spectrometer and VideometerLab spectra.

However, if we leave one recipe out of the training set and use it for testing the model, then the results show that the acquired model has problems predicting some of the recipes as an unseen recipe, see Table C.12.

Classification using QDA often got approximately the same result as LDA, and sometimes worse results. QDA was only significantly better than LDA in two cases: MG as training, CON as test for 0, 20, 60 ppm. This implies that the problem in general is best treated as linear.

Using LDA with 1,2,3-subsets on all recipes shows good results for a combination of three bands, where 450, 505 and 1050 nm were selected, see Table C.13.

Prediction of astaxanthin coating by PLSR with one recipe as training and another as test shows that SPC is very good at predicting MG, while the other combinations show poor results, see Table C.14. Furthermore, if we use three recipes for training and the remaining recipe as test, the results are somewhat more robust than when using only one recipe for training, but none of them show very good results. When using all four recipes for calibration (training) and validation (test) we get very good results with an R^2 value above 0.9 and an RPD above 4, see Table C.15.

Table C.10: Classification with LDA and QDA of pellet coating with two groups (0, 60 ppm) and using one pellet recipe for training the classification model and another recipe for prediction (test), using Scat images. Amount (concentration) of synthetic astaxanthin added to the fish oil coating in ppm.

Recipe Train	Recipe Test	Conc. (ppm)	LDA Test error	QDA Test error
CON	MG	0,60	0.4224	0.4224
CON	SPC	0,60	0.5278	0.4757
CON	CON31	0,60	0.4768	0.4768
MG	CON	0,60	0.0000	0.0000
MG	SPC	0,60	0.0000	0.0000
MG	CON31	0,60	0.0000	0.0284
SPC	CON	0,60	0.0000	0.0000
SPC	MG	0,60	0.0000	0.0108
SPC	CON31	0,60	0.0000	0.2371
CON31	CON	0,60	0.0039	0.0000
CON31	MG	0,60	0.4224	0.4224
CON31	SPC	0,60	0.0000	0.0000

C.4 Discussion

The spectrometer results and the reflection spectra from the VideometerLab images partly corresponds to previous studies of astaxanthin [3, 21, 156] where they found absorbance peaks of astaxanthin around 450 – 505 nm and also secondary peaks around 500 – 600 nm for various solvents, as well as at 870 nm.

Hotelling's T^2 calculates the statistical significance of the difference between

Table C.11: Classification with LDA and QDA of pellet coating using with three groups (0, 20, 60 ppm) and one pellet recipe for training the classification model and another recipe for prediction (test), using Scat images. Amount (concentration) of synthetic astaxanthin added to the fish oil coating in ppm.

Recipe Train	Recipe Test	Conc. (ppm)	LDA Test error	QDA Test error
CON	MG	0,20,60	0.7057	0.7057
CON	SPC	0,20,60	0.7333	0.7333
CON	CON31	0,20,60	0.6667	0.6667
MG	CON	0,20,60	0.3499	0.2464
MG	SPC	0,20,60	0.0392	0.1824
MG	CON31	0,20,60	0.6223	0.6371
SPC	CON	0,20,60	0.4472	0.4720
SPC	MG	0,20,60	0.2139	0.2139
SPC	CON31	0,20,60	0.0016	0.4631
CON31	CON	0,20,60	0.0041	0.1263
CON31	MG	0,20,60	0.7057	0.7057
CON31	SPC	0,20,60	0.4000	0.4333

Table C.12: Classification with LDA and QDA of pellet coating using Scat images and three pellet recipes for training the classification model and one recipe for prediction (test). Amount of synthetic astaxanthin added to the fish oil coating in ppm.

Recipe Train	Recipe Test	Conc. (ppm)	LDA Test error	QDA Test error
CON, MG, SPC	CON31	0,60	0.0000	0.0000
CON, MG, CON31	SPC	0,60	0.0000	0.0000
CON, SPC, CON31	MG	0,60	0.4224	0.0000
MG, SPC, CON31	CON	0,60	0.6693	0.0000
All	All	0,60	0.0000	0.0000
CON, MG, SPC	CON31	0,20,60	0.0099	0.2020
CON, MG, CON31	SPC	0,20,60	0.0392	0.0314
CON, SPC, CON31	MG	0,20,60	0.5320	0.2139
MG, SPC, CON31	CON	0,20,60	0.3582	0.4431
All	All	0,20,60	0.0000	0.0000

Table C.13: Classification of concentration level of synthetic astaxanthin coating using LDA on subsets (band combinations). All four recipes were used. One band at a time was tested, along with two and three bands in all possible combinations. The lowest classification error is presented along with the spectral bands used for the result. For these tests the concentration levels of synthetic astaxanthin are: 0, 20, 60 ppm.

Test	Image Type	Nbr of Band(s)	LDA CV CV error	Band(s) (nm)
Conc. Level				
	Scat	1	0.4132	505 nm
	Scat	2	0.1582	450, 505 nm
	Scat	3	0.0800	450, 505, 1050 nm

Table C.14: PLS regression on Scat images for synthetic astaxanthin concentration level prediction. For these tests the concentration levels of synthetic astaxanthin are: 0, 20, 60 ppm. SEC and SEP can be interpreted as the error of the model, measured as the amount of synthetic astaxanthin added to the fish oil coating in ppm.

Recipe Train	Recipe Test	Comp.	R^2 Calibr.	R^2 Pred.	SEC Calibr.	SEP Pred.	RPD
CON	MG	12	0.9873	-0.5363	2.3294	27.7238	0.8075
CON	SPC	12	0.9873	0.0734	2.3294	22.0534	1.0399
CON	CON31	12	0.9873	0.6519	2.3294	14.4779	1.6963
MG	CON	16	0.9744	-4.5516	3.6388	48.0869	0.4249
MG	SPC	16	0.9744	0.3475	3.6388	18.5067	1.2392
MG	CON31	16	0.9744	0.5313	3.6388	16.8007	1.4618
SPC	CON	13	0.9687	0.0077	4.1103	20.3301	1.0049
SPC	MG	13	0.9687	0.9470	4.1103	5.1514	4.3460
SPC	CON31	13	0.9687	0.7823	4.1103	11.4494	2.1450
CON31	CON	12	0.9687	-1.4799	4.3870	32.1394	0.6357
CON31	MG	12	0.9687	-4.5632	4.3870	52.7573	0.4244
CON31	SPC	12	0.9687	-2.7782	4.3870	44.5323	0.5150

Table C.15: PLS regression for synthetic astaxanthin concentration level prediction. For these tests the concentration levels of synthetic astaxanthin are: 0, 20, 60 ppm. Scat images. SEC and SEP can be interpreted as the error of the model, measured as the amount of synthetic astaxanthin added to the fish oil coating in ppm.

Recipe Train	Recipe Test	Comp.	R^2 Calibr.	R^2 Pred.	SEC Calibr.	SEP Pred.	RPD
CON,MG,SPC	CON31	18	0.9610	0.7771	4.4098	11.5849	2.1199
CON,MG,CON31	SPC	14	0.9329	0.6231	5.9638	14.0650	1.6305
CON,SPC,CON31	MG	16	0.9309	0.6761	6.0892	12.7290	1.7588
MG,SPC,CON31	CON	15	0.9301	0.7291	6.2091	10.6226	1.9233
All	All	17	0.9256	0.9457	6.2934	5.3342	4.2956

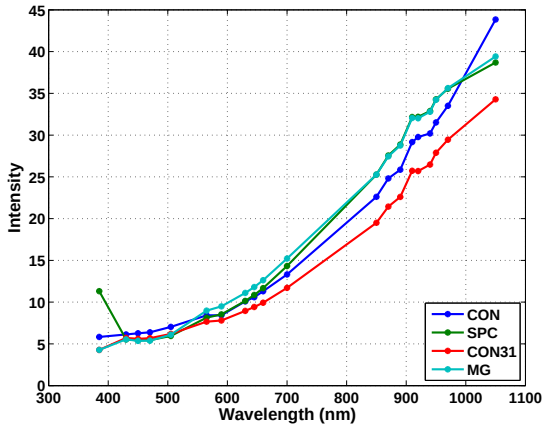

Figure C.15: VideometerLab mean spectra of pellets from each recipe, using Fill images of pellets with coating using synthetic astaxanthin level of 20 ppm.

group means. However, since we have a large number of correlated samples, this affects the significance value in an optimistic way and the difference might not necessarily be significant in practice.

The difference in spectral response between pellet end and side is possibly explained by the way the extruder machine produces the pellets. The Scat images only contain pellets lying on their side, while the pellets in the Fill images contain pellets placed randomly – i.e. both side and end are visible. The higher variation in the Fill images than in the Scat images might be explained by this and it might also explain the slightly better results for Scat images.

The classification between synthetic astaxanthin and natural astaxanthin coating works well using 10 or less bands, while the regression problem for concentration level of synthetic astaxanthin needs more than 10 components. Creating a model for the concentration level seems more complex, probably because the coating layer is relatively thin and the reflection of the astaxanthin coating is mixed with the background (the pellet compound). Also, a PLSR component is a linear combination of all 20 spectral bands, so it is not exactly comparable with selected bands of the classification methods.

The classification between synthetic astaxanthin and centrifuged synthetic astaxanthin coating seems to be a harder problem than classification between synthetic astaxanthin and natural astaxanthin coating.

Building a statistical model using 1,2,3-subset LDA with 20 variables takes a reasonable time, but for larger numbers of variables or combinations it will be time consuming, while SLDA performs less calculations since it does not test all subsets of variables. Also SLDA selects more spectral bands than subset LDA for a good classification; this could perhaps be explained by the grouping effect of the elastic net used by SLDA, which has a tendency to select sets of variables that are correlated.

The large difference in results between PLSR and LDA or QDA is mainly because PLSR and discriminant analysis work quite differently.

When all pellet recipes are included in the training set for PLSR prediction, the R^2 for prediction is higher than that for calibration (under-fit), which is considered to be a result of the recipe variation in the data.

The storage time of the pellets between production and imaging in this study will affect the astaxanthin concentration in the coating since astaxanthin oxidise with time. This might affect the spectral response of astaxanthin coating, however, it could not be found in the literature how much astaxanthin oxidise with time. There might be a difference in the astaxanthin coating spectra characteristics

in comparison with a real-time production situation. The results presented here indicate that there are still detectable amounts of astaxanthin after storage.

The results are satisfactory for screening the astaxanthin concentration level, but they are not good enough for quality control for all recipes. For MG and SPC using Scat images the RPD is above 5, which is considered good enough for quality control. The high prediction error (SEP) in most tests is also indicated by the RPD values. All concentration level predictions have an error in the approximate range of 4–8 ppm, which is considered high for the industry. It would be of interest to see whether more spectral bands in the critical regions produce better results. Since the visual inspection system is intended to be at-line, there would be time to capture more wavelengths if necessary. Also it would be of interest to investigate the astaxanthin coating in the production, without having been stored for a time, which likely would improve the inspection results.

It seems as the best regression results for different recipes are achieved when calibrating and validating on the same pellet recipe, or when calibrating on all recipes simultaneously, see Tables C.9 and C.15. This procedure could also be valuable when using the same recipe but with varying ingredient batches, since the raw material ingredients of any one recipe may well vary depending on availability and price.

C.5 Conclusions

The results show that it is possible to predict the synthetic astaxanthin concentration in the coating using multi-spectral image analysis. The best results for different recipes are achieved when calibrating and validating on the same pellet recipe, or when calibrating on all recipes. So in order to make a robust prediction model, all relevant recipes should be included in the calibration. The results are good enough for screening the astaxanthin concentration level. For MG and SPC using Scat images, the results are considered good enough for quality control.

There is a clear tendency that Scat images produce better results than Fill images. The Fill images contain more variation because the pellets are not ordered. Having said that, it must be emphasised that both Scat and Fill images show promising results, so even if Scat images get better results, it is now clear that Fill images can also be used for the inspection tasks. This is very promising since Fill images resemble the rapid at-line inspection suitable for the production.

Moreover, we have shown that it is possible to predict the type of astaxanthin used in the coating. The classification of synthetic astaxanthin coating and natural astaxanthin coating gives good results using only three spectral bands, and gives overall better results in comparison to classification between synthetic astaxanthin coating and coating using centrifuged synthetic astaxanthin.

The most common spectral bands selected for classification are in the VIS range of 450–600 nm, as well as NIR bands above 900 nm. Corresponding spectral weights can be seen in the PLSR components for synthetic astaxanthin concentration prediction.

Acknowledgements

The work presented has received funding from BioMar A/S and the EU under the Seventh Framework Programme FP7/2007-2013 under grant agreement number 214505.10.

Appendix D

Near-Infrared Hyper-spectral Image Analysis of Astaxanthin Concentration in Fish Feed Coating

---

Martin Georg Ljungqvist, Ken-ichi Kobayashi, Stina Frosch,

Michael Engelbrecht Nielsen, Bjarne Kjær Ersbøll, Shigeki Nakauchi

Presented and in the proceedings of the IEEE International Conference on Imaging Systems and Techniques, Manchester, United Kingdom, 2012 [89] .

Abstract

The aim of this study was to investigate the possibility of predicting concentration levels of synthetic astaxanthin coating of aquaculture feed pellets by hyper-spectral image analysis in the near infra-red (NIR) range and optical filter design. The imaging devices used were a VideometerLab with 20 wavelengths in the range of 385-1050 nm, and a Specim camera with 256 wavelengths in the range of 970–2500 nm. Linear discriminant analysis (LDA), partial least squares regression (PLSR), and a modified stepwise random selection with ordinary least squares (OLS) for filter selection was used for prediction of the concentration level. The results show that it is possible to predict the level of synthetic astaxanthin coating using either hyper-spectral imaging or three bandpass filters (BPF).

D.1 Introduction

Astaxanthin is a naturally occurring carotenoide with a high antioxidant activity, essential for growth and survival, and important for the development of colour in salmonide fishes [128]. The colour appearance of fish products is important for customers as a quality indicator [108]. Astaxanthin is very expensive [9] and therefore optimisation of its use in fish feed production is of importance.

An automatic vision system for at-line pigment quality control of the concentration level will be of great benefit to the industry, both in relation to process control and process optimisation.

Previous work on analysing fish feed pellets in the near infra-red (NIR) range above 1000 nm has e.g. been done in the range of 1100 to 1690 nm by Fernández-Ahumada et al. (2010) [44], as well as in the range of 400 to 2498 nm by Garrido-Varo et al. (2005) [52]. However, their classification was dependent on the feed ingredients and used spectroscopy; neither analysed pellet coatings, nor did they use image analysis.

Multi- and hyper-spectral image analysis has shown good results in previous biological applications where it is of interest to detect subtle differences in colour and surface chemistry [19, 30, 31, 37, 56, 74, 133, 140, 149].

Investigation of the spectral properties of astaxanthin in the NIR range above 1000 nm has been done by Yamane et al. (1996), who measured absorbance in the range of 1100–2500 nm using a spectrophotometer [153], and Amarie et al.

(2010), who used a spectrometer up to about 1400 nm [3].

Previous studies of astaxanthin coating have shown that it is possible to predict the presence and concentration level of astaxanthin in pellet coatings using multi-spectral image analysis [87, 89], however those studies were based on only 20 wavelengths in the visual range and parts of the NIR range.

However, to the authors' knowledge no hyper-spectral image analysis of astaxanthin has been done in the spectral range above 1050 nm. It is therefore of interest to investigate the characteristics of astaxanthin coating using hyper-spectral imaging in the NIR range.

The aim of this study is to investigate the possibility of predicting the concentration level of synthetic astaxanthin coating of aquaculture feed pellets by NIR hyper-spectral image analysis. It is of interest to investigate what spectral features are of importance for a sparse filter-based prediction model. By constructing optical filters that are ideal for inspection of astaxanthin, we can avoid the need to use expensive hyper-spectral imaging devices, and improve the signal-to-noise ratio (SNR) compared to narrow bands while also reducing the time for inspection.

We also want to investigate if the analysis is influenced by the way the pellets are arranged geometrically, by investigating the difference in images with single pellets lying on their side, and clusters of many pellets.

This paper is based on an earlier study; the NIR results in this study will be compared to the multi-spectral studies in the visual and lower parts of the NIR range up to 1050 nm by Ljungqvist et al. (2012) [89].

D.2 Materials and Methods

D.2.1 Pellets

A standard control recipe of fish feed pellets was used. It was based on normal commercial feed for salmonide fish and consisted mainly of fish meal.

D.2.2 Coating

The pellets used were coated with five different concentrations of added synthetic astaxanthin (0, 20, 40, 60, 80 ppm). The synthetic astaxanthin used was cold water dispersible (BASF SE, Germany).

D.2.3 Equipment

Three spectral devices were used for data acquisition.

D.2.3.1 Spectrometer

In order to explore the spectral properties of astaxanthin a spectrometer was used. Absorption spectra of astaxanthin were recorded in the visible and NIR range using a NIRSystems 6500 absorption spectrometer (Foss NIRSystems Inc, USA). The absorption spectra were transformed to reflection values using the standard relation $A = -\log(R)$, where A is absorption values and R is the reflection values. Every 2nd nanometre (nm) was recorded in the range from 400 to 2498 nm.

D.2.3.2 VideometerLab

The equipment used for image acquisition was a camera and lighting system called VideometerLab (VML) (Videometer A/S, Hørsholm, Denmark) which supports a multi-spectral resolution of 20 wavelengths [48]. These are distributed over the ultra-violet A (UVA), visual and lower wavelengths of the NIR region: 385, 430, 450, 470, 505, 565, 590, 630, 645, 660, 700, 850, 870, 890, 910, 920, 940, 950, 970, 1050 nm, as described in Ljungqvist et al. (2012) [87].

D.2.3.3 Hyper-spectral Device

A line-scan Specim camera was used (Spectral Camera SWIR; SPECIM Spectral Imaging Ltd, Finland), together with three halogen light sources (MH-M15, 150 W; Hataya Ltd, Japan) and a linear slide table moving the sample at constant speed. Spectral range used was 970–2500 nm using a step size of 6.3 nm, resulting in 256 captured spectral bands in the NIR range [74]. The line-scan

resolution was 320 pixels (X-axis), and the final image resolution was 320×350 pixels. The exposure time was 5.5 ms, and the images were of 14 bits precision.

For each sample image (I_{Sample}), two calibration images were taken, one of standard white with 98% reflection (I_{White}) and the second of dark current with the camera shutter closed (I_{Dark}). This results in a calibrated reflectance image I_R, see Equation D.1. Since the Specim camera is a line-scan camera, the images were calibrated on a pixel line basis (X-axis).

$$I_R = \frac{I_{Sample} - I_{Dark}}{I_{White} - I_{Dark}} \tag{D.1}$$

D.2.4 Image Acquisition

Images of the feed pellets lying on their side were captured using both the VideometerLab and Specim set-up.

A petri dish filled with pellets resembles the rapid at-line inspection that the industry would desire for this application.

For Specim, the Scat images were captured with a dark background to avoid shadows from the direct light sources and thereby improve segmentation of pellets, while the Fill images were captured using a standard white background.

Four images of scattered pellets (Scat) of each type were used for VideometerLab using a grey background, 5 images of scattered pellets of each type were used for Specim using a black background, and 4 images of filled plastic petri dishes (diameter 9 cm) of pellets (Fill) of each type were used for both VideometerLab (grey background) and Specim (white background). The VideometerLab Fill images were subdivided into regions of 100×100 pixels, the Specim Fill images were subdivided into regions of 30×30 pixels due to smaller image size.

The pellets were segmented from the background using a grey-scale threshold in combination with morphological methods [122].

For the Fill images the segmented pellet cluster was then divided into subregions of maximally 100×100 pixels and the mean of each region was used as a sample. The individual pellets were in this case not seen as samples, rather was the whole pellet cluster, divided into subregions regarded as samples. This was done in order to increase the number of samples and in that way avoid an ill-posed

problem and enable us to do the statistical analysis described in the section below.

The adjacent subregions will be positively correlated since one pellet can be divided so that it is part in several subregions, however since we get a large number of subregions, the amount of correlated subregions will be reduced and this is assumed not to affect the results.

For the images of scattered pellets, each pellet was segmented individually from the background and the mean value of each pellet was used as a sample.

Standard red-green-blue (sRGB) colour image representations of the multi-spectral VideometerLab images for this paper were made by multi-spectral colour-mapping using penalised least square regression described in Dissing et al. (2010) [36].

D.2.5 Data Analysis

The images of the pellets were analysed according to the hypotheses presented above. Since each pellet in the Scat images was represented as a mean spectrum, we evened out the variance of all pixels in each pellet and a distinct sample was achieved. For the Fill images the mean of each subregion was used. The pre-processing method called standard normal variate (SNV) was used for visualising the spectra [117]. All image analyses and statistics were carried out using Matlab 7.9 (The Mathworks Inc., Natick, MA, USA).

D.2.5.1 Discriminant Analysis

Since the concentration levels were discrete, we could perform statistical discriminant analysis on the data, using linear discriminant analysis (LDA) [43]. This was a way of investigating whether the five different concentration levels in the images were separable.

To validate the discriminant models, the leave-one-out cross-validation (LOOCV) method was used, where each sample was used as validation once [63]. To complement this, a training set of 70% of the samples along with a test set of 30% of the samples was used.

D.2.5.2 Regression

The concentration level was analysed using the partial least squares regression (PLSR) method [63, 131]. The data was mean-centred, and the number of components to be used in the PLSR model was decided using LOOCV on 70% of the samples while minimising the prediction residual sum of squares (PRESS). The model was validated on the remaining 30% validation samples.

R^2 is a measure of how much variation is explained by the model and was calculated for the prediction of the validation set. Further on, the ratio of the standard error of prediction (RPD) was calculated as a measure of how well the model predicts. The RPD is the ratio between the standard error of prediction (SEP) and the standard deviation (SD) of the original data (the reference values).

The SEP is equal to the root-mean-square error of prediction (RMSEP). An RPD value of 1.0 means that the model cannot predict accurately. An RPD value higher than 2.5 is considered satisfactory for screening, and values of 5–10 are adequate for quality control [147].

D.2.5.3 Filter Design

In order to further investigate what parts of the spectrum were of interest with respect to analysing astaxanthin, we used a method for designing optical filters. The method aimed at selecting a number of ideal rectangle-shaped band pass filters (BPF) and was described in Kobayashi et al. (2011) [76] and Nakauchi et al. (2012) [102]. The filter properties consisted of the centre wavelength (λ_c) and the half-bandwidth (w_h).

The filter design method uses ordinary least squares (OLS) regression and is iteratively trying to find optimal filter parameters by minimising root-mean-square error of cross-validation (RMSECV). The method chooses a centre wavelength and width for the BPF. When the first BPF is found it is fixed while choosing the second one, and so forth. Stepwise random selection was used, as described in point 1-9 in [76].

We optimised for 3 filters, and used 100,000 iterations for the search step. The minimum band width was limited to 50 nm, and the maximum to 1000 nm. The number of possible combinations of 3 BPFs was approximately 10^{12}.

D.3 Results

The spectrometer results show a large spectral difference between fish oil with added synthetic astaxanthin and plain fish oil in the visual range of 500–600 nm, see Figure D.1. This partly corresponds to previous studies of astaxanthin in the visual range [3, 21, 156]. In the NIR regime the difference between the two types is around 1100–1200 nm, 1300 nm, 1400 nm and above 1600 nm, which partly corresponds to the astaxanthin absorption peaks found in previous studies [3, 153].

An sRGB representation of a VideometerLab Scat image is shown in Figure D.2, and an sRGB version of a Fill image with subregions visualised is shown in Figure D.3. An example of a Specim Scat image is shown in Figure D.4, and a Fill image with subregions visualised is shown in Figure D.5.

The mean spectra of each astaxanthin concentration level shows that the five different levels are separated at 1100 nm and 1300 nm as well as in the range of 1400–1500 nm, when looking at the Fill Specim images, see Figure D.6.

For classification of the five levels of synthetic astaxanthin coating concentration, the LDA results from the VideometerLab images for synthetic astaxanthin concentration level are about 90–97% classification. The LDA results from the Specim images for synthetic astaxanthin concentration level are about 78-95% classification, see Table D.1

The calibration and validation results of PLS regression are shown in Table D.2. The PLSR results show good results for the VideometerLab images with R^2 values above 0.9 both for Fill and Scat images, as well as RPD values above 3, which is considered good enough for screening, see Figure D.7. For the Specim images the RPD is about 1.24, for Scat images and 2.15 for Fill images, see Figure D.8. The result of using the Specim images is not as good as the results using the VideometerLab images, even though the regression model needs fewer components for the VideometerLab images than for the Specim images.

The PLSR components when using Specim Fill images have large peaks at 1100 nm and 1300 nm, see Figure D.9. These are the same regions of the spectra where we could see a difference between the five different concentration levels in Figure D.6. Furthermore the PLSR components show peaks around 1600 nm and 1700 nm.

The results of the filter selection method are shown in Table D.3. It shows that the VideometerLab images get better results than the Specim images, both for Fill and Scat. The VideometerLab images get an RMSECV of 8.7 for Scat

Table D.1: Tests performed on VideometerLab and Specim images using LDA. Fill: A filled petri dish subdivided into regions. Scat: Pellets scattered and segmented as individual pellets. VML: VideometerLab. Amount of synthetic astaxanthin added to the fish oil coating: 0, 20, 40, 60, 80 ppm.

Image Type	LDA CV test error	LDA Test error	Samples n
VML			
Scat	0.0316	0.0170	791
Fill	0.0979	0.1044	2430
Specim			
Scat	0.2120	0.2208	2151
Fill	0.0470	0.0482	1042

images, and 14.0 for Fill images, while the Specim images get 27.6 for Scat images and 22.7 for Fill images.

For the VideometerLab Scat images two bands are located in the range of 405 to 515 nm in the visual range, and the third band at 925-1015 nm in the NIR range, see Figure D.10. For the VideometerLab Fill images all three filters are located in the NIR range of 832.5-1015 nm, see Figure D.11. The Specim Scat images have two filters in the range of 1439-1641 nm NIR range, while the Fill images have all three filters in the range of 1439-1634 nm.

For the VideometerLab images, the Scat images (scattered single pellets) give better results for all three methods than the subdivided Fill images. On the other hand, the Scat images using the Specim images showed poorer results than the subdivided Fill images, see Tables D.1, D.2, and D.3.

Investigating the variance in the 20 ppm images, it is shown that the mean standard deviation of the segmented pixels in all bands in the VideometerLab Scat images is 3.60, and for the Fill images the standard deviation is 6.11. For Specim the standard deviation for Scat images is 0.3789, and for Fill it is 0.0530.

D.4 Discussion

The results show that Scat is better than Fill for the VideometerLab images, but that Fill is better than Scat for the Specim images. This could partly be explained by the difference in variance between the two types of images and

Table D.2: PLS regression for synthetic astaxanthin concentration level prediction. VML: VideometerLab. Synthetic astaxanthin in the concentration levels: 0, 20, 40, 60, 80 ppm.

Image Type	Comp	R^2 Calibr.	R^2 Pred.	SEC Calibr.	SEP Pred.	RPD
VML						
Scat	12	0.9445	0.9414	5.9383	6.0125	4.1396
Fill	14	0.9120	0.9148	8.4456	8.2693	3.4274
Specim						
Scat	20	0.5019	0.3433	20.5032	23.3822	1.2350
Fill	24	0.8555	0.7837	10.7082	13.1118	2.1537

Table D.3: Filter design results. Synthetic astaxanthin concentration prediction using OLS and LOOCV, minimising RMSECV. All using 100,000 iterations. VML: VideometerLab.

Image Type	RMSE CV	Filter 1 nm	Filter 2 nm	Filter 3 nm
VML				
Scat	8.7	425.0–515.0	405.0–495.0	925.0–1015.0
Fill	14.0	925.0–1015.0	905.0–995.0	832.5–987.5
Specim				
Scat	27.6	1439.2–1489.6	1502.2–1641.0	2038.4–2088.8
Fill	22.7	1439.2–1489.6	1470.7–1634.7	1458.1–1634.7

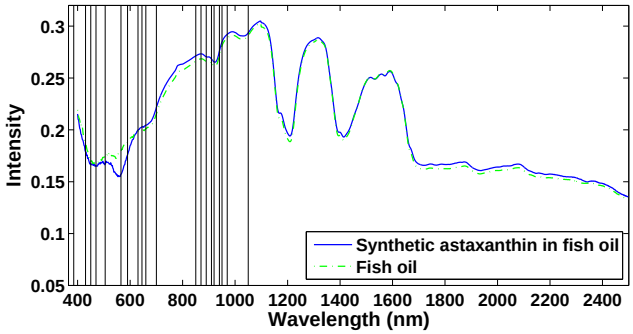

Figure D.1: Spectrometer reflection spectra of synthetic astaxanthin in fish oil, and plain fish oil. The values were converted from absorbance to reflectance. The wavelengths of the VideometerLab are marked by vertical lines.

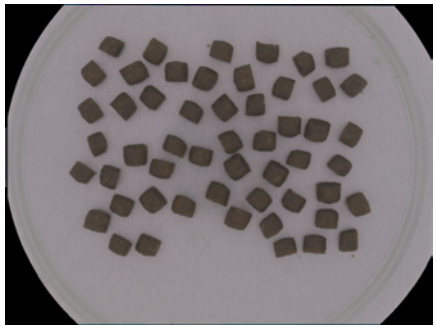

Figure D.2: Standard RGB version of a VideometerLab Scat image (scattered pellets lying on their side) of pellets with coating using fish oil with synthetic astaxanthin level of 20 ppm.

camera devices. Furthermore, the difference in results might be explained by the fact that the two methods use different parts of the spectrum. The type of light is also different between the VideometerLab and the Specim device. The Fill images using the Specim device contain more shadows than the Fill images using VideometerLab because of the direct lighting used for Specim and the diffuse light used in the VideometerLab sphere.

The scattering in Fill images could be different from the Scat images because the light penetrates one pellet in the Fill situation and could be scattered into other pellets so several pellets affect the result together.

The filter design method shows higher error than PLSR, but the advantage with

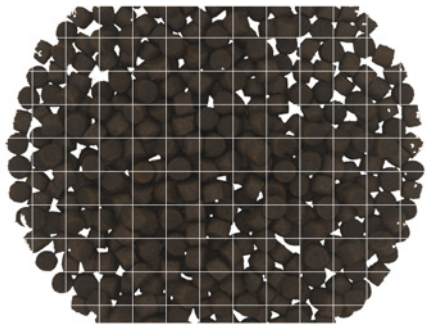

Figure D.3: Standard RGB version of a VideometerLab Fill image (a petri dish filled with pellets) of pellets with coating using fish oil with synthetic astaxanthin level of 20 ppm. The pellet cluster in the petri dish was segmented from the background and subregions of 100×100 pixels are visualised.

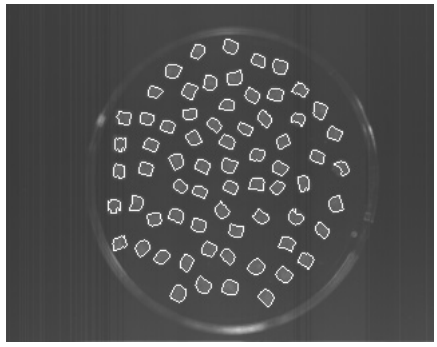

Figure D.4: Specim Scat image (scattered pellets lying on their side) of pellets with coating using fish oil with synthetic astaxanthin level of 20 ppm. The pellets were segmented from the background (white outline), and the intensity from the NIR spectral band of 1533.8 nm is used for visualisation.

the filter design method is that it can be implemented with optical filters, that are easier to implement than hyper-spectral imaging.

D.5 Conclusion

The results show that it is possible to predict the synthetic astaxanthin concentration in the coating using hyper-spectral image analysis.

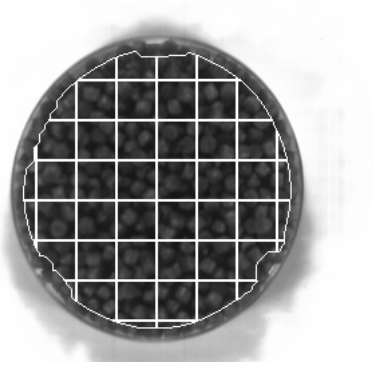

Figure D.5: Specim Fill image (a petri dish filled with pellets) of pellets with coating using fish oil with synthetic astaxanthin level of 20 ppm. Visualisation of the pellet cluster segmentation and subregions using 30×30 pixel regions. The intensity from the NIR spectral band of 1533.8 nm is used for visualisation.

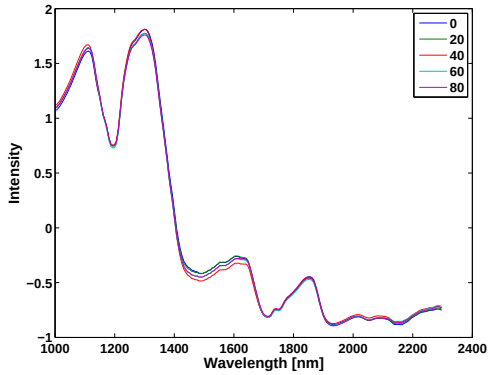

Figure D.6: Mean reflection spectra of the five different concentration levels of synthetic astaxanthin coating (ppm), using Specim Fill images (a petri dish filled with pellets) and SNV normalisation.

The results show that Scat is better than Fill for the VideometerLab images, but that Fill is better than Scat for the Specim images. Having said that, it must be emphasised that both Scat and Fill images show promising results and can be used for the inspection tasks.

Both PLSR and the filter design method put emphasis on the wavelengths found to be important for astaxanthin absorption/reflection, mostly between 1400 and 1600 nm. The prediction error for PLSR is lower than the error for the filter design results. However, the filters are easier to implement for industrial quality

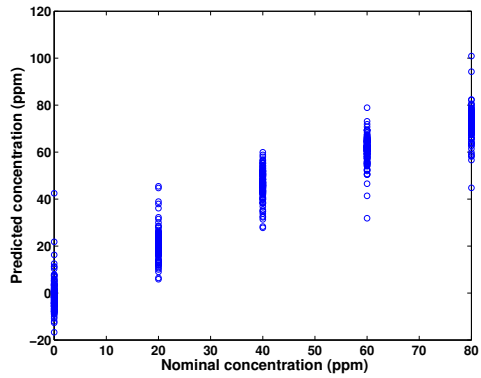

Figure D.7: PLSR prediction of synthetic astaxanthin coating concentration level (ppm) using the validation set of VideometerLab Fill images of pellets (a petri dish filled with pellets), and using 14 PLSR components.

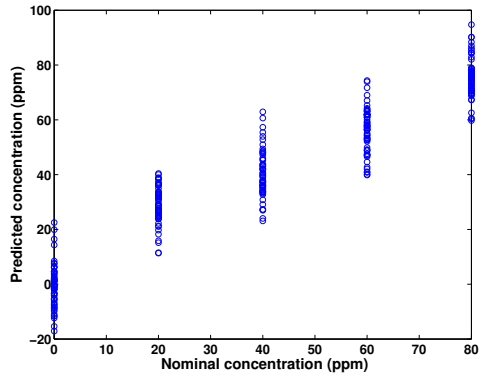

Figure D.8: PLSR prediction of synthetic astaxanthin coating concentration level (ppm) using the validation set of Specim Fill images of pellets (a petri dish filled with pellets), and using 24 PLSR components.

inspection.

Acknowledgment

The work presented has received funding from BioMar A/S and the EU under the Seventh Framework Programme FP7/2007-2013 under grant agreement number 214505.10.

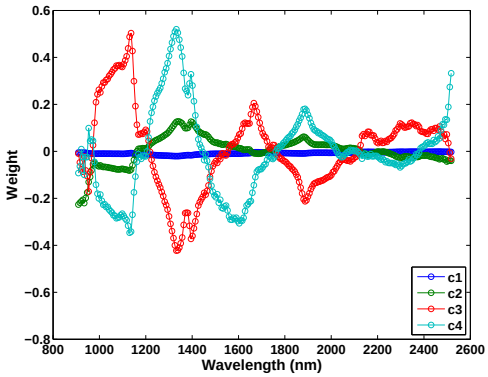

Figure D.9: PLSR components for the prediction of synthetic astaxanthin coating concentration level using Specim Fill images (a petri dish filled with pellets). Here showing the first four of the total 24 PLSR components.

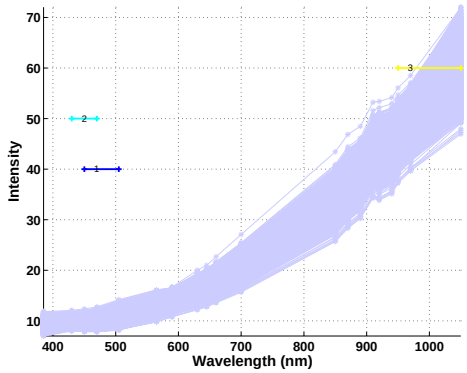

Figure D.10: Filter design results for prediction on VideometerLab Scat images (scattered pellets lying on their side) of pellets with synthetic astaxanthin coating concentration levels. The first two filters are selected in the visual range, and the third in the NIR regime. The filters are overlayed on all the reflection spectra of the data set.

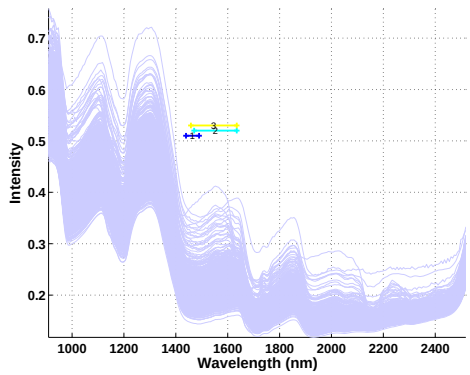

Figure D.11: Filter design results for prediction on Specim Fill images (a petri dish filled with pellets) of pellets with synthetic astaxanthin coating concentration levels. All three filters are selected in the NIR range of 1439-1634 nm. The filters are overlayed on all the reflection spectra of the data set.

Appendix E

Hyper-spectral Imaging based on Diffused Laser Light for Prediction of Astaxanthin Coating Concentration

---

Martin Georg Ljungqvist, Otto Højager Nielsen, Stina Frosch,

Michael Engelbrecht Nielsen, Line Harder Clemmensen, Bjarne Kjær Ersbøll

Submitted to Machine Vision and Applications 2012. Accepted for publication in 2013 [92].

Abstract

We present a study on predicting the concentration level of synthetic astaxanthin in fish feed pellet coating using multi- and hyper-spectral image analysis. This was done in parallel using two different vision systems. A new instrument for hyper-spectral imaging, the SuperK set-up, using a super-continuum laser as the light source was introduced. Furthermore, a parallel study with the commercially available multi-spectral VideometerLab imaging system was performed. The SuperK set-up used 113 spectral bands (455-1015 nm), and the VideometerLab used 20 spectral bands (385-1050 nm). In order to predict the astaxanthin concentration from the spectral image data, the synthetic astaxanthin content in the pellets was measured with the established standard technique; high pressure liquid chromatography (HPLC). Regression analysis was done using partial least squares regression (PLSR) and the sparse regression method elastic net (EN). The ratio of standard error of prediction (RPD) is the ratio between the standard deviation of the reference values and the prediction error, and for both PLSR and EN both devices gave RPD values between 4 and 24, and with mean prediction error of 1.4-8.0 parts per million (ppm) of astaxanthin concentration. The results show that it is possible to predict the synthetic astaxanthin concentration in the coating well enough for quality control using both multi- and hyper-spectral image analysis, while the SuperK set-up performs with higher accuracy than the VideometerLab device for this particular problem. The spectral resolution made it possible to identify the most significant spectral regions for detection of astaxanthin. The results also imply that the presented methods can be used in general for quality inspection of various coating substances using similar coating methods.

E.1 Introduction

Astaxanthin is a naturally occurring carotenoid with a high antioxidant activity essential for growth and survival and it is important for the development of colour in salmonid fishes [128]. The primary use of astaxanthin within aquaculture is as a feed additive to ensure that farmed salmon and trout have similar appearance to their wild counterparts [138]. The colour appearance of fish products is important for customers as a quality indicator [57, 108, 127]. Astaxanthin is very expensive [9] and therefore optimisation of its use in fish feed production is of importance.

Synthetic astaxanthin is more easily available and costs slightly less than natural astaxanthin and is therefore used more often in industry. However, there is a

demand for natural astaxanthin for the organic salmonid fish market, where natural astaxanthin is mandatory.

Today, chemical measurement of astaxanthin is done by high pressure liquid chromatography (HPLC). HPLC is a well established technique for measuring synthetic astaxanthin content in fish oil. However, when measuring astaxanthin concentration in fish feed pellets, an additional step for extraction of the oil is necessary, and this is why measurements of astaxanthin from fish feed pellets are less accurate and more labour intensive.

An automatic vision system for at-line pigment quality control of astaxanthin coating concentration level would be of great benefit to the industry, in relation to both process control and process optimisation.

The aim of this study is to investigate the possibility of predicting the concentration level of synthetic astaxanthin coating on aquaculture feed pellets by spectral imaging. Since HPLC is used for measuring astaxanthin coating content in the industry, we used this as a reference method.

Spectral imaging is called multi-spectral when using a small number of spectral bands (e.g. less than about 50), and hyper-spectral when using a large number of spectral bands (e.g. hundreds).

Previous studies on feed pellet monitoring by spectral analysis include near infra-red (NIR) reflectance spectroscopy for classification of feed material and feed pellets by Fernández-Ahumada et al. (2010) [44], and predicting chemical information in pharmaceutical pellet core and coating using NIR imaging by Sabin et al. (2011) [120].

Previous work on multi- and hyper-spectral image analysis of astaxanthin coating by Ljungqvist et al. (2012) [89, 90] has shown promising results for screening of the concentration level. However, those studies did not use hyper-spectral imaging in the visual part of the spectrum. In [90] only the NIR range was analysed, and in [89] only 20 wavelengths were analysed in the visual and parts of the NIR range. Neither of them used chemical measurements for validation of the astaxanthin coating level.

For the previous work using the visual part of the spectrum [89], the spectral bands were located at predefined wavelengths due to instrument set-up, chosen without knowledge of the particular problem. The few spectral bands used may not be the ones that give the greatest ability to quantify the contents of astaxanthin. Thus a more detailed study is called for, and here we report the characteristics for a new imaging method based on diffused laser light with more spectral bands. The study is focused on the visual region of the electromagnetic

spectrum due to function of astaxanthin as a pigment.

Vision systems have previously been implemented for quantisation of chemical contents, and a number of light-source options exist. In this paper we present the use of a super-continuum light source for full-field illumination. The super-continuum laser, combined with an acousto-optical tunable filter (AOTF) provides a broadband tunable light source. This form of light source is often used for confocal microscopy [121], fluorescence lifetime imaging [98], and measurement of sub-surface laser scattering (SLS) [104, 105]; also known as diffuse reflectance. To apply the light-source for full-field illumination, the small beam from the AOTF box is simply expanded and made diffuse.

A parallel study with a commercially available multi-spectral system called VideometerLab was also performed. The performance of this device has been validated for similar surface chemistry applications [30, 31, 32, 37, 39, 56, 62, 87].

Since the hyper-spectral imaging device records more spectral bands than a multi-spectral device, it would give more detailed information for measuring the astaxanthin coating concentration.

The presented work thus investigates both the possibility of examining astaxanthin contents by hyper-spectral image analysis, and a comparison of the two modalities (multi- and hyper-spectral imaging) for astaxanthin prediction.

E.2 Materials and Methods

E.2.1 Material

The pellets used in this study were produced for the purpose of this experiment, and the recipe was based on normal commercial fish feed for salmonid fish. The pellets had the approximate production diameter of 4.5 mm, and were coated with fish oil.

An extruder machine was used for the pellet production. The feed material was extruded through a die plate with holes of a specific diameter which determined the diameter of the pellets. On the other side of the disk there was a set of rotating knives that cut the material into shorter, cylinder-shaped pellets.

The synthetic astaxanthin used was cold water dispersible (BASF SE, Germany), and in total 7 different levels of synthetic astaxanthin concentration

were added to the fish oil coating. The highest synthetic astaxanthin level in fish oil was 100 parts per million (ppm), and then the oil was diluted so that the concentration level became half of the original. This was repeated to achieve the 7 nominal levels of synthetic astaxanthin concentration in the fish oil coating, where the last level was 0 ppm, see Table E.1.

Fish oil in itself typically contains a small amount of natural astaxanthin, however this is assumed to be less than 1 ppm and is here referred to as a coating of 0 ppm concentration. Astaxanthin is commonly measured in ppm, and it is measured in mass so here ppm corresponds to mg/kg.

Between production and image acquisition the pellets were stored at 2° Celsius in a dark environment for two months. They were stored in plastic bags where the oxygen had been pumped out and the bags were filled with nitrogen to minimise the oxidation process and quality reduction during storage.

The spectral reflection of the pellets is a mix of the pellet compound (recipe) and the reflection of astaxanthin. The light captured by each pixel is thus assumed to be a linear combination of two main components; the pellet compound and the astaxanthin coating. Due to the production method, the coating is neither evenly distributed among the pellets, nor uniformly on each pellet.

In the extrusion process, parts of the astaxanthin coating will go inside the pellet, while we only measure reflection from the surface. However, the industry is interested in the total amount of astaxanthin in the pellets. Therefore, the surface reflection is assumed to be linearly related to the total amount of astaxanthin in the pellets.

It is assumed that most of the quantity of synthetic astaxanthin on each pellet can be estimated by measuring the coating surface of each pellet. For practical use, however, it is not interesting to estimate the quantity on each single pellet, but rather on a larger amount of pellets and calculate an ensemble average.

E.2.2 Equipment

E.2.2.1 SuperK

The hyper-spectral imaging system consists of four parts: light source, spectral filter, diffuse filter and camera. The illumination system is based on a SuperK Extreme (NKT Photonics A/S, Denmark) super-continuum white light laser producing a quasi continuous output. The super-continuum light is filtered

Table E.1: Data overview of the 7 pellet groups (nominal concentration levels) and the number of images taken (of different samples) with VideometerLab and SuperK respectively. Added synthetic astaxanthin to the fish oil coating in ppm.

	Synthetic Astaxanthin Concentration (ppm)						
Levels	0	3.125	6.25	12.5	25	50	100
	Number of images						
VideometerLab	30	30	30	30	30	30	30
SuperK	10	10	10	10	10	10	10

using a SuperK Select (NKT Photonics A/S, Denmark), where an AOTF is used for spectral filtering of the beam. The combined light source and filtering box provides a wavelength tunable laser beam delivered in a photonic crystal fibre (PCF) by a Fiber Delivery System (NKT Photonics A/S, Denmark). The combined system provides 0.5 - 6.5 mW.

In combination this system provides light in the visual and NIR region, ranging from 455 to 1015 nm. A step size of 5 nm was used as the spectral resolution, resulting in 113 spectral bands. The bandwidth grows linearly as a function of wavelength; at 500 nm it is 3.5 nm, at 900 nm it is 14 nm.

The spectrally filtered light from the Fiber Delivery System forms a Gaussian fundamental transverse electromagnetic (TEM_{00}) beam. This is transformed to illuminate a square area below the camera using an Engineered Diffuser (ED1-C20-MD, Thorlabs, Sweden). This diffusing method has a high power transmission onto the sample.

The illumination does not form a perfectly uniform intensity distribution; it produces a gradient due to the projection caused by the oblique incidence of the beam onto the camera field of view. It also produces a short distance intensity fluctuation. To minimise the latter effect, the Gaussian beam delivered after the AOTF box is expanded using a -50 mm focal length negative lens (LC1439, Thorlabs, Sweden). By illuminating the Engineered Diffuser, the short distance intensity fluctuations are minimised and become insignificant for this application.

Image capturing is done using a Grasshopper GRAS-20S4M grey-scale charge-coupled device (CCD) camera (Point Grey Research Inc, Canada), which uses a 12 bit analogue to digital converter (ADC) with a 16 bit output. The image resolution is 1600 $\times$ 1200 pixels, with a pixel size of approximately 0.028 $\times$

0.028 millimetres. For an overview of the SuperK set-up see Figure E.1.

E.2.2.2 VideometerLab

To compare the result of the SuperK set-up, the commercially available multi-spectral VideometerLab (Videometer A/S, Hørsholm, Denmark) was also used for image acquisition. It uses 20 wavelengths distributed over the ultra-violet A (UVA), visual and NIR region: 385, 430, 450, 470, 505, 565, 590, 630, 645, 660, 700, 850, 870, 890, 910, 920, 940, 950, 970, 1050 nm.

This system uses a Point Grey Scorpion SCOR-20SOM grey-scale CCD camera. The objects of interest are placed inside an integrating sphere (Ulbricht sphere) with uniform diffuse lighting from light sources placed around the rim of the sphere [23]. All light sources are light-emitting diodes (LED) except for 1050 nm, which is a diffused laser diode.

The curvature of the sphere and its matt-white coating ensure a uniform diffuse light so that specular effects are avoided and the amount of shadow is minimised. The device is calibrated radiometrically with a following light and exposure calibration according to the National Institute of Standards and Technology (NIST). The system is also geometrically calibrated to ensure pixel correspondence for all spectral bands [48]. For an overview of the VideometerLab set-up see Figure E.2.

VideometerLab has the advantage that the intensity is calibrated with respect to the sensitivity of the CCD and the intensity of the light sources, which means that the resulting reflection spectrum can be compared with e.g. a spectroscopy spectrum.

The image resolution is 1200×1200 pixels. In this situation one pixel represents approximately 0.072×0.072 millimetres. The Scorpion camera has a 12 bit ADC, and the system uses 8 bit data output from the camera. After calibration correction, the reflectance intensity is output at 32 bit precision.

E.2.2.3 Spectroscopy

In order to explore the spectral properties of astaxanthin further, and to assist in the interpretation of the spectral image results, a spectrometer was used in the visual and NIR range. Absorption spectra of synthetic astaxanthin in a solution of fish oil along with plain fish oil were recorded using a NIRSystems 6500

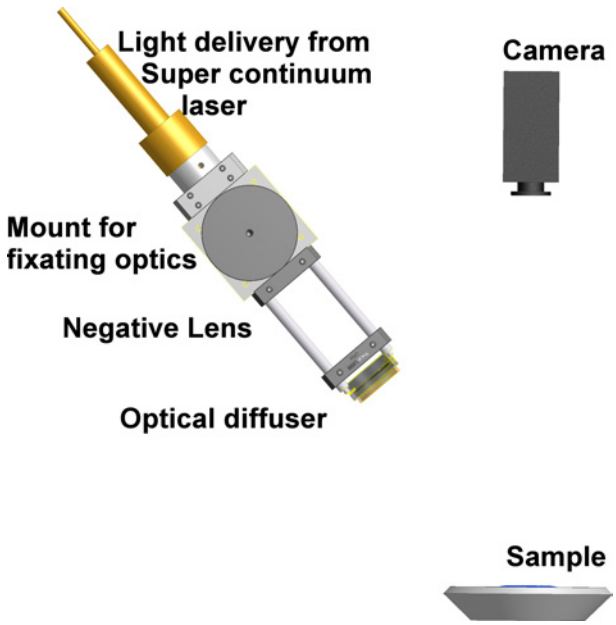

Figure E.1: Overview of the SuperK set-up showing the supercontinuum light delivery, negative lens, optical diffuser, camera, and sample position.

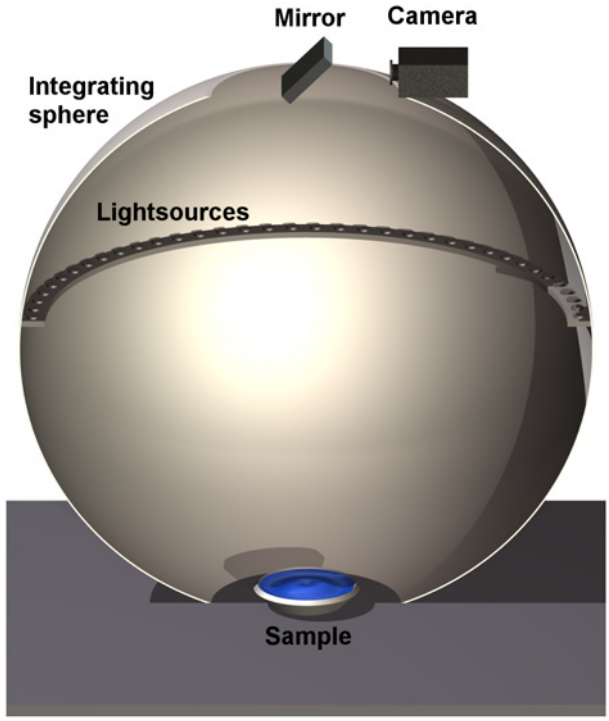

Figure E.2: The VideometerLab set-up showing a cross section of the integrating sphere, light sources, camera, and sample position.

absorption spectrometer (Foss NIRSystems Inc, USA) with a spectral resolution of 2 nm. The absorption spectra were transformed to reflection values using the standard relation $A = -\log(R)$, where A is the absorption values and R is the reflection values.

E.2.2.4 High Pressure Liquid Chromatography

In order to calibrate the hyper-spectral imaging prediction method, an HPLC analysis of the synthetic astaxanthin concentration in pellets was performed. By analysing samples from each concentration level we could estimate the average astaxanthin content in the pellets, which can be used to validate the nominal levels used in the production. In order to reduce the effect of the analysis method, we used two independent HPLC measurements from different parties.

The HPLC analysis was done at the National Food Institute, Division of Industrial Food Research at the Technical University of Denmark (Lyngby, Denmark) using an Agilent 1100 series HPLC (Agilent Technologies, Palo Alto, CA, USA), equipped with a UV diode array detector. The oil was extracted from the pellets using acetone and homogenised to a concentrate, which was analysed for synthetic astaxanthin content, according to the modified protocol of Bligh and Dyer (1959) [16].

A fraction of the lipid extract was evaporated under nitrogen and redissolved in 2 mL of *n*-heptane before injection. Astaxanthin content was determined after injection of an aliquot (50 μL) of the *n*-heptane fraction into a LiChrosorb Si60-5 column (100 mm $\times$ 3 mm, 5 μm) equipped with a Cromsep Silica (S2) guard column (10 mm $\times$ 2 mm; Chrompack, Middelburg, The Netherlands) and eluted with a flow of 1.2 mL/min using *n*-heptane/acetone (86:14, v/v) and detection at 470 nm. Concentrations of astaxanthin were calculated using authentic standards from Dr. Ehrenstorfer GmbH (Augsburg, Germany).

Furthermore, HPLC analysis was also made at Eurofins A/S (Galten, Denmark), which is a commercial laboratory.

E.2.3 Image Acquisition

Images of petri dishes (plastic, diameter of 9 cm) filled with pellets were captured using both the SuperK set-up and the VideometerLab. For each concentration level, 10 images of different pellets were captured using both SuperK and

VideometerLab, then an additional 20 images were captured with VideometerLab, see Table E.1. In total 70 SuperK pellet images and 210 VideometerLab pellet images were captured over two consecutive days.

The concentration level sequence was randomised, and samples were interleaved two at a time. The pellets were at normal room temperature during image acquisition.

A filled petri dish resembles the rapid inspection that the industry would desire for this application.

The pellet cluster inside the petri dish in each image was segmented from the light-grey background using a grey-scale threshold, using the band of 500 nm for the SuperK images and the band of 470 nm for the VideometerLab images. The threshold segmentation was complemented with the morphological methods erosion and dilation using a disk as structuring element [122]. Furthermore, the topmost layer of pellets was segmented to remove parts with less light, and in this way also avoid some of the granulometry information in the image. Since the SuperK images contained some specular reflections due to the direct lighting, the strongest specular effects were also removed by a threshold for both the VideometerLab and SuperK images.

The mean spectrum of the pixels in each segmented image was used as samples. In this way the impact of the pattern from the diffuse filter used by the SuperK set-up was reduced and was assumed not to impact the results of the image analysis.

Standard red-green-blue (sRGB) colour image representations of the VideometerLab images for this paper were done by multi-spectral colour-mapping using penalised least square regression described in Dissing et al. (2010) [36]. Since the SuperK set-up is not calibrated towards the CCD, sensitivity standardised colour-mapping was not possible, instead non-standard RGB images were made in order to visualise the images.

E.2.4 Data Analysis

The number of samples is denoted n and the number of variables (the wavelengths) is denoted p. The stored data of n samples and p variables is denoted as matrix $\mathbf{X}$. The ground truth reference values (concentration level) are stored in vector $\mathbf{y}$ with length n. The predicted (estimated) value of $\mathbf{y}$ is denoted $\hat{\mathbf{y}}$.

For ground truth reference values, the nominal values in Table E.1 were used.

For the VideometerLab data p is 20 and n is 210. In order to compare the VideometerLab data with the SuperK data, the 70 images corresponding to the same petri dishes of pellets for both methods were used in the analyses; $n = 70$. For the SuperK data p is 113 and n is 70, this results in an ill-posed problem with more variables than observations ($p \gg n$).

Two different regression methods were used in order to estimate the concentration level of synthetic astaxanthin in the pellet coating. Both methods produce linear prediction models, but they calculate the models in different ways, as described below.

All image analyses and statistics were carried out using Matlab 7.9 (The Mathworks Inc., Natick, MA, USA).

E.2.4.1 Principal Component Analysis

The multivariate data from the images were analysed using principal component analysis (PCA) for exploratory purposes [53]. PCA is an unsupervised method, and the most optimal method with respect to maximising the variance in the data [63]. If the relation of interest contains large variations, then PCA is a good method for analysing the data. The pre-processing method, called standard normal variate (SNV) [117], was used, followed by PCA. SNV is performed by subtracting the mean from each sample, and normalising using the standard deviation (SD) of the sample spectrum.

E.2.4.2 Model Selection and Validation

In order to calibrate the statistical model parameters, a calibration set of 70% of the samples was used (n_c). Then the chosen model was validated on the remaining 30% of the samples (n_v). For the VideometerLab data with a total of 210 samples, $n_c = 147$ and $n_v = 63$, and for the VideometerLab data using 70 samples, $n_c = 49$ and $n_v = 21$. For the SuperK data with a total of 70 samples, $n_c = 49$ and $n_v = 21$.

The calibration and validation set was chosen randomly, but with all concentration levels present in both. The same corresponding samples for both devices were present in both the calibration and the validation set.

For parameter calibration two different methods were used in parallel. Firstly, the leave-one-out cross-validation (LOOCV) method was used on the calibration

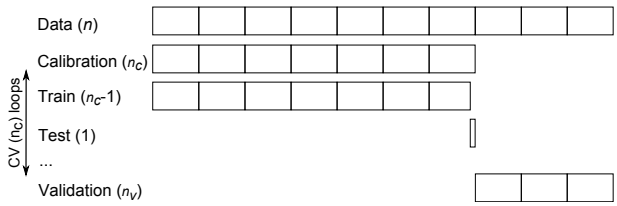

Figure E.3: Schematic overview of the LOOCV used for calibration and validation of the prediction. The calibration set consists of n_c samples, and the validation set of n_v samples. One sample at a time is left out for test in the calibration step.

set, where each sample is used as validation once, see Figure E.3.

Secondly, what can be called a group-fold cross-validation (GFCV) was used both for parameter calibration and in order to investigate how the prediction generalises on unseen concentration levels. The GFCV was performed so that all samples with one concentration level, a group, was left out during training of the model, and then the left out group was used for prediction.

Two nested GFCV:s were used, one for calibrating a PLSR model, and one for the final validation and generalisation. For every iteration a PLSR model was calibrated using GFCV on 6 levels, and then the validation was done on the left out level. For each iteration one of the 5 middle levels (3.125, 6.25, 12.5, 25, 50 ppm) were left out at a time in order to see how a model predicts on an unseen concentration level. The highest and lowest concentration levels were not used for the validation/generalisation part since we are not interested in extrapolation of the model. This procedure renders a result in terms of a pooled prediction error of the 5 group tests. For an overview of the GFCV scheme see Figure E.4.

E.2.4.3 Partial Least Squares Regression

The first method for analysing the concentration level was the partial least squares regression (PLSR) method [63, 131]. The data was mean centred, and the number of components to be used in the PLSR model was decided using LOOCV, and likewise GFCV, on the calibration set while minimising the mean of the residual sum of squares (RSS), see Equation E.1. A modified version of the 'one standard error rule' [63] for selection was used: The least number of components with RSS value inside the range of two SDs of the lowest value of RSS was selected.

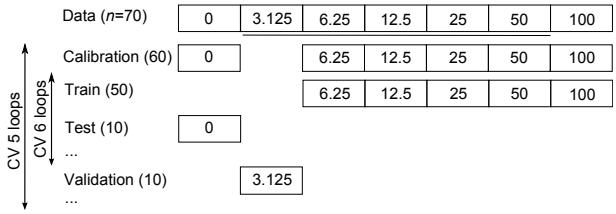

Figure E.4: Schematic overview of the group oriented cross-validation GFCV for calibration and validation of the prediction. The GFCV is used both for calibration and for generalisation validation. The data contains 7 different concentration levels, groups, and the middle 5 of these are used for generalisation validation. Each group consists of 10 samples. Calibration is performed on 6 groups at a time. One group at a time is left out for validation. Synthetic astaxanthin concentration in ppm.

For the VideometerLab data, the number of components (factors) n_f tested in the calibration step was varied from 1 to 20. For the SuperK data containing 113 variables and a calibration set of 49 samples; 47 was used as the maximum number of components tested.

The chosen value of n_f was used on the calibration set and the resulting prediction model was then validated on the validation set.

The coefficient of determination R^2 is a measure of how much variation is explained by the model and was calculated for the prediction of the validation set. R^2 is basically the ratio of the RSS and the total sum of squares (TSS), see Equation E.1.

$$R^2 = 1 - \frac{RSS}{TSS} = 1 - \frac{\sum_{n_v}(\mathbf{y} - \hat{\mathbf{y}})^2}{\sum_{n_v}(\mathbf{y} - \frac{1}{n_v}\sum_{n_v}\mathbf{y})^2} \,. \tag{E.1}$$

Furthermore, the ratio of the standard error of prediction and standard deviation (RPD) was calculated as a measure of how well the model predicts. The RPD is the ratio between the SD of the original data $\mathbf{y}$ (the reference values) and the standard error of prediction (SEP), see Equations E.2 and E.3.

$$SEP = RMSEP = \sqrt{\frac{1}{n_v}\sum_{n_v}(\mathbf{y} - \hat{\mathbf{y}})^2} \,. \tag{E.2}$$

$$RPD = \frac{SD}{SEP}\,. \tag{E.3}$$

The SEP is equal to the root mean square error of prediction (RMSEP). An RPD value of 1.0 means that the model cannot predict accurately, since this means that the mean error is equal to the SD of the reference values. An RPD value higher than 2.5 is considered satisfactory for screening, and values of 5–10 are adequate for quality control [147].

To further see what range of the spectrum is relevant for the prediction of astaxanthin concentration, we used interval PLS (iPLS) regression where the spectrum is divided into a number of regions and PLSR is performed on each region individually [106]. While the VideometerLab data has too few spectral bands for this method, we can investigate what parts of the SuperK spectrum give best prediction. We used 20 intervals and a PLSR model was calibrated for each of them.

E.2.4.4 Elastic Net Regression

In order to identify which wavelengths are of most interest, the elastic net (EN) was also used for regression analysis [160]. The EN is a sparse statistical method and performs variable selection while doing regression. In contrast to PLSR it does not use linear combinations of all variables, it uses only a few variables which are found important; non-zero coefficients. In this way EN excludes variables that do not contribute to the result and thus are potential noise.

EN tends to select variables that are correlated with each other, and this is suitable for spectral data with intrinsic correlation. This grouping effect would make the result suitable for an optical filter implementation.

EN needs two model parameters: λ_1 for the L_1 norm for determining the number of non-zero coefficients, and λ_2 for the Euclidean L_2 norm for regularisation. The regularisation is suitable for the ill-posed problem. The regression model consists of the variable weights (coefficients) in $\boldsymbol{\beta}^{en}$, see Equation E.4.

$$\beta_j^{en} = \underset{\beta_j}{\operatorname{argmin}}\big(\|\mathbf{y} - \mathbf{X}\beta_j\|_2^2 + \lambda_2\|\beta_j\|_2^2 + \lambda_1\|\beta_j\|_1\big)\,. \tag{E.4}$$

The estimated coefficients are then multiplied by $(1 + \lambda_2)$ to get the final EN solution.

The two parameters were selected using LOOCV on the calibration set. The λ_1 parameter steers the selection of variables and was calculated so that the number of selected variables was varied from 1 to 20. The λ_2 parameter was varied with 12 logarithmic steps from 10^{-7} to 10. The data matrix $\mathbf{X}$ was normalised, and the reference values $\mathbf{y}$ were centred, for each calculation of the EN.

RSS was used in order to find the optimal parameter set. If more than one combination of the number of selected variables and λ_2 was found to give the best calibration result, then the lowest number of selected variables and the highest value of λ_2 was used, giving the least complex model.

The implementation by Sjöstrand et al. (2012) [130] was used for calculations of the EN.

E.3 Results

E.3.1 SuperK Power Stabilisation

To estimate the acquisition reproducibility, the same sample was repeatedly imaged for ~ 11 hours, and the mean image intensity was measured. To compare across wavelengths, we report the variation relative to the mean intensity of the given wavelength; the ratio denoted as a percentage (%). The resulting SDs are presented in Figure E.5 showing the image acquisition reproducibility.

Compared to the precision that is desired in estimating astaxanthin coating concentration (~ 1 %), we suspect that the wavelengths below 470 nm will be too noisy for modelling the concentration level. For the regression models this will automatically mean a reduced weighting for these bands.

Depending on which wavelength is chosen during modelling, and since we only apply linear models, the reported SD as a function of wavelength indicates the precision of ~ 0.3 % as a limit of the acquisition process itself.

E.3.2 Chemical Measurement

The results from the two independent HPLC measurements of the synthetic astaxanthin coating concentration both show lower values than the nominal values, and DTU shows lower values than Eurofins. However, both HPLC mea-

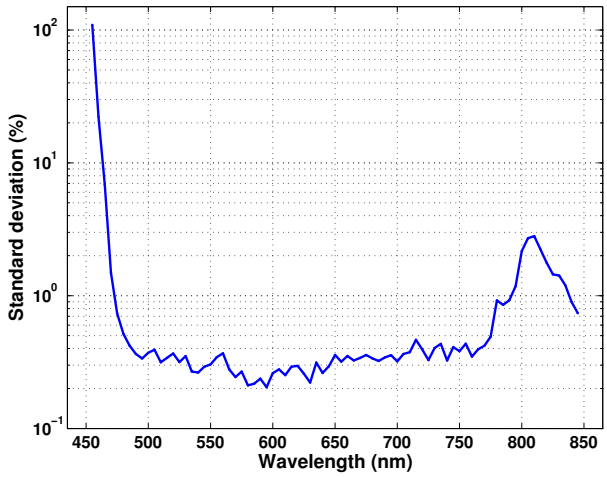

Figure E.5: SuperK stability measurement. Standard deviation of the mean image intensities (%) of the power-normalised image data for each wavelength.

surements are linear to the nominal values, see Table E.2, which means that the nominal values are valid as reference values for the regression.

E.3.3 Image Analysis

Background and dark sample parts were segmented out using threshold and morphological operations. Example results of a segmented VideometerLab image can be seen in Figures E.6 and E.7, as well as for SuperK in Figures E.8 and E.9. RGB versions of the captured images for all 7 concentration levels visualising the differences in pigment concentration can be seen in Figure E.10 for VideometerLab, and in Figure E.11 for the SuperK images.

The spectrometer spectra of fish oil with added synthetic astaxanthin and plain fish oil are presented in Figure E.12, which shows that the largest separation is in the range of 490 – 610 nm.

Investigating the reflection spectra of the pellets coated with synthetic astaxanthin shows similar characteristics to the spectroscopy results of astaxanthin in fish oil, see Figure E.13. Looking at the difference of the concentration levels' reflection spectra in Figures E.14 and E.15 reveals that the largest difference between concentration levels is around 505 nm for the VideometerLab data, and between 500 and 520 nm for the SuperK data. This corresponds well with

regions of difference in the reflection spectrum in Figure E.12.

From the explorative analysis of the concentration level of synthetic astaxanthin coating using PCA, score scatter plots using all combinations of PC1 to PC6 were investigated (results not shown). PC2 seems to describe the concentration scale well for the SuperK data, and PC2 in combination with PC3 for the VideometerLab data. However, both show some small overlap – mostly for the lower concentration levels, see Figures E.16 and E.17. This concludes that the variation between the concentration levels is the second largest variance in the image data (PC2), next after the total intensity variation (PC1), which corresponds well with the two spectra mentioned above.

Calibrating the PLSR model by LOOCV gives an optimum of 3 components for the VideometerLab data, and 7 components for the SuperK data, see Figure E.18. It also shows that the calibration error drops significantly around 3 components for both modalities.

Regression analysis of the synthetic astaxanthin coating concentration level using the whole images as samples shows good results. PLSR using LOOCV shows an R^2 value of prediction above 0.94 for VideometerLab and 0.99 for SuperK, see Table E.3, where VideometerLab uses 3 PLSR components and SuperK uses 7 PLSR components.The EN using LOOCV has R^2 around 0.97 for VideometerLab and 0.99 for SuperK, see Table E.3, where the VideometerLab data uses 8 non-zero coefficients, and the SuperK data uses 19 coefficients.

For the VideometerLab data the RPD is between 4 and 9 for both PLSR and EN, while for the SuperK data the RPD value is almost 24 for PLSR and 21 for the EN. The mean prediction error is 7.6 ppm for VideometerLab using 210 samples, and 8.0 ppm when using 70 samples. For the SuperK data using 70 samples the mean prediction error is 1.4 ppm. The synthetic astaxanthin coating concentration prediction using PLSR and EN can be seen in Figures E.19 and E.20, and using EN in Figures E.21 and E.22, illustrating that the predicted levels correlate well with the nominal levels. For the SuperK data 3 PLSR components were also tested, resulting in an R^2 of 0.97, SEP of 3.8, and an RPD of 9, see Table E.3.

The RPD for different numbers of PLSR components can be seen in Figure E.23, where it shows that RPD above 5 is achieved for SuperK using only 2 components, and using 4 components for VideometerLab.

The PLSR components' weights show the contribution of different spectral regions to the model, and thus their significance. Similar to the difference from the grand mean, Figures E.14 and E.15, we rediscover the importance of the blue and green regime between 450 and 590 nm, but see distinctions also in the

NIR measurements for the two instruments, see Figures E.24 and E.25. For the VideometerLab data the largest PLSR weights are at 385 nm and 505 nm, while for the SuperK data the largest PLSR weights are around 550 nm and around 860 nm. The importance of the visual range of the spectrum was confirmed by the iPLS regression of the SuperK data returning the lowest LOOCV calibration error around 545 – 575 nm, see Figure E.26.

The EN regression coefficients $\boldsymbol{\beta}_{en}$ that constitute the prediction model show similar results for both VideometerLab and SuperK data, see Figures E.27 and E.30. For the VideometerLab data the largest coefficient is at 565 nm, and the second largest at 505 nm. For the SuperK data the largest coefficient is at 550 nm. Both systems show similar clusters of spectral bands with high emphasis in the visual regime.

The results also show that using the 16 bands that are the same for both the VideometerLab and the SuperK set-up (470, 505, 565, 590, 630, 645, 660, 700, 850, 870, 890, 910, 920, 940, 950, 970 nm) gives acceptable results for quality control with an RPD value of 2.6 for VideometerLab, and 8.3 for SuperK. The VideometerLab images got R^2 of 0.84 using 2 PLSR components, and the SuperK images got R^2 of 0.94 using 4 PLSR components, see Table E.3.

By leaving out one concentration level for validation using GFCV and PLSR, it was tested how the prediction performs on unseen concentration levels. Using LOOCV, all concentration levels have been used for calibration by leaving out one sample at a time, and for comparison with GFCV here 0 and 100 ppm have been left out when performing the validation. When using GFCV all concentration levels have been used for calibration while leaving out one concentration level at a time, and all concentration levels but 0 and 100 ppm have been used for validation, one at a time. We see that the pooled SEP of GFCV is larger than the corresponding SEP of LOOCV for both systems, as can be seen in Table E.4. For the VideometerLab using LOOCV, the SEP is 5.5, and for GFCV the pooled SEP is 14. For the SuperK data using LOOCV, the SEP is 1.3, and for GFCV the pooled SEP is 9.6.

Visualisation of the spatial distribution of synthetic astaxanthin coating on the pellets was done using the PLSR prediction result for VideometerLab and SuperK, and can be seen in Figures E.28 and E.29. Spectral images from the validation set and all different concentration levels have been projected using the PLSR components. This should only be seen as a visualisation, since the PLSR models are calibrated on image mean values and then used for prediction on pixel values. The visualisations clearly show larger values for the higher concentration levels of synthetic astaxanthin.

Table E.2: HPLC measurement of the synthetic astaxanthin present in the pellets, carried out by two different parties. Added synthetic astaxanthin to the fish oil coating in ppm.

Nominal Values	HPLC DTU	HPLC Eurofins
0	0	0
3.125	1.90	3.07
6.25	4.36	5.88
12.5	9.56	11.6
25	19.44	24.8
50	42.64	49.3
100	90.46	95.1

Table E.3: PLS and EN regression for synthetic astaxanthin coating concentration level prediction using LOOCV. PLS regression was also done using only the 16 bands that are in common for VideometerLab and SuperK. Synthetic astaxanthin concentration in ppm.

Device Samples (n)	Method	Comp. Coef.	R^2 Calibr.	R^2 Pred.	SEC Calibr.	SEP Pred.	RPD Pred.
VideometerLab							
210	PLS	3	0.9483	0.9479	7.6916	7.6180	9.1292
70	PLS	3	0.9598	0.9421	6.9785	8.0281	4.2588
210	EN	8	0.9729	0.9728	5.4904	5.5053	6.1094
70	EN	8	0.9853	0.9702	4.0426	5.7571	5.9387
SuperK							
70	PLS	7	0.9990	0.9982	1.1345	1.4278	23.9466
70	PLS	3	0.9788	0.9872	5.0698	3.7728	9.0622
70	EN	19	0.9989	0.9976	1.1093	1.6209	21.0926
VideometerLab-16							
70	PLS	2	0.8441	0.8432	13.5960	13.2122	2.5877
SuperK-16							
70	PLS	4	0.9850	0.9848	4.3091	4.1108	8.3170

Table E.4: Generalisation test with GFCV using PLS regression for synthetic astaxanthin coating concentration level prediction. The pooled SEP of GFCV is compared to the corresponding prediction error of LOOCV, where only the middle concentration levels (3.125, 6.25, 12.5, 25, 50 ppm) have been used for validation for both methods. The mean number of PLSR components used for GFCV is presented. Synthetic astaxanthin concentration in ppm.

Device	CV Type	Samples n	Comp. n_f	SEP Pred.
VideometerLab				
	LOOCV	70	3	5.4971
	GFCV	70	2	14.0364
SuperK				
	LOOCV	70	7	1.3240
	GFCV	70	1.6	9.5813

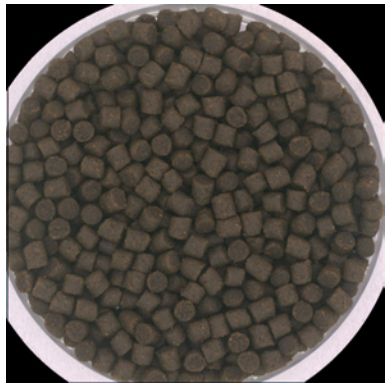

Figure E.6: SRGB representation of a VideometerLab image of pellets coated with synthetic astaxanthin of 50 ppm.

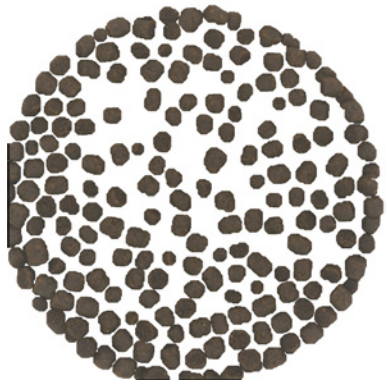

Figure E.7: SRGB representation of the segmented version of the VideometerLab image in Figure E.6, with pellets coated with synthetic astaxanthin of 50 ppm.

Figure E.8: RGB representation of a SuperK image of pellets coated with synthetic astaxanthin of 50 ppm.

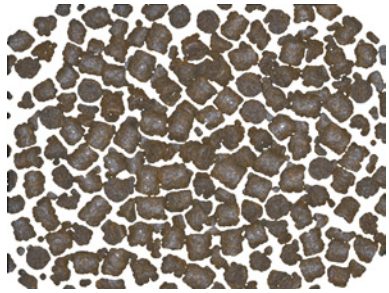

Figure E.9: RGB representation of the segmented version of the SuperK image in Figure E.8, with pellets coated with synthetic astaxanthin of 50 ppm.

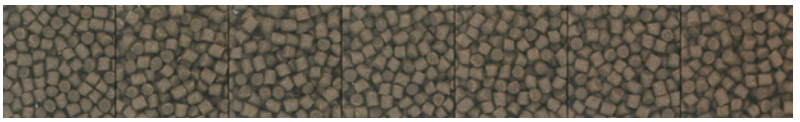

Figure E.10: SRGB representation of cropped VideometerLab images of the pellets with 7 different levels of synthetic astaxanthin coating concentration. From left to right: 0, 3.125, 6.25, 12.5, 25, 50, 100 ppm.

Figure E.11: RGB representation of cropped SuperK images of the pellets with 7 different levels of synthetic astaxanthin coating concentration. From left to right: 0, 3.125, 6.25, 12.5, 25, 50, 100 ppm.

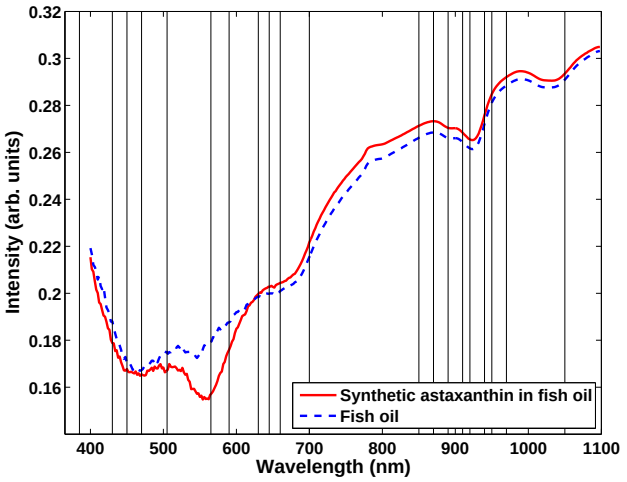

Figure E.12: Mean reflection spectra of synthetic astaxanthin coating in fish oil, as well as plain fish oil, using a spectrometer. No pellets were used here. The bands of the VideometerLab are marked by vertical lines.

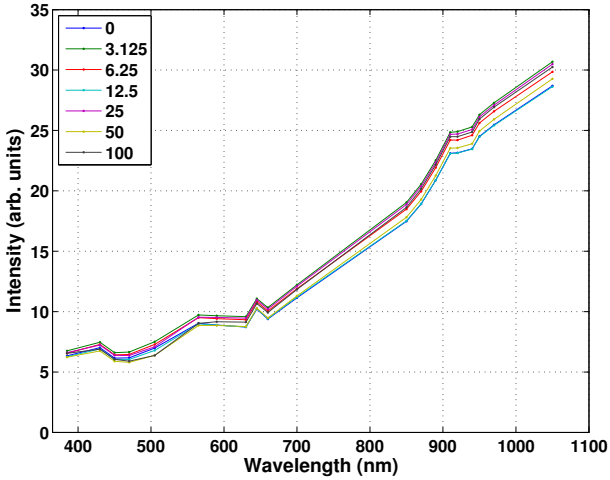

Figure E.13: Mean reflection spectra of the different concentration levels of synthetic astaxanthin in pellet coating, using image mean of the VideometerLab images, $n = 70$.

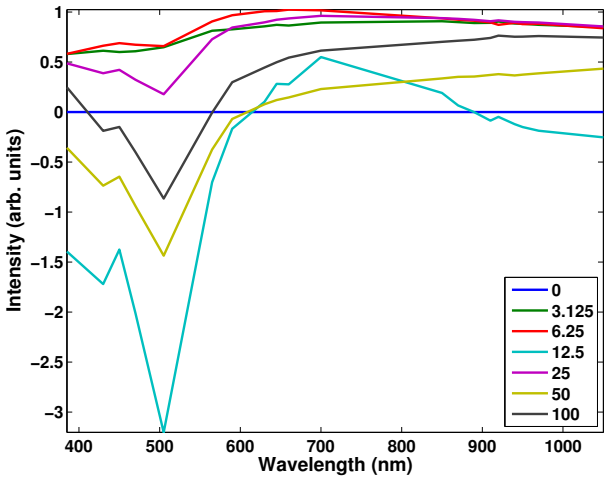

Figure E.14: The difference in reflection spectra from the concentration level of 0 ppm of the different concentration levels of synthetic astaxanthin coating, using the VideometerLab images, $n = 70$. Normalised by the SD of each level.

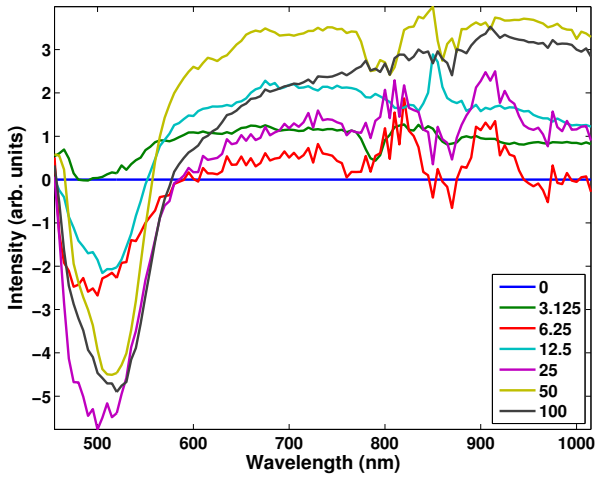

Figure E.15: The difference in reflection spectra from the concentration level of 0 ppm of the different concentration levels of synthetic astaxanthin coating, using the SuperK set-up, $n = 70$. Normalised by the SD of each level.

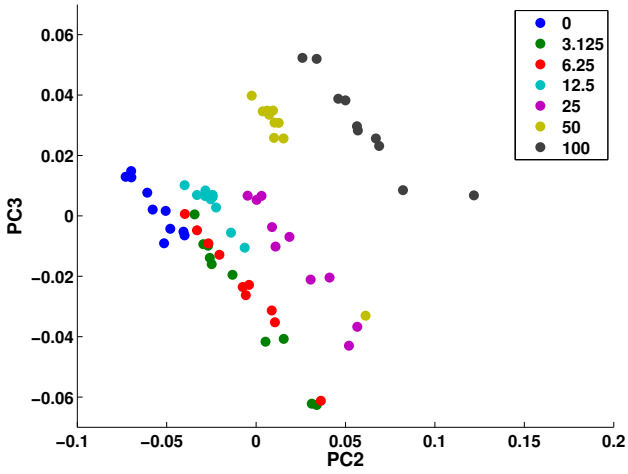

Figure E.16: Scatter plot of synthetic astaxanthin coating using PC2 and PC3 from a PCA on whole image samples using the VideometerLab, $n = 70$.

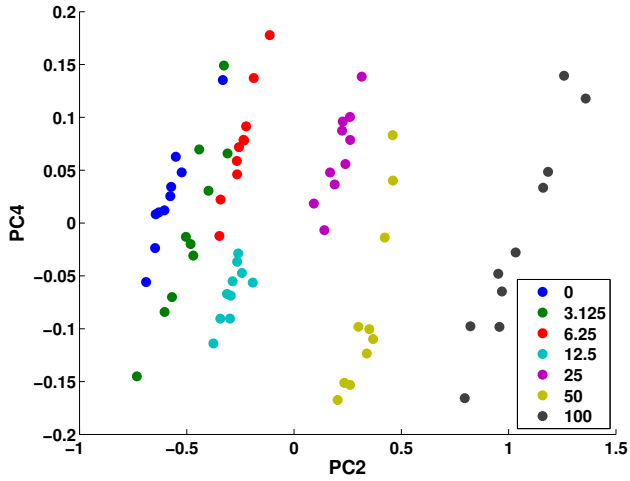

Figure E.17: Scatter plot of synthetic astaxanthin coating using PC2 and PC4 from a PCA on whole image samples using the SuperK, $n = 70$.

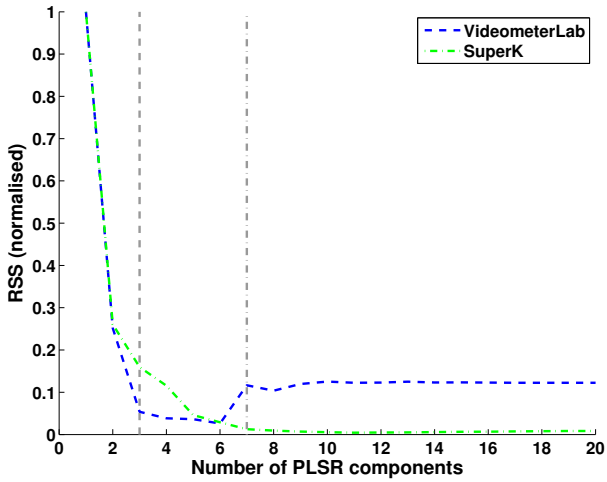

Figure E.18: PLSR calibration using LOOCV RSS, using the calibration data set of VideometerLab and SuperK respectively, $n_c = 49$, $n = 70$. Minimum of RSS with the least number of components within two SD was found at 3 components for VideometerLab, and at 7 components for SuperK. The first 20 components are shown for SuperK.

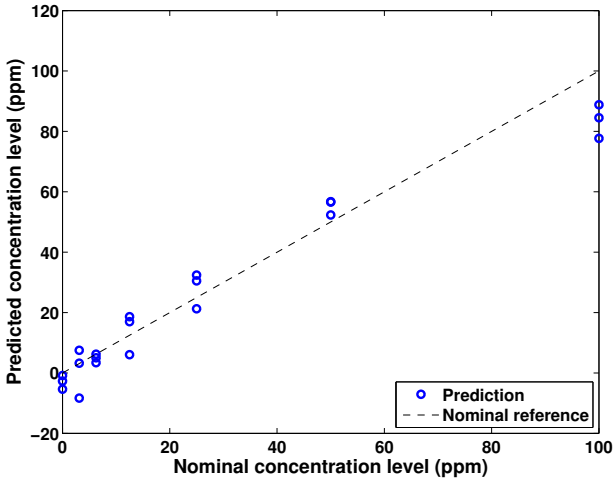

Figure E.19: PLSR prediction of synthetic astaxanthin coating using LOOCV on image samples from the VideometerLab, $n = 70$ and using 3 components.

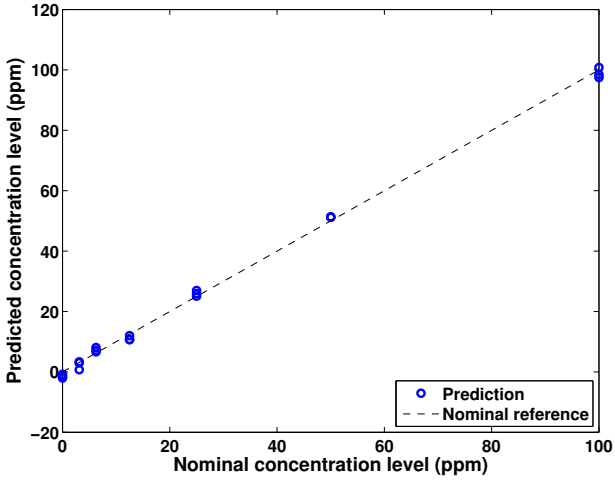

Figure E.20: PLSR prediction of synthetic astaxanthin coating using LOOCV on image samples from the SuperK, $n = 70$ and using 7 components.

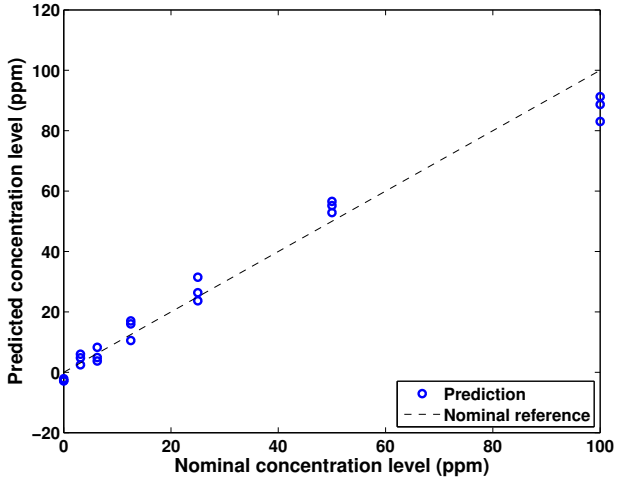

Figure E.21: EN prediction of synthetic astaxanthin coating using LOOCV on image samples from the VideometerLab, $n = 70$ and using 8 non-zero coefficients.

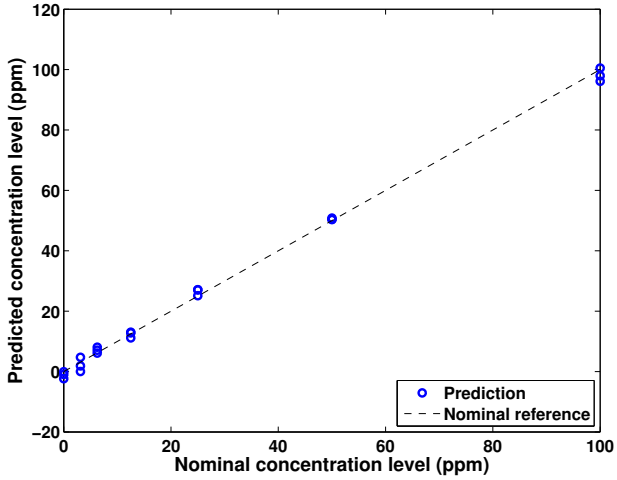

Figure E.22: EN prediction of synthetic astaxanthin coating using LOOCV on image samples from the SuperK, $n = 70$ and using 19 non-zero coefficients.

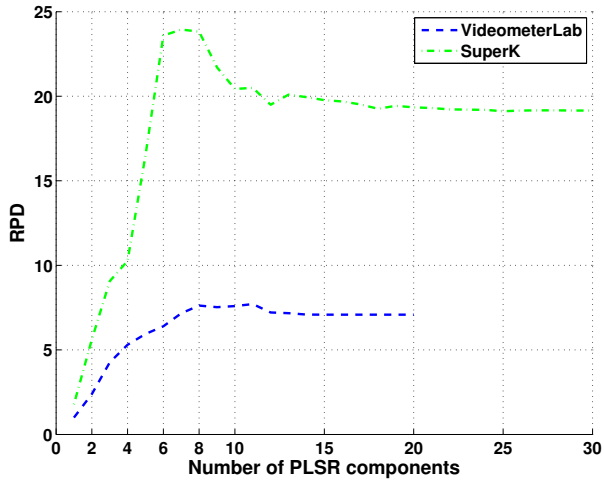

Figure E.23: RPD for different numbers of PLSR components. Using the calibration and validation data set of VideometerLab and SuperK respectively, $n = 70$. The first 30 components are shown for SuperK.

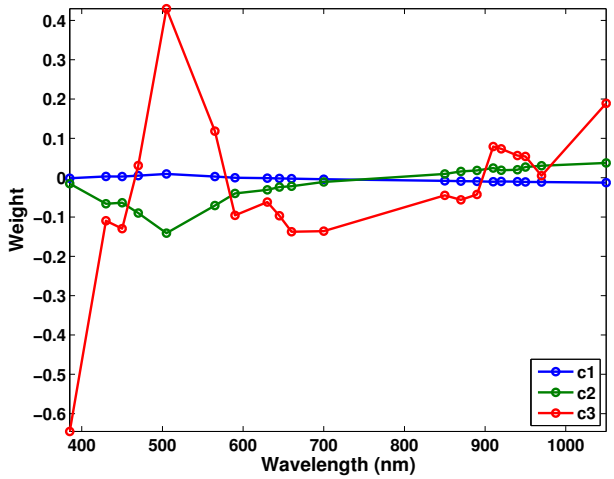

Figure E.24: PLSR components for the prediction of synthetic astaxanthin coating concentration level using LOOCV on image samples from the VideometerLab, $n_c = 49$, $n = 70$. Calculated on the calibration set, showing the 3 PLSR components.

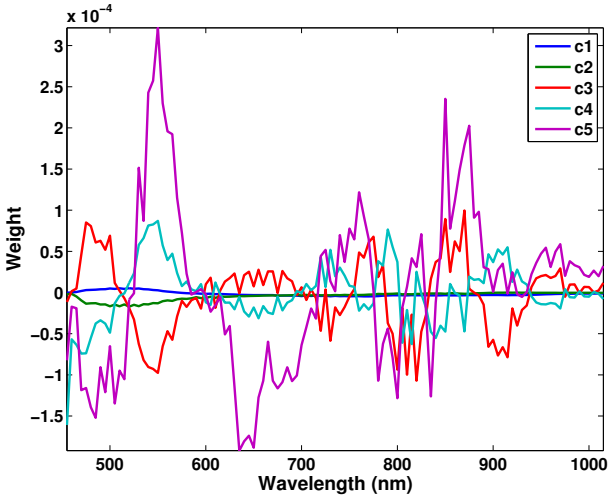

Figure E.25: PLSR components for the prediction of synthetic astaxanthin coating concentration level using LOOCV on image samples from the SuperK, $n_c = 49$, $n = 70$. Calculated on the calibration set, here showing the first 5 of the total 7 PLSR components.

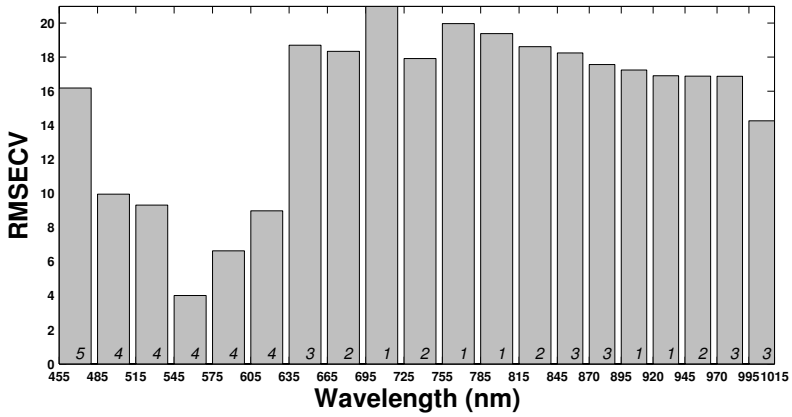

Figure E.26: The iPLS regression calibration using LOOCV on SuperK images illustrating the error (RMSECV) of 20 different regions in the spectrum, $n_c = 49$, $n = 70$. The optimal number of PLSR components chosen for each interval is shown in italics.

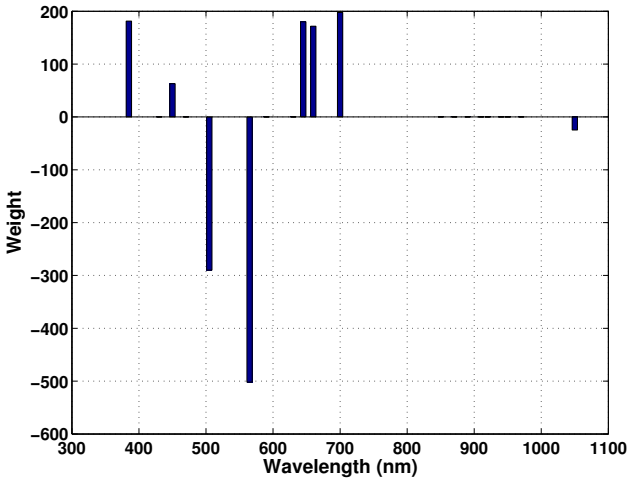

Figure E.27: The coefficients in $\boldsymbol{\beta}_{en}$ from the prediction model of synthetic astaxanthin coating using EN regression with LOOCV on image samples from the VideometerLab, $n = 70$ and using 8 non-zero coefficients.

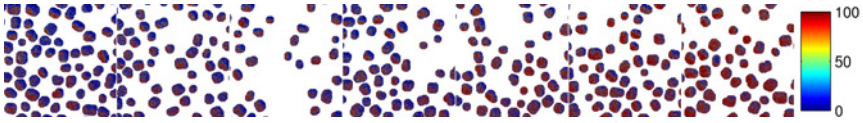

Figure E.28: Projected VideometerLab images using the PLSR model, visualised using the jet colour map where 0 ppm astaxanthin is blue, and 100 ppm astaxanthin is shown as red. The images are taken from the validation set, cropped, clamped and masked. The pellets with different levels of synthetic astaxanthin coating concentration, from left to right: 0, 3.125, 6.25, 12.5, 25, 50, 100 ppm.

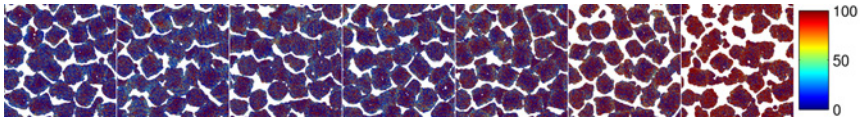

Figure E.29: Projected SuperK images using the PLSR model, visualised using the jet colour map where 0 ppm astaxanthin is blue, and 100 ppm astaxanthin is shown as red. The images are taken from the validation set, cropped, clamped and masked. The pellets with different levels of synthetic astaxanthin coating concentration, from left to right: 0, 3.125, 6.25, 12.5, 25, 50, 100 ppm.

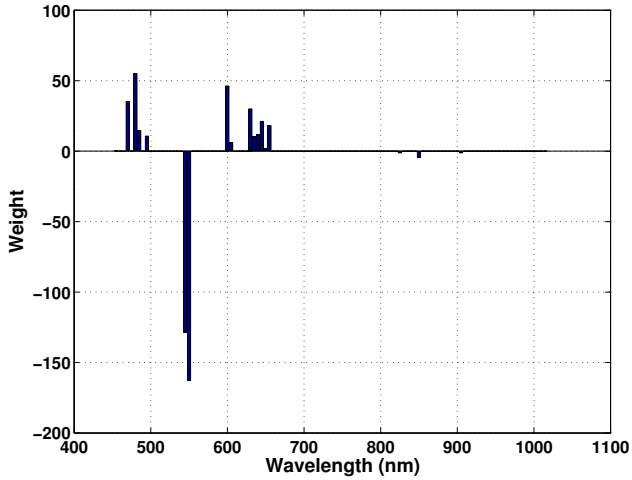

Figure E.30: The coefficients in $\boldsymbol{\beta}_{en}$ from the prediction model of synthetic astaxanthin coating using EN regression with LOOCV on image samples from the SuperK, $n = 70$ and using 19 non-zero coefficients.

E.4 Discussion

The results from the multi-spectral VideometerLab and the hyper-spectral SuperK indicate that it is possible to predict synthetic astaxanthin coating on pellets.

The design has minimised the structure of the semi diffuse illumination used in the SuperK set-up so it visually becomes insignificant. It is evident that the presented technique using an Engineered Diffuser provides a sufficient trade-off between a smooth uniform illumination and high power transmission.

In addition, the SuperK system's image acquisition reproducibility was investigated. The results presented in Figure E.5 show low variation above 470 nm.

In industry it is desired to know the astaxanthin coating level with an accuracy of roughly 1 ppm, which corresponds to a sensitivity of 1% of the pixel intensity for the present study. For this reason it was satisfactory that the reproducibility SD of the power stabilised SuperK images taken over long acquisition times (11 hours) proved to be below 1%, see Figure E.5.

For each image acquisition, the two systems examined different numbers of pellets due to the difference of field of view. However, this difference was not

significant since a large number of pellets were investigated in each image.

Previous studies of astaxanthin [3, 21, 156] found absorbance peaks of astaxanthin of around 450 – 505 nm and secondary peaks of around 500 – 600 nm for various solvents, as well as at 870 nm. This corresponds with the spectrometer results seen in Figure E.12.

To continue the data exploration we have presented the spectral difference of the different synthetic astaxanthin coating concentration levels, seen in Figures E.14 and E.15. For both modalities the largest discrimination between data was present in the $\sim 500 - 550$ nm wavelength range. This is in good agreement with the difference in spectroscopy spectra, presented in Figure E.12, of fish oil with and without synthetic astaxanthin. Since astaxanthin is a pigment, it makes sense that the visual range of the spectrum is of importance in the results.

The two vision systems presented very similar characterisations of the samples. Spectral response from both systems shows a clear separation between concentration levels for the wavelengths of about 510 – 530 nm, and also along the entire spectrum. SuperK showed more distinction between the small concentration levels, which can be seen both in the difference spectra and the PCA plot, see Figures E.15 and E.17.

For concentration prediction, PLSR and EN models were trained on the data from each instrument and both systems were able to perform results suitable for industrial screening and quality inspection, as the high RPD values between 4 and 24 presented in Table E.3 indicate.

PLSR components 1 and 2 include a small amount of all spectral bands and these alone can explain a moderate part of the variance in the data corresponding to the reference values, see Figures E.24 and E.25. This could be interpreted such that the overall intensity in all spectral bands explains a part of the synthetic astaxanthin concentration level. However, this is not enough for quality control for the VideometerLab data with respect to RPD value, and just enough for quality control for the SuperK data, as can be seen in Figure E.23. This can be compared to the results in [37] where they found astaxanthin concentration in fish fillets to be strongly dependent on the overall pixel intensity in multispectral images, stated both for PC1 and PLSR component 1.

However, for astaxanthin in pellet coating it seems as if the concentration level has a more subtle dependency on pixel intensity, since the characteristics appear first in PC2, see Figures E.16 and E.17, and in PLSR component 2 and onwards, indicating that the concentration variance is a smaller portion of the data variance. This is common for variance of interest in image analysis [53]. In a previous study of astaxanthin coating, PC2 was also found to be of impor-

tance for detecting the presence of astaxanthin [87], [Paper C]. Furthermore, for astaxanthin coating concentration prediction, PLSR component 2 and onwards showed considerable characteristics for prediction in [90] and component 3 and onwards in [89].

The RPD test shown in Figure E.23 illustrates that more than about 10 PLSR components do not improve the results, which is confirmed by Figure E.18. We therefore conclude that the regression problem for this data has a low complexity since 3 components suffice, though still with a considerable prediction error, and this is considerably improved by a few more components up to about 7 or 10 components.

The regression models show similar structures between VideometerLab and SuperK, both using PLS regression and EN regression. The PLS regression chose primarily two spectral regions for discriminating between the coating concentrations. The weight of the PLSR components and EN coefficients corresponds well with the variance seen in the spectral difference of the different astaxanthin levels shown in Figures E.14 and E.15. The weight of the PLSR coefficients also corresponds well with the primary absorbance peaks found of around 450 – 505 nm in previous studies of astaxanthin, and both PLSR and EN coefficients correspond well with the secondary absorption peaks of around 500 – 600 nm and 870 nm. This also corresponds to the spectroscopy results in Figure E.12.

Since the PLSR component weights are somewhat clustered to the above-mentioned regions, it makes sense to use these regions for making optical filters for an industrial inspection system. The weights of the EN coefficients are clustered in two main parts with opposite signs in the visual range for both modalities, which suggests that the prediction in future could be made using two optical filters. Optical filters can make the equipment cheaper and faster for industrial quality inspection of astaxanthin. The optimum design of such filters can be estimated by using sparse methods such as EN or filter-focused methods [76, 90, 102].

For the EN results it can be seen that the RPD increases with the number of coefficients. While more coefficients in some cases can increase the result, it also enables EN to select different clusters of correlated variables.

To directly compare the performance of the two vision systems, the overlapping 16 bands from the two were used for prediction and the results are presented in Table E.3. The VideometerLab data show a prediction error of 13 ppm, while the SuperK have a prediction error of 4 ppm. This is too high for the industry and thus means that many spectral bands are important for a result with high accuracy for this particular prediction problem.

The SEP for the VideometerLab is about 5-8 ppm of synthetic astaxanthin

concentration using PLSR and EN, and the SEP for SuperK with 3 PLSR components is about 3.7 ppm, which means that the error is larger than the smallest level of synthetic astaxanthin; 3.125 ppm. This means that the VideometerLab results are uncertain for this particular level; perhaps this is the limit of the used system. It can be noted that there is an overlap between the smallest astaxanthin concentration levels seen in the PCA plots in Figure E.16 and E.17.

Both PLSR and EN perform well for the prediction problem presented. However, the EN prediction model (coefficients) is more interpretable than the PLSR model (components); compare Figures E.24 and E.25 with Figures E.27 and E.30. While PLSR includes all spectral bands in several components in the prediction model, though weighted, EN selects just a few spectral bands which make the model easier to interpret and also makes it possible to use a low number of spectral bands.

For testing the generalisation of the PLSR prediction model, a validation scheme here called GFCV was used for leaving out one concentration level at a time for validation. This gives an indication on how the prediction behaves for unseen concentration levels. It is natural to expect a somewhat higher error in this case since the model has not been trained on all concentration levels. However, the generalisation result of GFCV is considered a more honest result than by using LOOCV. It is shown that the pooled prediction error of GFCV is much larger than the corresponding error of LOOCV for both systems, see Table E.4. The large difference in prediction error implies that the LOOCV scheme in combination with data with many variables compared to the number of samples, gives some over-fitting. This can also be assumed from the very optimistic results of both PLSR and EN for the SuperK data with 113 variables, compared to the VideometerLab's 20 variables. The optimistic results by using LOOCV on all concentration levels are partly explained by the fact that the study contained only one production batch. It is clear that as the complexity of the reflection increases, the background may have very different contributions from different chemical compounds that all contribute in the surface reflection.

It is therefore concluded, that in order to make a robust and precise prediction model for synthetic astaxanthin coating concentration it is important to use all target concentration levels, and also that future work examines different production batches.

However, as mentioned previously, HPLC measurements of astaxanthin from fish feed pellets are less accurate than when measuring astaxanthin in oil. A clear difference could be seen in the two measurements of the pellets in Table E.2. Therefore, spectral imaging could be a good complement for screening of synthetic astaxanthin coating.

E.5 Conclusions

A new instrument for hyper-spectral imaging, the SuperK set-up, based on a spectral broad laser light source, was introduced together with a parallel study with the commercially available multi-spectral VideometerLab imaging system. We have shown that the new SuperK system can be used for chemical surface inspection using hyper-spectral image analysis.

The results show that it is possible to predict the synthetic astaxanthin concentration in the coating well enough for quality control using either multi- or hyper-spectral image analysis. Results also show that the SuperK set-up performs with higher accuracy than the VideometerLab for predicting the synthetic astaxanthin concentration in the pellets, while the VideometerLab performs well enough for quality control. The results were obtained by only measuring surface reflections, which in combination with the good results implies that the methods can be used in general for quality inspection of various coating substances using similar coating methods.

In addition, the higher spectral resolution of the SuperK system combined with sparse statistics for analysing the signals, made it possible to identify the most significant spectral regions for the particular detection of astaxanthin. This is of interest for a simple and robust commercial system.

Acknowledgements

The work presented has received funding from BioMar A/S and the EU under the Seventh Framework Programme FP7/2007-2013 under grant agreement number 214505.10. This work was in part financed by the Centre for Imaging Food Quality project which is funded by the Danish Council for Strategic Research (contract no 09-067039) within the Programme Commission on Health, Food and Welfare. The expert technical assistance of Heidi Olander Petersen is gratefully acknowledged.

Appendix F

Classification of Astaxanthin Colouration of Salmonid Fish using Spectral Imaging and Tricolour Measurement

---

Martin Georg Ljungqvist, Bjørn Skovlund Dissing,

Michael Engelbrecht Nielsen, Bjarne Kjær Ersbøll,

Line Harder Clemmensen, Stina Frosch

IMM-Technical Report-2012-08, Technical University of Denmark (DTU) [85].

Abstract

The goal of this study was to investigate if it is possible to differentiate between rainbow trout (*Oncorhynchus mykiss*) having been fed with natural or synthetic astaxanthin. Three different techniques were used for visual inspection of the surface colour of the fish meat: multi-spectral image capturing, tricolour CIELAB measurement, and manual SalmoFan inspection. Furthermore it was tested whether the best predictions come from measurements of the steak or the fillet of the fish. Methods used for classification were linear discriminant analysis (LDA), quadratic discriminant analysis (QDA), and sparse linear discriminant analysis (SLDA).

F.1 Introduction

The colour of salmonid fish is one of the most important quality parameters for customers [57, 108, 127]. Consumers associate increased level of red in salmonid fishes with superior quality, and colour is the first quality parameter inspected by the customer [5]. Therefore, it is of outermost importance for the industry to understand the effect of breed conditions and processing on the colour development in salmonid fish fillets.

Astaxanthin has a high antioxidant activity, is essential for reproduction, growth and survival, and important for the development of colour in salmonid fish [128]. The primary use of astaxanthin within aquaculture is as a feed additive to ensure that farmed salmon and trout have similar appearance to their wild counterparts [138]. For this purpose, fish feed pellets are coated with fish oil with added astaxanthin in order for the fish to get the red meat pigmentation. Synthetic astaxanthin is more easily available and costs slightly less than natural astaxanthin and is therefore used more often in the industry. However, there is a demand for natural astaxanthin for the organic salmonid fish market where natural astaxanthin is mandatory.

Several studies has investigated how different processing conditions influences the colour in the fillets [42, 77, 151, 152]. Some studies investigating the effect of astaxanthin source (natural versus synthetic) on astaxanthin concentration in the muscle and physical performance criteria such as growth [15, 146], and to distinguish between natural and synthetic astaxanthin chemically in fish [139] can be found, whereas literature about the effect of astaxanthin source on meat colour to our knowledge is almost non existing.

The aim of this study was to investigate if natural and synthetic astaxanthin give different fish meat colour. The goal was to be able to differentiate between fish having been fed with natural and synthetic astaxanthin by using machine vision techniques. This is important since the organic salmonid fish market has to use natural astaxanthin in the feed. Furthermore, it was tested whether the best predictions were obtained from vision analysis of the steak or the fillet of the fish.

The colour of salmonid fish fillets has previously been inspected by several methods such as tricolour measurements [27, 151, 152], spectroscopy [17, 47, 109, 148] and visible imaging [64, 99, 151, 152]. Recently, Dissing et al. (2011) [37] predicted natural astaxanthin concentration level in salmonid fish fillets by multispectral images.

The fish colour in this study was measured using three different systems: multispectral imaging, CIELAB point measure, and SalmonFan visual judgement.

F.2 Materials and Methods

F.2.1 Fish

A total of 45 rainbow trout (*Oncorhynchus mykiss*) were used in the study. The fish were bread in indoor tanks holding 15° Celsius and fed with EcoLife Pearl 4.5 mm fish feed pellets (BioMar A/S, Brande, Denmark). The fish were segregated intro three holding tanks, with 15 fish in each tank, for the feeding trial:

- Control: Fish fed with feed using no additional astaxanthin.
- Natural: Fish fed with feed coated with 25 ppm of natural astaxanthin.
- Synthetic: Fish fed with feed coated with 25 ppm of synthetic astaxanthin.

Each fish was uniquely marked by a micro chip. This gave the opportunity to relate all information on individual level. All fish up to the experiment was fed with non pigmented feed.

Diets were prepared exclusively for this study by a commercial feed company (BioMar A/S, Brande, Denmark). The basic pellet, EcoLife Pearl, was used in all diets. All pellets where coated with fish oil containing either 25 ppm

synthetic astaxanthin (BASF SE, Germany), 25 ppm natural astaxanthin [103], or no astaxanthin added (control). The fish oil used all originated from the same batch.

When slaughtered, all 45 fish where weighed and the fork length measured. Each fish was cleaned and de-headed before cut into both a steak and fillet, see Figures F.1, F.2, and F.3. Two biopsies, left and right, were done for each steak, see Figures F.3, and F.4.

After cutting, the samples were placed in plastic petri dishes (90 mm diameter) and stored on ice in Styrofoam boxes. After 30 minutes of storage the samples were measured first by multi-spectral image analysis, then Minolta measurements where conducted before evaluation with the SalmoFan Lineal. Finally, each sample was minced and subsequently frozen at −40° C. After 14 days of storage the astaxanthin concentration was determined by chemical determination.

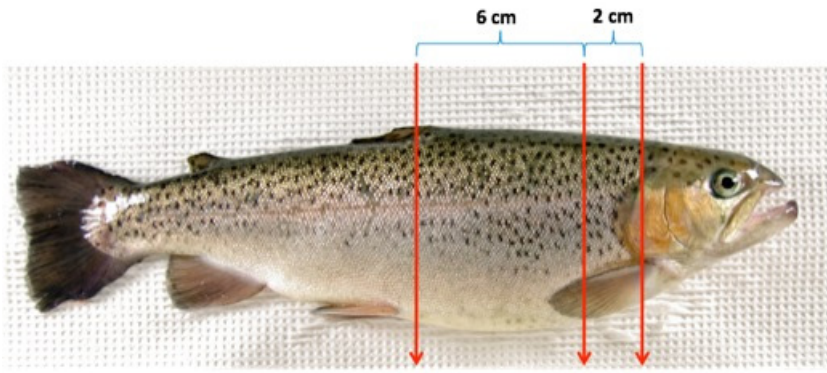

Figure F.1: Overview of where the rainbow trout is cut for steak and fillet.

F.2.2 Methods

F.2.2.1 Chemical determination of astaxanthin content

Astaxanthin of the minced fillets or biopsies was determined in duplicate from the lipid extracts of the fish meat using an Agilent 1100 series high pressure liquid chromatography (HPLC) (Agilent Technologies, Palo Alto, CA), equipped with a UV diode array detector. The fillet or biopsy sample was minced, and 10 g in duplicates was used for extraction using chloroform and methanol according

Figure F.2: Example of a rainbow trout fillet.

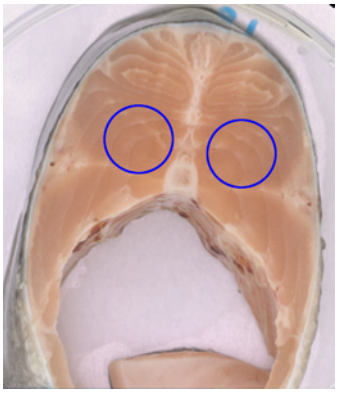

Figure F.3: Example of a rainbow trout steak, with the places for the biopsies marked by blue circles.

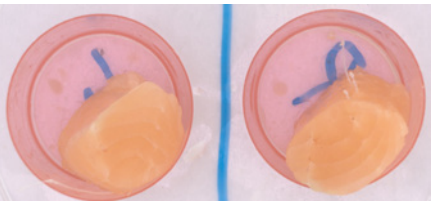

Figure F.4: Example of left and right biopsies from the steak in Figure F.3.

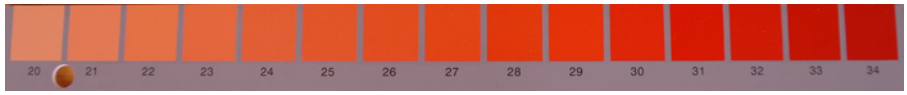

Figure F.5: SalmoFan Lineal with pigmentation gradient from 20 to 34.

to the modified protocol of Bligh and Dyer [16]. A fraction of the lipid extract was evaporated under nitrogen and re-dissolved in 2mL of *n*-heptane before injection. The astaxanthin content was determined after injection of an aliquot (50 μL) of the *n*-heptane fraction onto a LiChrosorb Si60-5 column (100 mm $\times$ 3 mm, 5 μm) equipped with a Chromsep Silica (S2) guard column (10 mm $\times$ 2 mm; Chrompack, Middelburg, The Netherlands) and eluted with a flow of 1.3 mL/min using *n*-heptane/acetone (86:14, v/v) and detection at 470 nm. Concentrations of astaxanthin were calculated using authentic standards from Dr. Ehrenstorfer GmbH (Augsburg, Germany).

F.2.2.2 SalmoFan

A SalmoFan Lineal (DSM Nutritional Products Ltd, Basel, Switzerland) pigmentation chart was used for manual inspection by three people individually. The SalmoFan has a colour gradient scale numbered 20 to 34, see Figure F.5. The SalmoFan Lineal was visually compared to the fish meat and the closest match in colour intensity was decided manually. The SalmoFan Lineal is commonly used for colour quality inspection in the salmonid fish industry.

F.2.2.3 Tricolour Device

Tricolour point measurements were furnished using a hand-held Minolta Chroma Meter II-CR200 (Minolta Co. Ltd, Japan). The Minolta colorimeter provides controlled illumination of the sample and is commonly used for measuring the average colour of a food sample area. CIELAB values from the Chroma Meter's surface reflection measurements were used.

The CIELAB (L^*, a^*, b^*) colour space is perceptually uniform and specified by the International Commission on Illumination (CIE). L^* closely matches the lightness perceived by human vision, while a^* represents red and green, and b^* represents yellow and blue.

The CIE L^*, a^*, b^* values were determined at two locations on the fillet sample (see Figure F.11) and in the centre of each biopsy.

F.2.2.4 Spectral Imaging

The equipment used for image acquisition is a camera and lighting system called VideometerLab (Videometer A/S, Hørsholm, Denmark) which supports a multi-spectral resolution of 20 wavelengths. These are distributed over the ultra-violet A (UVA), visible and first near infra-red (NIR) region: 385, 430, 450, 470, 505, 565, 590, 630, 645, 660, 700, 850, 870, 890, 910, 920, 940, 950, 970, 1050 nm.

This system uses a Point Grey Scorpion SCOR-20SOM grey-scale camera and the objects of interest are placed inside an integrating sphere (Ulbricht sphere) with uniform diffuse lighting from light sources placed around the rim of the sphere. All light sources are light emitting diodes (LED) except for 1050 nm which is a diffused laser diode.

The curvature of the sphere and its white matte coating ensures a uniform diffuse light so that specular effects are avoided and likewise minimising the amount of shadows. The device is calibrated radiometrically with a following light and exposure calibration. The system is also geometrically calibrated to ensure pixel correspondence for all spectral bands [48].

The image resolution is 1280 $\times$ 960 pixels. Each file contains 20 images, one for each spectral band. In this situation one pixel represents approximately 0.072 $\times$ 0.072 millimetres. The Scorpion camera has a 12 bit analogue to digital converter (ADC), and the system used 8 bit data output from the camera. The correction for calibration gives reflectance intensity output of 32 bit precision.

The performance of the VideometerLab has previously been validated for similar surface chemistry applications [30, 31, 32, 37, 39, 40, 56, 62, 87, 89, 90].

F.2.3 Data Acquisition

The fish fillets and biopsies were placed in petri dishes (plastic, diameter of 9 cm) and thereafter inspected using the VideometerLab, the Minolta Chroma Meter (CIELAB), and the SalmoFan Lineal. In total 45 fillet measurements were captured. For the steak, 45 CIELAB and SalmoFan Lineal measurements were performed. Moreover, for the steak biopsies (left and right) 45 multi-spectral images were captured. The measurement order of all samples was randomised for all measurement systems used in this study.

Standard red-green-blue (sRGB) colour image representations of the Videometer-Lab images for this paper were done by multi-spectral colour-mapping

using penalised least square regression described in Dissing et al. (2010) [36].

F.2.4 Data Analysis

F.2.4.1 Pre-processing

Each multi-spectral image was normalised using standard normal variate (SNV) for each pixel. This means that the mean was subtracted from every pixel, and divided by the standard deviation of the pixel values [117]. This pre-processing was done in order to reduce the effect of difference in astaxanthin concentration levels between the three different groups since the scope of the study is to investigate if there is a colour difference between fish natural versus synthetic astaxanthin.

The region of interest (ROI) in each fillet image was segmented using the first factor of the maximum autocorrelation factor (MAF) method [135]. The images of the biopsies were segmented manually.

After SNV the mean value of all pixels in the regions of interest was used as samples, resulting in 45 samples. The mean of left and right biopsy was used. Furthermore, nine different percentiles (1, 5, 10, 25, 50, 75, 90, 95, 99) were calculated of the SNV normalised pixels from the VideometerLab images, resulting in a total of 180 variables. With 45 samples and 180 variables this results in an ill-posed problem.

F.2.4.2 Model Selection and Validation

For validation and parameter calibration of the statistical models the leave-one-out cross-validation (LOOCV) method was used, were each sample is used as validation once. For LOOCV the error rate is almost unbiased for the true (expected) prediction error, but could have high variance since the training sets are so similar to each other [63].

Because of the low number of samples in the study the bootstrap re-sampling method was used for validation in some cases. In this way it was tested how the prediction generalises for different subsets of samples.

A training set of 30 samples and test set of 15 samples were defined, randomly selected so that the training set has 10 samples from each group, and the test

set has 5 samples from each group. When not using LOOCV or bootstrap, the statistical models were assessed using this test and training set. The samples in the training and test sets are shown in Tables F.1 and F.2.

Table F.1: Training set

Natural	Synthetic	Control
6	22	32
3	16	40
11	30	34
7	28	35
14	17	45
8	29	33
5	21	38
15	25	42
1	27	41
2	26	37

Table F.2: Test set

Natural	Synthetic	Control
4	19	31
13	23	43
9	18	44
10	24	36
12	20	39

F.2.4.3 Discriminant Analysis

Statistical discriminant analysis was made in order to separate fish fed with added natural astaxanthin from synthetic astaxanthin. Methods used were linear discriminant analysis (LDA), quadratic discriminant analysis (QDA) [43], and sparse linear discriminant analysis (SLDA) [28].

SLDA was used to regularise the ill-posed problem and select the most important variables for discriminating between the groups. SLDA is using the elastic net (EN) for variable selection [160]. The EN tends to select variables that are correlated with each other. EN needs two calibration parameters: the λ_1 steers the L_1 norm for determining the number of non-zero components, and λ_2 controls the L_2 (Euclidean) norm for the regularisation. The two model parameters, the number of selected variables and λ_2, were chosen using LOOCV

on 10 samples from each group, and the chosen model was then validated on 5 samples from each group.

The λ_1 parameter is steering the selection of variables and was calculated so that the number of selected variables was varied from 1 to 10. The λ_2 parameter was varied with 12 logarithmic steps from 10^{-7} to 10. The data were normalised for each calculation of the SLDA. If more than one combination of number of selected variables and λ_2 was found to give the best calibration result, then the lowest number of selected variables and the highest value of λ_2 was used, giving the least complex model.

Since the number of samples is relatively small, this procedure was then wrapped in a bootstrap of 50 iterations in order to see how stable the model was. For comparing purposes the same randomised indices for calibration and validation sets used in the bootstrap were the same for both fillet and biopsy. In this way the same fish were used for calibration and validation sets for both fillet and biopsy.

The SLDA algorithm calculates sparse discriminant components that give the best classification of the groups. The number of components is one less than the number of groups. These components are linear combinations of the selected variables.

Further more, another method for evaluating spectral bands was done by performing LDA classification on band combinations (subsets). One band at a time was tested, along with all exclusive combinations of up to six bands in an extensive test for the lowest classification error. LOOCV was used for model selection.

In order to compare LDA with subsets and SLDA we used Wilk's Λ which in principle consists of the ratio of the within group variation ($\mathbf{W}$) and the total variation ($\mathbf{T}$), i.e. the within group plus the between group variation, see Equation F.1. A value of Wilk's Λ which is close to zero indicates that the groups are well separated. The band combination with the lowest value of Wilk's Λ was chosen.

$$\Lambda = \frac{\det(\mathbf{W})}{\det(\mathbf{T})} \,. \tag{F.1}$$

Hotelling's T^2 test was used in order to see if the two group means of natural and synthetic astaxanthin were significantly different [66].

All image analyses and statistics were carried out using Matlab 7.9 (The Mathworks Inc., Natick, MA, USA).

F.3 Results

The experimental results are presented in this section, divided into three parts. Firstly, an overview of the experiment is presented. Secondly, the classification of astaxanthin type using tricolour measurement and SalmoFan inspection is reported. Thirdly, the classification of astaxanthin type using spectral imaging is shown.

F.3.1 Experiment Overview

The fish were weighed in the beginning and end of the feeding time period, the increase in weight can be seen in Figure F.6. This shows that some fish ate much of the feed and some fish did not eat much, which also would relate to the amount of astaxanthin they have assimilated.

In the end of the experiment, after 14 days of frozen storage, the chemical content of astaxanthin was determined using HPLC analysis, see Figure F.7. It can be seen that the average astaxanthin content is different between the three groups. Especially between the natural and synthetic astaxanthin group there is a large difference in average astaxanthin concentration. Here we can confirm the large variation of astaxanthin content between the fish as implied by the weight differences.

F.3.2 Tricolour and SalmoFan

The fish meat was analysed using a CIELAB detector, which was compared with using an ordinary SalmoFan sensor panel.

The CIELAB values can be seen in scatter plots in Figure F.8. It shows that a^* and b^* show a structure for the three groups, while the groups does not seem to be separated with regards to L^* values. This means that the colour information is more important than the lightness with respect to separating natural and synthetic astaxanthin.

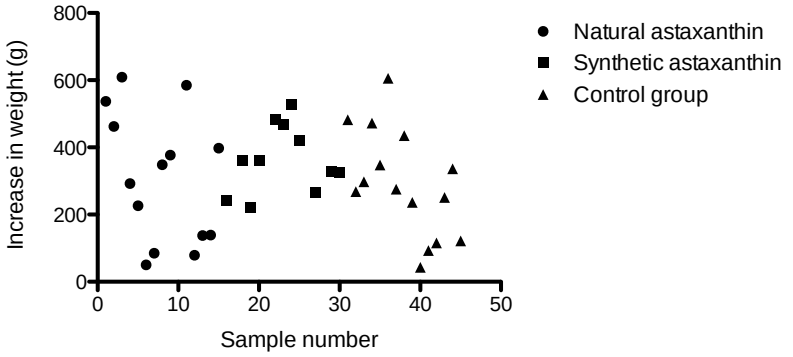

Figure F.6: The increase of weight of the fish during the experiment.

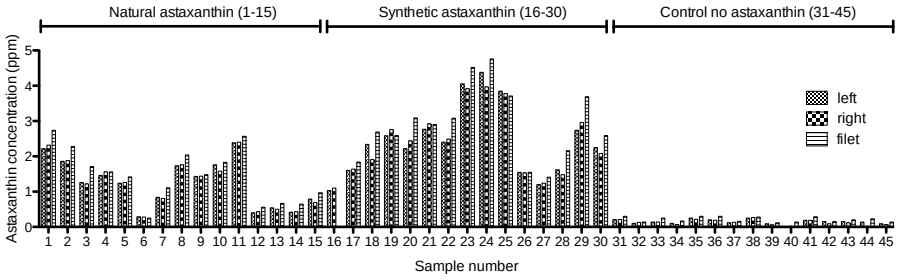

Figure F.7: The astaxanthin concentration in ppm in the fillet, as well as right and left biopsy, measured by HPLC.

Mean results from the SalmoFan sensor panel can be seen in Figure F.8 where a clear grouping of the three groups can be seen, especially for the biopsy measurements.

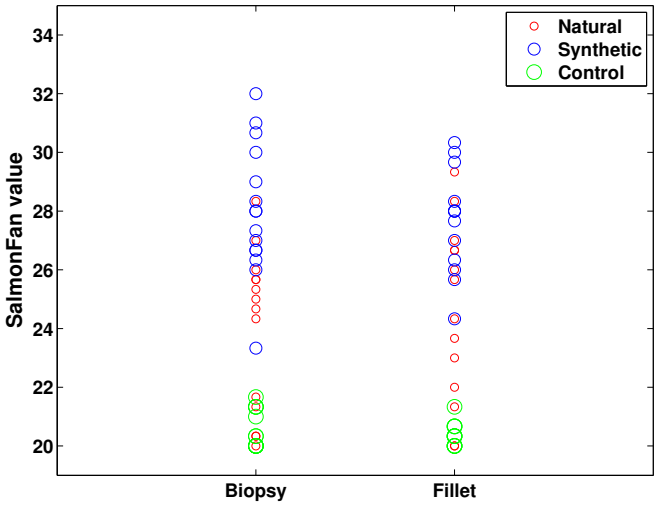

Figure F.8: The SalmoFan Lineal mean values for biopsy and fillet.

Classification of the three groups was done using LDA and QDA. Because of the relatively few samples the classification was repeated by doing a bootstrap with randomly chosen sets for 100 iterations and calculating the mean of the classifications.

The reflection spectra of the SalmoFan individual pigmentation levels was analysed using the VideometerLab and the result can be seen in Figure F.10.

The control group is classified by 92-99% by QDA. For LDA this group is classified by 99-100% for the SalmoFan data, and 96% for CIELAB.

For CIELAB the classification of natural and synthetic astaxanthin is in the range of 63-76%, while for the SalmoFan the corresponding classification is 38-82%.

Both LDA and QDA show generally better results for synthetic compared to natural astaxanthin classification for the SalmoFan data. The same tendency is not clearly seen for CIELAB values.

It shows that the classifications for steak are somewhat better than those for fillet on the CIELAB data.

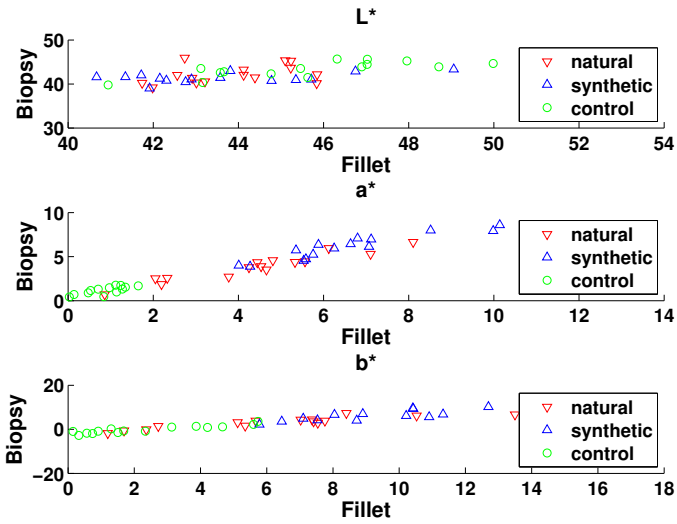

Figure F.9: The CIELAB values in scatter plots for biopsy and fillet.

Overall QDA showed about the same or better results than the LDA, therefore the QDA results are here presented and can be seen in Table F.3.

To see if the length and weight influence the result we did the same bootstrap but on the residuals from a regression on length and weight. The results were similar to the ordinary bootstrap results but showed improvement for natural astaxanthin for the SalmoFan data, mostly on fillet but also for steak. For the CIELAB values QDA improved on the synthetic astaxanthin with this method, see Table F.4 for the QDA results.

To see if the length, weight and astaxanthin concentration influence the result we did the same bootstrap but on the residuals from a regression on length, weight and astaxanthin concentration. The results were all (about twice as) worse than the ordinary bootstrap results (results not shown).

To see if the astaxanthin concentration alone influences the result we did the same bootstrap but on the residuals from a regression on the astaxanthin concentration. The results were all (about twice as) worse than the ordinary bootstrap results (results not shown).

(a) Confusion matrix for CIELAB steak on a 100 QDA classification bootstrap

	Natural	Synthetic	Control
Natural	0.7220	0.2080	0.0700
Synthetic	0.2540	0.7440	0.0020
Control	0.0580	0.0140	0.9280

(b) Confusion matrix for CIELAB fillet on a 100 QDA classification bootstrap

	Natural	Synthetic	Control
Natural	0.6520	0.2780	0.0700
Synthetic	0.3140	0.6860	0
Control	0.0420	0.0300	0.9280

(c) Confusion matrix for SalmoFan steak on a 100 QDA classification bootstrap

	Natural	Synthetic	Control
Natural	0.4680	0.2240	0.3080
Synthetic	0.2180	0.7820	0
Control	0.0360	0	0.9920

(d) Confusion matrix for SalmoFan fillet on a 100 QDA classification bootstrap

	Natural	Synthetic	Control
Natural	0.4820	0.3400	0.1780
Synthetic	0.1840	0.8160	0
Control	0.0520	0	0.9480

Table F.3: Confusion matrices for QDA.

(a) Confusion matrix for CIELAB steak residual on a 100 QDA classification bootstrap

	Natural	Synthetic	Control
Natural	0.7260	0.1280	0.1460
Synthetic	0.1880	0.8060	0.0060
Control	0.1000	0.0280	0.8720

(b) Confusion matrix for CIELAB fillet residual on a 100 QDA classification bootstrap

	Natural	Synthetic	Control
Natural	0.6720	0.2340	0.0940
Synthetic	0.2580	0.7400	0.0020
Control	0.0720	0.0420	0.8860

(c) Confusion matrix for SalmoFan steak residual on a 100 QDA classification bootstrap

	Natural	Synthetic	Control
Natural	0.5620	0.2040	0.2340
Synthetic	0.2180	0.7740	0.0080
Control	0.1080	0	0.9340

(d) Confusion matrix for SalmoFan fillet residual on a 100 QDA classification bootstrap

	Natural	Synthetic	Control
Natural	0.6420	0.2020	0.1560
Synthetic	0.1160	0.8840	0
Control	0.0740	0	0.9260

Table F.4: Confusion matrices for QDA.

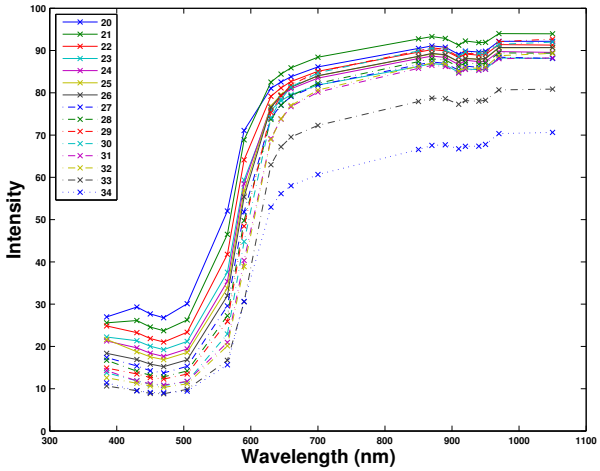

Figure F.10: VideometerLab mean reflection spectra of the SalmoFan with pigmentation scale of 20–34.

F.3.3 Spectral Imaging

Multi-spectral images of trout fish meat were captured using the VideometerLab and segmented using CDA. An example of a segmented fillet image with the ROI visualised can be seen in Figure F.11, and examples of the three different groups can be seen in Figure F.12. All fish fillets can be seen in Figure F.13, illustrating the group variation. The pixels in the ROI in each image were normalised using SNV and two different feature sets were extracted: mean spectra, and nine percentiles. The features were analysed using LDA, QDA, and SLDA in order to discriminate between fish meat from fish fed with synthetic astaxanthin, natural astaxanthin and no astaxanthin.

The mean sample spectra show a separation between the groups between 450 and 500 nm, see Figure F.14. However, the separation is more distinct for the control group than between natural and synthetic astaxanthin.

Classification between all three groups of fish fillets and steak biopsies using LDA on the mean spectra shows that the control group is always correctly classified, both for fillet and biopsy, and both when using the train and test set as when using LOOCV, see Tables F.5, F.6 and F.7. We therefore focus on the results and optimal variables used in order to classify between natural and synthetic astaxanthin.

Hotelling's T^2 test for separate means done on the mean spectra showed that

Figure F.11: Trout fillet image example. An sRGB representation of the multi-spectral VideometerLab image, with the segmented ROI visualised with a white outline.

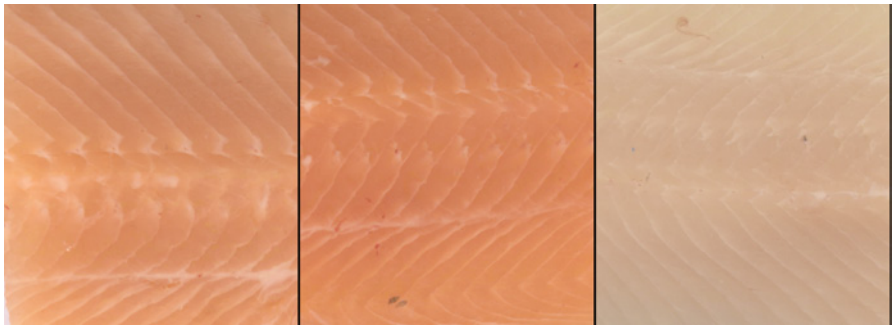

Figure F.12: Trout fillet images of the three different groups: Fish fed with feed using natural astaxanthin (left), synthetic astaxanthin (middle), and no additional astaxanthin (right). Here showing cropped sRGB representations of the multi-spectral VideometerLab images.

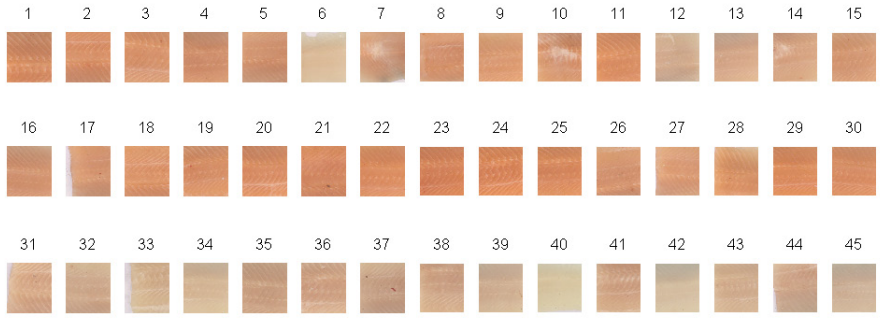

Figure F.13: All trout fillets. Top row, sample 1-15: Fish fed with feed using natural astaxanthin. Middle row, sample 16-30: Fish fed with synthetic astaxanthin. Bottom row, sample 31-45: Fish fed with no additional astaxanthin (control group). Here showing cropped sRGB representations of the multi-spectral VideometerLab images.

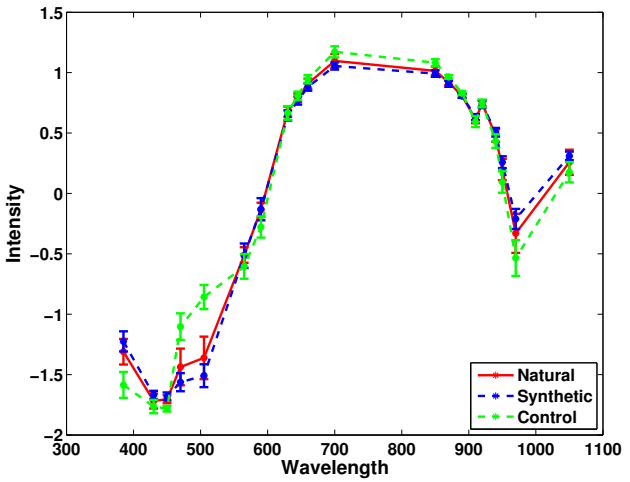

Figure F.14: Mean spectra of 45 multi-spectral images of trout biopsy, with ±1 sample standard deviation for each spectral band.

natural and synthetic astaxanthin is not separated with good significance level. For the biopsy spectral data $p = 0.25$ and for fillet the two groups were not significantly different. However, according to Wilk's Λ the two groups should be better separated for the fillet images than for the biopsy images, as can be seen in Table F.8.

Table F.5: Confusion matrix for LDA classification of all three groups using mean spectra of fillet images. Validated on the test set with 5 samples in each group.

Group	Natural	Synthetic	Control
Natural	3	2	0
Synthetic	3	2	0
Control	0	0	5

Table F.6: Confusion matrix for LDA classification of all three groups using mean spectra of biopsy images. Validated on the test set with 5 samples in each group.

Group	Natural	Synthetic	Control
Natural	2	2	1
Synthetic	2	3	0
Control	0	0	5

Table F.7: Classification between synthetic astaxanthin, natural astaxanthin and control group, using LDA on the mean spectra.

Type	LDA CV error	LDA Test error
Fillet	0.2667	0.3333
Biopsy	0.3111	0.3333

Classification of natural and synthetic astaxanthin using LDA on mean spectra of fillet and steak biopsy show poor results with an error larger than 50%. However, SLDA on percentiles and LDA using a subset of 6 mean spectral bands show promising results. For SLDA using percentiles, the classification is between 70% and 82%, and for LDA using 6 mean spectral bands gives 90% correct classification on fillet, and 80% on steak biopsy. Wilk's Λ show that natural and synthetic astaxanthin is better separated in the fillet images than the

Table F.8: Classification between synthetic and natural astaxanthin, using LDA and SLDA on the mean spectra of fillet and biopsy respectively.

Type	LDA CV error	SLDA Val. error	SLDA Val. min.	SLDA Val. std.	LDA 6 bands CV error	Wilk's Λ
Fillet	0.6667	0.2440	0	0.1232	0.1000	0.7718
Biopsy	0.5333	0.3000	0	0.1512	0.2000	0.8333

Table F.9: Classification between synthetic and natural astaxanthin, using SLDA on the percentile features. Ordinary LDA is not possible on ill-posed problems.

Type	LDA CV error	SLDA Val. error	SLDA Val. min.	SLDA Val. std.	LDA 6 bands CV error	Wilk's Λ
Fillet	-	0.2160	0	0.1376	-	0.7839
Biopsy	-	0.2540	0	0.1487	-	0.8375

Table F.10: Top 5 variables selected by SLDA for classification between synthetic and natural astaxanthin using the mean spectra. Frequency (Freq.) is the number of times that feature was selected in the 50 iteration bootstrap, a kind of variable importance.

Type	Freq.	Wavelength (nm)
Fillet		
	28	385
	23	700
	22	1050
	18	565
	18	590
	17	505
Biopsy		
	31	385
	26	920
	21	565
	21	890
	20	430
	18	910
	18	1050

Table F.11: Top 5 variables selected by SLDA for classification between synthetic and natural astaxanthin using the percentile features. Frequency (Freq.) is the number of times that feature was selected in the 50 iteration bootstrap, a kind of variable importance. Chosen band wavelength in nanometre and the percentile of that band.

Type	Frequency	Wavelength (nm)	Percentile
Fillet			
	17	700	99
	15	385	1
	9	1050	1
	8	590	25
	7	385	25
	7	630	99
Biopsy			
	17	385	1
	11	385	95
	11	890	1
	8	385	90
	8	630	99
	7	430	99
	7	920	90
	6	385	75
	6	385	99

steak biopsy images, irrespective of mean spectra or percentiles. Classification between synthetic and natural astaxanthin, using LDA and SLDA on the mean spectra can be seen in Table F.8, and the results for using SLDA on the spectra percentiles can be seen in Table F.9.

The results show that it is possible to classify the type of astaxanthin that has been fed to the trout, and the best results for classification between synthetic and natural astaxanthin is achieved by SLDA on percentiles and LDA using a subset of 6 bands. It seems as fillet is better than biopsy for classifying between synthetic and natural astaxanthin.

The wavelength most often chosen in the bootstrap generally for all tests is the UVA band 385 nm. For fillet the band of 700 nm is also highly important. The most often selected variables in the form of mean of spectral bands are shown in Table F.10. The most often selected variables in the form of percentiles of spectral bands can be seen in Table F.11.

To summarise, the results show that the control group, which was not fed with astaxanthin, is quite easy to separate from the two astaxanthin groups, while it is more difficult to separate the natural and synthetic groups, as can be seen in Figure F.15.

F.4 Discussion

Previous studies of astaxanthin [3, 21, 156] found distinguished absorbance peaks of astaxanthin around 450 – 505 nm and secondary peaks around 500 – 600 nm for various solvents, as well as around 870 nm. The lowest maximum found in petroleum ether (467-470 nm) and highest in carbon disulphide (502-505 nm). However, the spectral response of astaxanthin in fish meat is different from that of astaxanthin in oil due to how the astaxanthin is bind in the flesh. This means that the prediction model of astaxanthin in fish meat would be different from the prediction model for astaxanthin solved in oil.

In Dissing et al. (2011) [37] the concentration level of natural astaxanthin in fish fillet was highly correlated with the largest independent variance component in the multi-spectral image data. This means that the astaxanthin concentration is highly dependent on the overall image intensity.

With relatively few samples and large variation within the groups with regards to astaxanthin content this classification is challenging. Normalisation using SNV on each pixel was used in order to reduce the effect of different concen-

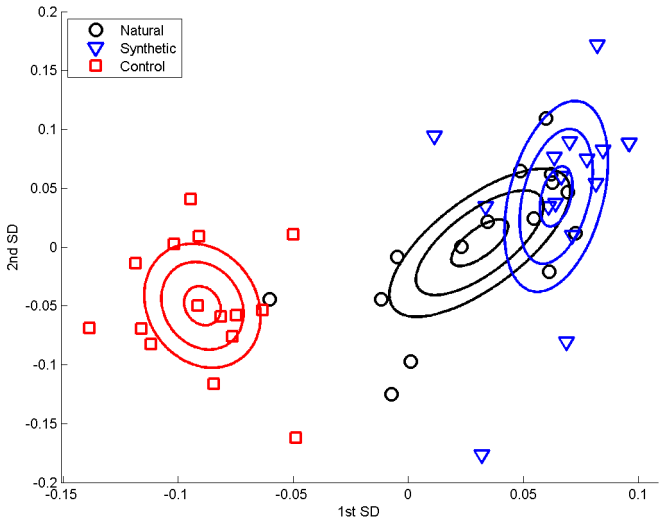

Figure F.15: The biopsy of salmonid fish fed with natural astaxanthin, synthetic astaxanthin, and no astaxanthin (control group). The samples are plotted using the two sparse discriminant components from SLDA, and estimated normal distribution contours are visualised for each group.

tration level between the groups. However, it is hard to reduce the difference completely. We cannot exclude the cause of concentration level completely in the results. An apparent overlap of synthetic and natural astaxanthin groups can be seen in the presented scatter plots (see e.g. Figure F.15), and it is possible that the classification is distinguishing the groups dependent on concentration level. However, when compensating for the concentration difference by using regression residuals in the classification the results were still not improved.

Furthermore, it has previously been shown that measuring the surface colour of a non-homogeneous object, such as meat, using a colorimeter such as the Minolta Chroma Meter usually gives erroneous colour results [55, 151]. Often a grey or purplish colour is reported, which is due to the light penetrating the sample and scattering inside the object, by the light coming from the colorimeter's illumination being close to the surface [55]. Colorimeters also only samples specific points on the surface. In comparison, imaging techniques usually have diffuse illumination and gives a more clear surface colour as a result. Imaging techniques therefore has the advantage for monitoring the entire surface of a non-uniform food sample capturing both shape and colour, including surface variations and producing a permanent picture reference.

F.5 Conclusions

The results show that it is easy to separate natural and synthetic astaxanthin from the control group using multi-spectral image analysis, tricolour analysis and SalmoFan analysis. However, it seems to be a more challenging task to separate natural astaxanthin and synthetic astaxanthin. Natural and synthetic astaxanthin show an overlap in spectral reflection, tricolour values, and SalmoFan values.

Using tricolour CIELAB measurements it shows that the classification of natural and synthetic astaxanthin is slightly better using the steak than the fillet.

For discriminating between fish fed with natural and synthetic astaxanthin the CIELAB measurements show better performance than the SalmoFan values.

Using spectral imaging, the results show that fillet is better than steak for classifying between synthetic and natural astaxanthin.

Acknowledgments

The work presented has in parts received funding from BioMar A/S and the EU under the Seventh Framework Programme FP7/2007-2013 under grant agreement number 214505.10. The expert technical assistance of Heidi Olander Petersen is gratefully acknowledged.

Bibliography

[1] Ansi/iec 60529-2004 degrees of protection provided by enclosures (ip code), November 2004. National Electrical Manufacturers Association (NEMA).

[2] Rolf Adams. Radial decomposition of discs and spheres. *Graphical Models and Image Processing*, 55(5):325–332, 1993.

[3] Sergiu Amarie, Ute Förster, Nina Gildenhoff, Andreas Dreuw, and Josef Wachtveitl. Excited state dynamics of the astaxanthin radical cation. *Chemical Physics*, 373(1-2):8–14, 2010.

[4] Lyle K. Anderson. Extraction of carotenoid pigment from shrimp processing waste, us3906112, September 1975.

[5] Stewart Anderson. Salmon color and the consumer. In *Microbehavior and Macroresults: Proceedings of the Tenth Biennial Conference of the International Institute of Fisheries Economics and Trade Presentations*, July 2000.

[6] J. Angulo and B. Schaack. Morphological-based adaptive segmentation and quantification of cell assays in high content screening. In *5th IEEE International Symposium on Biomedical Imaging: From Nano to Macro*, volume 1-4, pages 360 –363, May 2008.

[7] Morten Arngren, Per Waaben Hansen, Birger Eriksen, Jan Larsen, and Rasmus Larsen. Analysis of pre-germinated barley using hyperspectral image analysis. *Journal of Agricultural and Food Chemistry*, 2011.

[8] M.S. Azaza, M.N. Dhraief, M.M. Kraiem, and E. Baras. Influences of food particle size on growth, size heterogeneity, food intake and gastric evacuation in juvenile nile tilapia, oreochromis niloticus, l., 1758. *Aquaculture*, 309(1-4):193–202, 2010.

[9] R.T.M. Baker, A.-M. Pfeiffer, F.-J. Schöner, and L. Smith-Lemmon. Pigmenting efficacy of astaxanthin and canthaxanthin in fresh-water reared atlantic salmon, salmo salar. *Animal Feed Science and Technology*, 99(1-4):97–106, 2002.

[10] Sukumar Bandyopadhyay. Aquafeed extrudate flow rate and pellet characteristics from low-cost single-screw extruder. *Journal of Aquatic Food Product Technology*, 10(2):3, 2001.

[11] P. Yvonne Barnes, Edward A. Early, and Albert C. Parr. Nist measurement services: Spectral reflectance. National Institute of Standards and Technology Special Publication 250-48, Optical Technology Division, Physics Laboratory, National Institute of Standards and Technology (NIST), March 1998.

[12] R B Barnes. Thermography of the human body. *Science (New York, N.Y.)*, 140:870–877, 1963.

[13] R.J. Barnes, M.S. Dhanoa, and Susan J. Lister. Standard normal variate transformation and de-trending of near-infrared diffuse reflectance spectra. *Applied Spectroscopy*, 43(5):772–777, 1989.

[14] Bruce G. Batchelor, editor. *Machine Vision Handbook*. Springer London, 2012.

[15] B. Bjerkeng, M. Peisker, K. von Schwartzenberg, T. Ytrestoyl, and T. Asgard. Digestibility and muscle retention of astaxanthin in atlantic salmon, salmo salar, fed diets with the red yeast phaffia rhodozyma in comparison with synthetic formulated astaxanthin. *Aquaculture*, 269(1-4):476–489, 2007.

[16] EG Bligh and WJ Dyer. A rapid method of total lipid extraction and purification. *Canadian Journal of Biochemistry and Physiology*, 37(8):911–917, 1959.

[17] Claus Borggaard, Lars Bager Christensen, Knut Erik Gulbrandsen, and Allan J. Rasmussen. Method and apparatus for determining quality properties of fish, us6649412, November 2003.

[18] R. Bro, K. Kjeldahl, A. K. Smilde, and H. A. L. Kiers. Cross-validation of component models: A critical look at current methods. *Analytical and Bioanalytical Chemistry*, 390(5):1241–1251, 2008.

[19] Tadhg Brosnan and Da-Wen Sun. Improving quality inspection of food products by computer vision – a review. *Journal of Food Engineering*, 61(1):3–16, 2004.

[20] P. Bubrick. Production of astaxanthin from haematococcus. *Bioresource Technology*, 38(2-3):237–239, 1991.

[21] Manuel Buchwald and William P. Jencks. Optical properties of astaxanthin solutions and aggregates. *Biochemistry*, 7(2):834–843, 1968.

[22] Donald A. Burns and Emil W. Ciurczak, editors. *Handbook of near-infrared analysis*. CRC Press, 3rd edition, 2008.

[23] Jens Michael Carstensen and Jørgen Folm-Hansen. An apparatus and a method of recording an image of an object, ep1051660, November 2003.

[24] Jens Michael Carstensen, Michael Adsetts Edberg Hansen, Niels Christian Krieger Lassen, Per Waaben Hansen, Bjarne Kjær Ersbøll, and Thomas Martini Jørgensen. Creating surface chemistry maps using multispectral vision technology. In *9th MICCAI - Workshop on Biophotonics Imaging for Diagnostics and Treatment*. IMM-Technical Report-2006-17, 2006.

[25] Asger Nyman Christiansen, Jens Michael Carstensen, Flemming Møller, and Allan Aasbjerg Nielsen. Monitoring the change in colour of meat: A comparison of traditional and kernel-based orthogonal transformations. *Journal of Spectral Imaging*, 3(1), 2012.

[26] Asger Nyman Christiansen, Jens Michael Carstensen, Olga Papadopoulou, Nikos Chorianopoulos, Efstafios Z. Panagou, and George-John E. Nychas. Multi spectral imaging analysis for meat spoilage discrimination. In J.M. Frias E. Cummins and V.P. Valdramidis, editors, *7th International Conference on Predictive Modelling of Food Quality and Safety*, pages 384–387, Dublin, Ireland, September 2011.

[27] R. Christiansen, G. Struksnaes, R. Estermann, and O. J. Torrissen. Assessment of flesh colour in atlantic salmon, salmo salar l. *Aquaculture Research*, 26(5):311–321, 1995.

[28] Line Clemmensen, Trevor Hastie, Daniela Witten, and Bjarne Ersbøll. Sparse discriminant analysis. *Technometrics*, 53(4):406–413, November 2011.

[29] Line H. Clemmensen, Bjørn S. Dissing, Grethe Hyldig, and Hanne Løje. Multispectral imaging of wok-fried vegetables. *Journal of Imaging Science and Technology*, 56(2):020404, 2012.

[30] Line H. Clemmensen, Michael Hansen, and Bjarne K. Ersbøll. A comparison of dimension reduction methods with application to multi-spectral images of sand used in concrete. *Machine Vision and Applications*, 21:959–968, 2010.

[31] Line H. Clemmensen, Michael E. Hansen, Jens C. Frisvad, and Bjarne K. Ersbøll. A method for comparison of growth media in objective identification of penicillium based on multi-spectral imaging. *Journal of Microbiological Methods*, 69(2):249–255, 2007.

[32] Line Katrine Harder Clemmensen and Bjarne Kjær Ersbøll. Multispectral recordings and analysis of psoriasis lesions. *MICCAI 06 - Workshop on Biophotonics Imaging for Diagnostics and Treatment, October 6, 2006 proceedings, 9th MICCAI Conference*, 2006.

[33] W.W. Coblentz. The reflecting power of various metals. *Journal of The Franklin Institute*, 170(3):169–193, 1910.

[34] Corinna Cortes and Vladimir Vapnik. Support-vector networks. *Machine Learning*, 20(3):273–297, 1995.

[35] Marie-Françoise Devaux, Brigitte Bouchet, David Legland, Fabienne Guillon, and Marc Lahaye. Macro-vision and grey level granulometry for quantification of tomato pericarp structure. *Postharvest Biology and Technology*, 47(2):199–209, 2008.

[36] Bjørn S. Dissing, Jens M. Carstensen, and Rasmus Larsen. Multispectral colormapping using penalized least square regression. *Journal of Imaging Science and Technology*, 54(3):0304011–0304016, 2010.

[37] Bjørn S. Dissing, Michael E. Nielsen, Bjarne K. Ersbøll, and Stina Frosch. Multispectral imaging for determination of astaxanthin concentration in salmonids. *PLoS One*, 6(5):Article No.: e19032, 2011.

[38] Bjørn Skovlund Dissing, Line Katrine Harder Clemmensen, Bjarne Kjær Ersbøll, Hanne Løje, and Jens Adler-Nissen. Temporal reflectance changes in vegetables. *2009 IEEE 12th International Conference on Computer Vision Workshops (ICCV Workshops)*, pages 1917–1922, 2009.

[39] Bjørn Skovlund Dissing, Bjarne Kjær Ersbøll, and Jens Adler-Nissen. *New vision technology for multidimensional quality monitoring of food processes*. PhD thesis, Technical University of Denmark (DTU), 2011.

[40] Bjørn Skovlund Dissing, Olga S Papadopoulou, Chrysoula Tassou, Bjarne Kjær Ersbøll, Jens Michael Carstensen, Efstathios Z Panagou, and George-John Nychas. Using multispectral imaging for spoilage detection of pork meat. *Food and Bioprocess Technology*, pages 1–12, 2012.

[41] Michael Elad. *Sparse and redundant representations : from theory to applications in signal and image processing*. Springer, 2010.

[42] U. Erikson and E. Misimi. Atlantic salmon skin and fillet color changes effected by perimortem handling stress, rigor mortis, and ice storage. *Journal of Food Science*, 73(2):C50–C59, 2008.

[43] Bjarne K. Ersbøll and Knut Conradsen. *An Introduction to Statistics, vol. 2*. DTU Informatics, 7 edition, 2007.

[44] E. Fernandez-Ahumada, J. M. Roger, B. Palagos, J. E. Guerrero, D. Perez-Marin, and A. Garrido-Varo. Multivariate near-infrared reflection spectroscopy strategies for ensuring correct labeling at feed bagging in the animal feed industry. *Applied Spectroscopy*, 64(1):83–91, 2010.

[45] J.A. Fernández Pierna, V. Baeten, and P. Dardenne. Screening of compound feeds using nir hyperspectral data. *Chemometrics and Intelligent Laboratory Systems*, 84(1-2):114–118, 2006.

[46] R.A. Fisher. The use of multiple measurements in taxonomic problems. *Annals Of Eugenics*, 7:179–188, 1936.

[47] Are Folkestad, Jens Petter Wold, Kjell-Arne Rørvik, Jon Tschudi, Karl Henrik Haugholt, Kari Kolstad, and Turid Mørkøre. Rapid and non-invasive measurements of fat and pigment concentrations in live and slaughtered atlantic salmon (salmo salar l.). *Aquaculture*, 280(1-4):129–135, 2008.

[48] Jørgen Folm-Hansen. *On chromatic and geometrical calibration*. PhD thesis, Technical University of Denmark, 1999.

[49] M. Foster, R. Petrell, M. R. Ito, and R. Ward. Detection and counting of uneaten food pellets in a sea cage using image analysis. *Aquacultural Engineering*, 14(3):251 – 269, 1995.

[50] Stina Frosch, Bjørn Skovlund Dissing, Jens Adler-Nissen, and Michael Engelbrecht Nielsen. Spectral imaging as a tool in food research and quality monitoring of food production. *Wide Spectra of Quality Control*, pages 373–384, 2011.

[51] George M. Furnival and Robert W. Wilson Jr. Regressions by leaps and bounds. *Technometrics*, 42(1):69–79, 2000.

[52] Ana Garrido-Varo, Maria Dolores Perez-Marin, Jose Emilio Guerrero, Augusto Gomez-Cabrera, Maria Jose de la Haba, Jara Bautista, Ana Soldado, Fernando Vicente, Adela Martinez, Begona de la Roza-Delgado, and Silvia Termes. Near infrared spectroscopy for enforcement of european legislation concerning the use of animal by-products in animal feeds. *Biotechnologie Agronomie Societe et Environnement*, 9(1):3–9, 2005.

[53] Paul Geladi, Hans Isaksson, Lennart Lindqvist, Svante Wold, and Kim Esbensen. Principal component analysis of multivariate images. *Chemometrics and Intelligent Laboratory Systems*, 5(3):209 – 220, 1989.

[54] Paul L. M. Geladi and Hans F. Grahn, editors. *Techniques and Applications of Hyperspectral Image Analysis*. John Wiley & Sons, Ltd, 2007.

[55] Antonio Girolami, Fabio Napolitano, Daniela Faraone, and Ada Braghieri. Measurement of meat color using a computer vision system. *Meat Science*, 93(1):111–118, 2013.

[56] David Delgado Gomez, Line Harder Clemmensen, Bjarne K. Ersbøll, and Jens Michael Carstensen. Precise acquisition and unsupervised segmentation of multi-spectral images. *Computer Vision and Image Understanding*, 106(2-3):183–193, 2007.

[57] T. R. Gormley. A note on consumer preference of smoked salmon colour. *Irish Journal of Agricultural and Food Research*, 31(2):199–202, 1992.

[58] Jacob Gøtterup, Karsten Olsen, Susanne Knøchel, Karsten Tjener, Louise H. Stahnke, and Jens K.S. Møller. Colour formation in fermented sausages by meat-associated staphylococci with different nitrite- and nitrate-reductase activities. *Meat Science*, 78(4):492–501, 2008.

[59] Hermann Grassmann. Zur theorie der farbenmischung. *Annalen der Physik*, 165(5):69–84, 1853.

[60] David M. Haaland and Edward V. Thomas. Partial least-squares methods for spectral analyses. 1. relation to other quantitative calibration methods and the extraction of qualitative information. *Analytical Chemistry*, 60(11):1193–1202, 1988.

[61] Mazen L. Hamad, Christopher D. Ellison, Mansoor A. Khan, and Robbe C. Lyon. Drug product characterization by macropixel analysis of chemical images. *Journal of Pharmaceutical Sciences*, 96(12):3390–3401, 2007.

[62] Michael Edberg Hansen, Bjarne Kjær Ersbøll, Jens Michael Carstensen, and Allan Aasbjerg Nielsen. Estimation of critical parameters in concrete production using multispectral vision technology. *Lecture Notes in Computer Science*, pages 1228–1237, 2005.

[63] Trevor Hastie, Robert Tibshirani, and Jerome Friedman. *The Elements of Statistical Learning: Data Mining, Inference, and Prediction*. Springer, 2nd edition, February 2009.

[64] Lars Helge Stien, Fredrik Manne, Kari Ruohonene, Antti Kause, Krisna Rungruangsak-Torrissen, and Anders Kiessling. Automated image analysis as a tool to quantify the colour and composition of rainbow trout (oncorhynchus mykiss w.) cutlets. *Aquaculture*, 261(2):695–705, 2006.

[65] Arthur E. Hoerl and Robert W. Kennard. Ridge regression: Biased estimation for nonorthogonal problems. *Technometrics*, 12(1):55–67, 1970.

[66] Harold Hotelling. Relations between two sets of variates. *Biometrika Trust*, 28(3/4):321–377, December 1936.

[67] Martin Jägersand. Saliency maps and attention selection in scale and spatial coordinates: an information theoretic approach. *IEEE International Conference on Computer Vision*, pages 195–202, 1995.

[68] Shyam N. Jha, editor. *Nondestructive evaluation of food quality : theory and practice*. Springer-Verlag, 2010.

[69] Thorsten Joachims. *Making large-Scale SVM Learning Practical. Advances in Kernel Methods - Support Vector Learning*. MIT-Press, 1999.

[70] E. A. Johnson and G. H. An. Astaxanthin from microbial sources. *CRC Critical Reviews in Biotechnology*, 11(4):297–326, 1991.

[71] Eric A. Johnson, Tomas G. Villa, and Michael J. Lewis. Phaffia rhodozyma as an astaxanthin source in salmonid diets. *Aquaculture*, 20(2):123–134, 1980.

[72] Ronald Jones and Pierre Soille. Periodic lines: Definition, cascades, and application to granulometries. *Pattern Recognition Letters*, 17(10):1057 – 1063, 1996.

[73] K. Kobayashi, M. Masaaki, T. Toyota, and S. Nakauchi. Visualisation of fat and fatty acid distribution in beef using a set of filters based on near infrared spectroscopy. *Journal of Near Infrared Spectroscopy*, 20(5):509–519, 2012.

[74] K. Kobayashi, Y. Matsui, Y. Maebuchi, T. Toyota, and S. Nakauchi. Near infrared spectroscopy and hyperspectral imaging for prediction and visualisation of fat and fatty acid content in intact raw beef cuts. *Journal of Near Infrared Spectroscopy*, 18(5):301–315, 2010.

[75] K.-i. Kobayashi, T. Yamada, A. Hiraishi, and S. Nakauchi. Real-time optical monitoring of microbial growth using optimal combination of light-emitting diodes. *Optical Engineering*, 51(12):123201, 2012.

[76] Ken-ichi Kobayashi, Ken Nishino, Bjørn Skovlund Dissing, Masaaki Mori, Toshihiro Toyota, and Shigeki Nakauchi. Design of characteristics of optical filter set for prediction and visualization of fat content in raw beef cuts. *Scandinavian Workshop on Imaging Food Quality 2011 : Ystad, May 27, 2011 - Proceedings*, pages 23–28, 2011.

[77] Fanbin Kong, Juming Tang, B. Rasco, C. Crapo, and S. Smiley. Quality changes of salmon (oncorhynchus gorbuscha) muscle during thermal processing. *Journal of Food Science*, 72(2):S103–S111, 2007.

[78] Rasmus Larsen, Morten Arngren, Morten Arngren, Per Waaben Hansen, and Allan Aasbjerg Nielsen. Kernel based subspace projection of near infrared hyperspectral images of maize kernels. *Lecture Notes in Computer Science (including subseries Lecture Notes in Artificial Intelligence and Lecture Notes in Bioinformatics)*, 5575 LNCS:560–569, 2009.

[79] Nejla Lassoued, Perrine Babin, Guy Della Valle, Marie-Françoise Devaux, and Anne-Laure Réguerre. Granulometry of bread crumb grain: Contributions of 2d and 3d image analysis at different scale. *Food Research International*, 40(8):1087–1097, 2007.

[80] Kurt C. Lawrence, William R. Windham, Bosoon Park, Douglas P. Smith, and Gavin H. Poole. Comparison between visible/nir spectroscopy and hyperspectral imaging for detecting surface contaminants on poultry carcasses. *Proceedings of the SPIE - The International Society for Optical Engineering*, 5271(1):35–42, 2004.

[81] Tony Lindeberg. Scale-space: A framework for handling image structures at multiple scales. *Cern School of Computing*, 96(8):27–38, 1996.

[82] Tony Lindeberg. Feature detection with automatic scale selection. *International Journal of Computer Vision*, 30(2):79–116, 1998.

[83] Tony Lindeberg. Principles for automatic scale selection. *Handbook on Computer Vision and Applications*, 2:239–274, 1999. Academic Press, Boston, USA.

[84] Yongliang Liu, Kuanglin Chao, Moon S. Kim, David Tuschel, Oksana Olkhovyk, and Ryan J. Priore. Potential of raman spectroscopy and imaging methods for rapid and routine screening of the presence of melamine in animal feed and foods. *Applied Spectroscopy*, 63(4):477–480, 2009.

[85] Martin Georg Ljungqvist, Bjørn Skovlund Dissing, Michael Engelbrecht Nielsen, Bjarne Kjær Ersbøll, Line Harder Clemmensen, and Stina Frosch. Classification of astaxanthin colouration of salmonid fish using spectral imaging and tricolour measurement. Technical Report 08, Technical University of Denmark, Informatics, 2012.

[86] Martin Georg Ljungqvist, Bjarne Kjær Ersbøll, Michael Engelbrecht Nielsen, and Stina Frosch. Multi-spectral image analysis for astaxanthin coating classification. *Scandinavian Workshop on Imaging Food Quality 2011 : Ystad, May 27, 2011 - Proceedings*, pages 63–68, 2011.

[87] Martin Georg Ljungqvist, Bjarne Kjær Ersbøll, Michael Engelbrecht Nielsen, and Stina Frosch. Multispectral image analysis for astaxanthin coating classification. *Journal of Imaging Science and Technology*, 56(2):020403–1 – 020403–6, 2012. http://imaging.org/IST/store/epub.cfm?abstrid=45215.

[88] Martin Georg Ljungqvist, Stina Frosch, Michael Engelbrecht Nielsen, and Bjarne K. Ersbøll. Analysis of astaxanthin in fish feed pellets. *Proc. West European Fish Technologists Association*, 40:59–60, Oct 2010.

[89] Martin Georg Ljungqvist, Stina Frosch, Michael Engelbrecht Nielsen, and Bjarne Kjær Ersbøll. Multispectral image analysis for robust prediction of astaxanthin coating. *Applied Spectroscopy*, 67(7), July 2013. Accepted for publication.

[90] Martin Georg Ljungqvist, Ken-ichi Kobayashi, Stina Frosch, Michael Engelbrecht Nielsen, Bjarne Kjær Ersbøll, and Shigeki Nakauchi. Near-infrared hyper-spectral image analysis of astaxanthin concentration in fish feed coating. *Proceedings of the IEEE International Conference on Imaging Systems and Techniques*, pages 136–141, July 2012. http://dx.doi.org/10.1109/IST.2012.6295524.

[91] Martin Georg Ljungqvist, Michael Engelbrecht Nielsen, Bjarne Kjær Ersbøll, and Stina Frosch. Image analysis of pellet size for a control system in industrial feed production. *PLoS ONE*, 6(10):e26492, 10 2011. http://dx.doi.org/10.1371/journal.pone.0026492.

[92] Martin Georg Ljungqvist, Otto Højager Nielsen, Stina Frosch, Michael Engelbrecht Nielsen, Line Harder Clemmensen, and Bjarne Kjær Ersbøll. Hyper-spectral imaging based on diffused laser light for prediction of astaxanthin coating concentration. *Machine Vision and Applications*, 2013. Accepted for publication. http://dx.doi.org/10.1007/s00138-013-0512-2.

[93] Hanne Løje, Bjørn Skovlund Dissing, Line Katrine Harder Clemmensen, Bjarne Kjær Ersbøll, and Jens Adler-Nissen. Multispectral imaging of wok fried vegetables. *Scandinavian Workshop on Imaging Food Quality 2011 : Ystad, May 27, 2011 - Proceedings*, pages 59–62, 2011.

[94] Mette Marie Løkke, Helene Fast Seefeldt, Thomas Skov, and Merete Edelenbos. Color and textural quality of packaged wild rocket measured by multispectral imaging. *Postharvest Biology and Technology*, 75:86–95, 2013.

[95] P. Maragos. Pattern spectrum and multiscale shape representation. *Pattern Analysis and Machine Intelligence, IEEE Transactions on*, 11(7):701 –716, jul 1989.

[96] Georges Matheron. *Random sets and integral geometry*. John Wiley, 1975.

[97] Georges Matheron and Jean Serra. The birth of mathematical morphology. *Mathematical Morphology, Proceedings*, pages 1–16, 2002.

[98] Gail McConnell and Erling Riis. Photonic crystal fibre enables short-wavelength two-photon laser scanning fluorescence microscopy with fura-2. *Physics in Medicine and Biology*, 49(20):4757, 2004.

[99] E Misimi, J R Mathiassen, and U Erikson. Computer vision-based sorting of atlantic salmon (salmo salar) fillets according to their color level. *Journal of Food Science*, 72(1):S030, 2007.

[100] Douglas C. Montgomery. *Introduction to statistical quality control*. Wiley, 2005.

[101] L.A. Morales-Hernández, I.R. Terol-Villalobos, A. Domínguez-González, F. Manríquez-Guerrero, and G. Herrera-Ruiz. Spatial distribution and spheroidicity characterization of graphite nodules based on morphological tools. *Journal of Materials Processing Tech.*, 210(2):335–342, 2010.

[102] Shigeki Nakauchi, Ken Nishino, and Takuya Yamashita. Selection of optimal combinations of band-pass filters for ice detection by hyperspectral imaging. *Optics Express*, 20(2):986–1000, 2012.

[103] M. E. Nielsen, H. Mikkelsen, L. B. Nielsen, and O. Joensen. By-product based production of natural astaxanthin (nax). *7th Joint meeting: 50th Annual Atlantic Fisheries Technology Conference and 29th Annual Seafood Science and Technology Society of the Americas*, 2005.

[104] Otto Højager Attermann Nielsen, Anders Lindbjerg Dahl, Rasmus Larsen, Henrik Aanæs, Jens Michael Carstensen, Flemming Møller, Frederik Donbæk Nielsen, and Carsten L. Thomsen. Supercontinuum light sources for hyperspectral subsurface laser scattering: Applications for food inspection. *Lecture Notes in Computer Science (including subseries Lecture Notes in Artificial Intelligence and Lecture Notes in Bioinformatics)*, 6688 LNCS:327–337, 2011.

[105] Otto Højager Attermann Nielsen, Anders Lindbjerg Dahl, Rasmus Larsen, Flemming Møller, Frederik Donbæk Nielsen, Carsten L. Thomsen, Henrik Aanæs, and Jens Michael Carstensen. In depth analysis of food structures. *Scandinavian Workshop on Imaging Food Quality 2011 : Ystad, May 27, 2011 - Proceedings*, pages 29–34, 2011.

[106] L. Nørgaard, A. Saudland, J. Wagner, J. P. Nielsen, L. Munck, and S. B. Engelsen. Interval partial least-squares regression (ipls): A comparative chemometric study with an example from near-infrared spectroscopy. *Applied Spectroscopy*, 54(3):413–419, 2000.

[107] Daniel Nyström. Colorimetric and multispectral image acquisition using model-based and empirical device characterization. In Bjarne K. Ersbøll and Kim Steenstrup Pedersen, editors, *SCIA*, volume 4522 of *Lecture Notes in Computer Science*, pages 798–807. Springer, 2007.

[108] J. Ostrander, C. Martinsen, J. Liston, and J. McCullough. Sensory testing of pen-reared salmon and trout. *Journal of Food Science*, 41(2):386–390, 1976.

[109] Silje Ottestad, Oddvin Sørheim, Karsten Heia, Josefine Skaret, and Jens Petter Wold. Effects of storage atmosphere and heme state on the color and visible reflectance spectra of salmon (salmo salar) fillets. *Journal of Agricultural and Food Chemistry*, 59(14):7825–7831, 2011.

[110] B. Park, Y.R. Chen, and M. Nguyen. Multi-spectral image analysis using neural network algorithm for inspection of poultry carcasses. *Journal of Agricultural Engineering Research*, 69(4):351 – 363, 1998.

[111] Kyoo-Chul Park, Hyungryul J. Choi, Chih-Hao Chang, Robert E. Cohen, Gareth H. McKinley, and George Barbastathis. Nanotextured silica surfaces with robust superhydrophobicity and omnidirectional broadband supertransmissivity. *ACS Nano*, 6(5):3789–3799, 2012.

[112] Kevin David Parsonage. Detection of fish-food pellets in highly-cluttered underwater images with variable illumination. Master's thesis, Department of Chemical and Biological Engineering, The University of British Columbia, 2001.

[113] Karl Pearson. On lines and planes of closest fit to systems of points in space. *Philosophical Magazine*, 2(7-12):559–572, 1901.

[114] J. A. Fernández Pierna, V. Baeten, A. Michotte Renier, R. P. Cogdill, and P. Dardenne. Combination of support vector machines (svm) and near-infrared (nir) imaging spectroscopy for the detection of meat and bone meal (mbm) in compound feeds. *Journal of Chemometrics*, 18(7-8):341–349, 2004.

[115] Melba B. Reantaso. Aquaculture newsletter. *Food and Agriculture Organization of the United Nations*, 49, June 2012.

[116] Cecilia Riccioli, Dolores Perez-Marin, Jose Emilio Guerrero-Ginel, Wouter Saeys, and Ana Garrido-Varo. Pixel selection for near-infrared chemical

imaging (nir-ci) discrimination between fish and terrestrial animal species in animal protein by-product meals. *Applied Spectroscopy*, 65(7):771–781, 2011.

[117] Asmund Rinnan, Frans van den Berg, and Søren Balling Engelsen. Review of the most common pre-processing techniques for near-infrared spectra. *TrAC Trends in Analytical Chemistry*, 28(10):1201–1222, 2009.

[118] S. K. Rod, F. Hansen, F. Leipold, and S. Knochel. Cold atmospheric pressure plasma treatment of ready-to-eat meat: Inactivation of listeria innocua and changes in product quality. *Food Microbiology*, 30(1):233–238, 2012.

[119] Juan G. Rosas and Marcelo Blanco. A criterion for assessing homogeneity distribution in hyperspectral images. part 1: Homogeneity index bases and blending processes. *Journal of Pharmaceutical and Biomedical Analysis*, 70:680–690, 2012.

[120] Guilherme P. Sabin, Márcia C. Breitkreitz, André M. de Souza, Patrícia da Fonseca, Lupercio Calefe, Mario Moffa, and Ronei J. Poppi. Analysis of pharmaceutical pellets: An approach using near-infrared chemical imaging. *Analytica Chimica Acta*, 706(1):113–119, 2011.

[121] Norbert Scherer, Justin E Jureller, T.A. Birks, W.J. Wadsworth, and P. St. J. Russell. Widely tunable femtosecond pulses from a tapered fiber for ultrafast microscopy and multiphoton applications. In *The Thirteenth International Conference on Ultrafast Phenomena*, page TuE41. Optical Society of America, 2002.

[122] Jean Serra. *Image Analysis and Mathematical Morphology*. Academic Press, London, 1982.

[123] A Seybold and T W Goodwin. Occurrence of astaxanthin in the flower petals of adonis annua l. *Nature*, 184 (Suppl 22):1714–1715, 1959.

[124] Muhammad A. Shahin and Stephen J. Symons. Detection of fusarium damaged kernels in canada western red spring wheat using visible/near-infrared hyperspectral imaging and principal component analysis. *Computers and Electronics in Agriculture*, 75(1):107–112, 2011.

[125] W. A. Shewhart. Quality control charts. *Bell System Technical Journal*, 5(4):72–82, 1926.

[126] WA Shewhart. Application of statistical methods to manufacturing problems. *Journal of the Franklin Institute*, 226:163–186, 1938.

[127] S. Sigurgisladottir, C.C. Parrish, S.P. Lall, and R.G. Ackman. Effects of feeding natural tocopherols and astaxanthin on atlantic salmon (salmo salar) fillet quality. *Food Research International*, 27(1):23–32, 1994.

[128] Artemis P. Simopoulos. Omega-3 fatty acids in health and disease and in growth and development. *American Journal of Clinical Nutrition*, 54:438–463, 1991.

[129] Agnar Holten Sivertsen, Karsten Heia, Kristian Hindberg, and Fred Godtliebsen. Automatic nematode detection in cod fillets (gadus morhua l.) by hyperspectral imaging. *Journal of Food Engineering*, 111(4):675–681, 2012.

[130] Karl Sjöstrand, Line Harder Clemmensen, Rasmus Larsen, and Bjarne Ersbøll. Spasm: A matlab toolbox for sparse statistical modeling. *Journal of Statistical Software*. Accepted for publication 2012.

[131] Michael Sjöström, Svante Wold, Walter Lindberg, Jan-Åke Persson, and Harald Martens. A multivariate calibration problem in analytical chemistry solved by partial least-squares models in latent variables. *Analytica Chimica Acta*, 150:61–70, 1983.

[132] Izumi Sone, Ragnar L. Olsen, Agnar H. Sivertsen, Guro Eilertsen, and Karsten Heia. Classification of fresh atlantic salmon (salmo salar l.) fillets stored under different atmospheres by hyperspectral imaging. *Journal of Food Engineering*, 109(3):482–489, 2012.

[133] S. K. Stormo, A. H. Sivertsen, K. Heia, H. Nilsen, and E. Elvevoll. Effects of single wavelength selection for anisakid roundworm larvae detection through multispectral imaging. *Journal of Food Protection*, 70(8):1890–1895, 2007.

[134] Da-Wen Sun, editor. *Hyperspectral imaging for food quality analysis and control*. Academic Press, 2010.

[135] Paul Switzer and A. A. Green. Min/max autocorrelation factors for multivariate spatial imagery. Technical Report 6, Stanford University, Department of Statistics, 1984.

[136] Jo-Anne L. Tabachek. The effect of feed particle size on the growth and feed efficiency of arctic charr [salvelinus alpinus (l.)]. *Aquaculture*, 71(4):319–330, 1988.

[137] R Tibshirani. Regression shrinkage and selection via the lasso. *Journal Of The Royal Statistical Society Series B-methodological*, 58(1):267–288, 1996.

[138] O.J. Torrisen, R.W. Hardy, and K.D. Shearer. Pigmentation of salmonids - carotenoid deposition and metabolism. *Reviews in Aquatic Sciences*, 1(2):209–225, 1989.

[139] S. A. Turujman, W. G. Wamer, Rong Rong Wei, and R. H. Albert. Rapid liquid chromatographic method to distinguish wild salmon from aquacultured salmon fed synthetic astaxanthin. *Journal of AOAC International*, 80(3):622–632, 1997.

[140] Devrim Unay, Bernard Gosselin, Olivier Kleynen, Vincent Leemans, Marie-France Destain, and Olivier Debeir. Automatic grading of bicolored apples by multispectral machine vision. *Computers and Electronics in Agriculture*, 75:204–212, 2011.

[141] Luc Vincent. Fast grayscale granulometry algorithms. *Mathematical Morphology and its Applications to Image Processing*, 2:265–272, 1994.

[142] Luc Vincent. Fast granulometric methods for the extraction of global image information. *Proc. 11th Annual Symposium of the South African Pattern Recognition Association*, pages 119–133, 2000.

[143] Wenbo Wang and Jitendra Paliwal. Potential of near-infrared hyperspectral reflactance imaging for screening of farm feed contamination. *Progress in Biomedical Optics and Imaging - Proceedings of SPIE*, 5969:59692T, 2005.

[144] Xiaopeng Wang, Yingjie Li, and Yanli Shang. Measurement of microcapsules using morphological operators. *2006 8th International Conference On Signal Processing, Vols 1-4*, pages 1286–1289, 2006.

[145] JWJ Wankowski and JE Thorpe. Role of food particle-size in the growth of juvenile atlantic salmon (salmo-salar l.). *Journal of Fish Biology*, 14(4):351–370, 1979.

[146] John N. C. Whyte and Kathleen L. Sherry. Pigmentation and composition of flesh of atlantic salmon fed diets supplemented with the yeast phaffia rhodozyma. *North American Journal of Aquaculture*, 63(1):52–57, 2001.

[147] P. C. Williams and D. C. Sobering. Comparison of commercial near infrared transmittance and reflectance instruments for analysis of whole grains and seeds. *Journal of Near Infrared Spectroscopy*, 1(1):25–32, 1993.

[148] Jens Petter Wold, Brian J. Marquardt, Brian K. Dable, Dave Robb, and Bjarne Hatlen. Rapid quantification of carotenoids and fat in atlantic salmon (salmo salar l.) by raman spectroscopy and chemometrics. *Applied Spectroscopy*, 58(4):395–403, 2004.

[149] J.P. Wold, F. Westad, and K. Heia. Detection of parasites in cod fillets by using simca classification in multispectral images in the visible and nir region. *Applied Spectroscopy*, 55(8):1025–1034, 2001.

[150] G. Wyszecki and W.S. Stiles. *Color science. Concepts and methods, quantitative data and formulae. 2.ed.* Wiley, 1982. (Bibl.s.885-924) (Wiley series in pure and applied optics).

[151] Yavuz Yagiz, Murat O Balaban, Hordur G Kristinsson, Bruce A Welt, and Maurice R Marshall. Comparison of minolta colorimeter and machine vision system in measuring colour of irradiated atlantic salmon. *Journal of the Science of Food and Agriculture*, 89(4):728–730, 2009.

[152] Yavuz Yagiz, Hordur G. Kristinsson, Murat O. Balaban, Bruce A. Welt, Maria Ralat, and Maruice R. Marshall. Effect of high pressure processing and cooking treatment on the quality of atlantic salmon. *Food Chemistry*, 116(4):828–835, 2009.

[153] Yuichi Yamane, Takashi Mikami, Katsuya Higashida, Toshihide Kakizono, and Naomichi Nishio. Estimation of the concentrations of cells, astaxanthin and glucose in a culture of phaffia rhodozyma by near infrared reflectance spectroscopy. *Biotechnology Techniques*, 10:529–534, 1996. 10.1007/BF00159519.

[154] Haibo Yao, Zuzana Hruska, Russell Kincaid, Ambrose Ononye, Robert L. Brown, Deepak Bhatnagar, and Thomas E. Cleveland. Development of narrow-band fluorescence index for the detection of aflatoxin contaminated corn. *Proceedings of the SPIE - The International Society for Optical Engineering*, 8027:80270D, 2011.

[155] Peiqiang Yu. Application of cluster analysis (cla) in feed chemical imaging to accurately reveal structural-chemical features of feeds and plants within cellular dimension. *Journal of Agricultural and Food Chemistry*, 53(8):2872–2880, 2005.

[156] Jian-Ping Yuan and Feng Chen. Identification of astaxanthin isomers in haematococcus lacustris by hplc-photodiode array detection. *Biotechnology Techniques*, 11(7):455–459, 1997.

[157] Andrzej Zadoroźny, Hong Zhang, and Martin Jägersand. Granulometry using image transform techniques. *International Conference on Vision Interface*, 15:433–438, 2002.

[158] Yonghui Zhao, Lawrence Taplin, Mahdi Nezamabadi, and Roy Berns. Using the matrix r method for spectral image archives. *AIC Colour 05 - 10th Congress of the International Colour Association*, 10, May 2005.

[159] Fengle Zhu, Shuxi Cheng, Di Wu, and Yong He. Rapid discrimination of fish feeds brands based on visible and short-wave near-infrared spectroscopy. *Food and Bioprocess Technology*, 4(4):597–602, 2011.

[160] H Zou and T Hastie. Regularization and variable selection via the elastic net. *Journal Of The Royal Statistical Society Series B - Statistical Methodology*, 67:301–320, 2005.